

1991

Modification of axial-flow compressor stall margin by variation of stationary blade setting angles

John Paul Rukavina
Iowa State University

Follow this and additional works at: <https://lib.dr.iastate.edu/rtd>

 Part of the [Mechanical Engineering Commons](#)

Recommended Citation

Rukavina, John Paul, "Modification of axial-flow compressor stall margin by variation of stationary blade setting angles " (1991).
Retrospective Theses and Dissertations. 9575.
<https://lib.dr.iastate.edu/rtd/9575>

This Dissertation is brought to you for free and open access by the Iowa State University Capstones, Theses and Dissertations at Iowa State University Digital Repository. It has been accepted for inclusion in Retrospective Theses and Dissertations by an authorized administrator of Iowa State University Digital Repository. For more information, please contact digirep@iastate.edu.

INFORMATION TO USERS

This manuscript has been reproduced from the microfilm master. UMI films the text directly from the original or copy submitted. Thus, some thesis and dissertation copies are in typewriter face, while others may be from any type of computer printer.

The quality of this reproduction is dependent upon the quality of the copy submitted. Broken or indistinct print, colored or poor quality illustrations and photographs, print bleedthrough, substandard margins, and improper alignment can adversely affect reproduction.

In the unlikely event that the author did not send UMI a complete manuscript and there are missing pages, these will be noted. Also, if unauthorized copyright material had to be removed, a note will indicate the deletion.

Oversize materials (e.g., maps, drawings, charts) are reproduced by sectioning the original, beginning at the upper left-hand corner and continuing from left to right in equal sections with small overlaps. Each original is also photographed in one exposure and is included in reduced form at the back of the book.

Photographs included in the original manuscript have been reproduced xerographically in this copy. Higher quality 6" x 9" black and white photographic prints are available for any photographs or illustrations appearing in this copy for an additional charge. Contact UMI directly to order.

U·M·I

University Microfilms International
A Bell & Howell Information Company
300 North Zeeb Road, Ann Arbor, MI 48106-1346 USA
313/761-4700 800/521-0600

Order Number 9126243

**Modification of axial-flow compressor stall margin by variation
of stationary blade setting angles**

Rukavina, John Paul, Ph.D.

Iowa State University, 1991

U·M·I
300 N. Zeeb Rd.
Ann Arbor, MI 48106

NOTE TO USERS

**THE ORIGINAL DOCUMENT RECEIVED BY U.M.I. CONTAINED PAGES
WITH POOR PRINT. PAGES WERE FILMED AS RECEIVED.**

THIS REPRODUCTION IS THE BEST AVAILABLE COPY.

**Modification of axial-flow compressor stall margin
by variation of stationary blade setting angles**

by

John Paul Rukavina

**A Dissertation Submitted to the
Graduate Faculty in Partial Fulfillment of the
Requirements for the Degree of
DOCTOR OF PHILOSOPHY**

Major: Mechanical Engineering

Approved:

Signature was redacted for privacy.

In Charge of Major Work

Signature was redacted for privacy.

For the Major Department

Signature was redacted for privacy.

For the Graduate College

**Iowa State University
Ames, Iowa
1991**

TABLE OF CONTENTS

NOMENCLATURE	xiv
ABSTRACT	xviii
1. INTRODUCTION	1
1.1 Stall	4
1.2 Surge	7
1.3 Avoiding Stall	8
2. RELATED ISOLATED AIRFOIL DYNAMIC STALL RESEARCH	12
3. PROOF OF CONCEPT IN LOW-SPEED COMPRESSORS . .	24
3.1 Stationary Blade Setting Angle Variations	25
3.2 Two-Stage Axial-Flow Fan	29
3.2.1 Two-stage fan performance tests	31
3.2.2 Axial-flow fan results	33
3.3 Three-Stage Axial-Flow Compressor	39
3.3.1 Three-stage compressor performance tests	43
3.3.2 Three-stage compressor results	45
3.4 Detailed Flow Measurements for Three-Stage Compressor	57
3.4.1 Velocity diagram calculations using detailed measurements . .	67

3.5	Low-Speed Compressor Conclusions	74
4.	PRATT & WHITNEY COMPRESSOR	78
4.1	Pratt & Whitney Axial-Flow Compressor	78
4.1.1	D.C. drive motor and gearbox	83
4.1.2	Throttle	83
4.1.3	Surge detection and relief system	84
4.2	Pratt & Whitney Compressor Data Acquisition System	88
4.2.1	Pressure system	88
4.2.2	Temperature system	106
4.3	Pratt & Whitney Three-Stage Compressor Performance Tests	108
4.3.1	Inlet corrected mass flow	108
4.3.2	Compressor pressure rise ratio	113
4.3.3	Inlet corrected rotational speed	114
4.3.4	Detection of stall in the Pratt & Whitney compressor	114
5.	ESTIMATION OF REDUCED FREQUENCY AND ROTOR INLET FLOW ANGLE VARIATION FOR PRATT & WHIT- NEY COMPRESSOR	116
5.1	Calculation of Reduced Frequency at Stall, K_{stall} , for the Pratt & Whitney Compressor	118
5.2	Rotor Inlet Flow Angle Analysis for Pratt & Whitney Three-Stage Compressor	126
6.	PRATT & WHITNEY RESULTS AND DISCUSSIONS	135
6.1	Pratt and Whitney Baseline and Modified Compressor Performance	135
6.1.1	Pratt & Whitney detailed flow measurements	138

7. CONCLUSIONS	155
8. BIBLIOGRAPHY	160
9. ACKNOWLEDGEMENTS	162
10. APPENDIX A: DETAILED FLOW MEASUREMENTS FOR THREE-STAGE COMPRESSOR	163
11. APPENDIX B: VELOCITY DIAGRAM CALCULATIONS FROM DETAILED MEASUREMENT DATA	171

LIST OF TABLES

Table 3.1:	Summary of two-stage fan builds and results	34
Table 3.2:	Absolute flow angle (°), baseline, $\Phi = 0.353$	63
Table 3.3:	Absolute flow angle (°), baseline, $\Phi = 0.420$	63
Table 3.4:	Absolute flow angle (°) variation from baseline, $+6^\circ$ 2/rev, $\Phi = 0.353$	65
Table 3.5:	Absolute flow angle (°) variation from baseline, $+6^\circ$ 2/rev, $\Phi = 0.420$	65
Table 3.6:	Absolute flow angle (°) variation from baseline, -6° 2/rev, $\Phi = 0.353$	66
Table 3.7:	Absolute flow angle (°) variation from baseline, -16° 2/rev, $\Phi = 0.353$	66
Table 3.8:	Detailed flow measurement data, baseline, $\Phi = 0.353$	72
Table 3.9:	Detailed flow measurement data, $+6^\circ$ 2/rev, $\Phi = 0.353$	72
Table 3.10:	Detailed flow measurement data, -6° 2/rev, $\Phi = 0.353$	73
Table 3.11:	Detailed flow measurement data, -16° 2/rev, $\Phi = 0.353$	73
Table 4.1:	Pratt & Whitney compressor design specifications	81
Table 4.2:	Pratt & Whitney compressor blading specifications	82
Table 4.3:	D.C. drive motor specifications	84

Table 4.4:	Scanivalve pressure system power supplies	95
Table 4.5:	Control pressure logic	95
Table 4.6:	Calibration constants for the ZOC14 pressure sensor	105
Table 5.1:	Stalling mass flowrates and axial velocity at stall for the base- line compressor configuration	119
Table 5.2:	Velocity diagram calculations for the baseline stalling condition	121
Table 5.3:	Reduced frequency at stall, K_{stall} , for the Pratt & Whitney three-stage axial-flow compressor	122
Table 5.4:	Amplitude of blade setting angle variation, $\Delta\phi$, and corre- sponding rotor inlet flow angle variation for the low-speed, three-stage compressor	129
Table 5.5:	Amplitude of blade setting angle variation, $\Delta\phi$, and corre- sponding rotor inlet flow angle variation the Pratt & Whitney, three-stage compressor	133
Table 10.1:	Absolute flow angle (°), baseline, $\Phi = 0.353$	164
Table 10.2:	Absolute flow angle (°), baseline, $\Phi = 0.420$	164
Table 10.3:	Absolute flow angle (°), $+6^\circ$ 2/rev, $\Phi = 0.353$	165
Table 10.4:	Absolute flow angle (°) variation from baseline, $+6^\circ$ 2/rev, Φ $= 0.353$	165
Table 10.5:	Absolute flow angle (°), $+6^\circ$ 2/rev, $\Phi = 0.420$	166
Table 10.6:	Absolute flow angle (°) variation from baseline, $+6^\circ$ 2/rev, Φ $= 0.420$	166
Table 10.7:	Absolute flow angle (°), -6° 2/rev, $\Phi = 0.353$	167

Table 10.8:	Absolute flow angle (°) variation from baseline, -6° 2/rev, Φ = 0.353	167
Table 10.9:	Absolute flow angle (°), -6° 2/rev, $\Phi = 0.420$	168
Table 10.10:	Absolute flow angle (°) variation from baseline, -6° 2/rev, Φ = 0.420	168
Table 10.11:	Absolute flow angle (°), -16° 2/rev, $\Phi = 0.420$	169
Table 10.12:	Absolute flow angle (°) variation from baseline, -16° 2/rev, $\Phi = 0.420$	169
Table 10.13:	Absolute flow angle (°), -16° 2/rev, $\Phi = 0.353$	170
Table 10.14:	Absolute flow angle (°) variation from baseline, -16° 2/rev, $\Phi = 0.353$	170
Table 11.1:	Detailed flow measurement data, baseline, $\Phi = 0.353$	172
Table 11.2:	Detailed flow measurement data, baseline, $\Phi = 0.420$	172
Table 11.3:	Detailed flow measurement data, $+6^\circ$ 2/rev, $\Phi = 0.353$	173
Table 11.4:	Detailed flow measurement data, $+6^\circ$ 2/rev, $\Phi = 0.420$	173
Table 11.5:	Detailed flow measurement data, -6° 2/rev, $\Phi = 0.353$	174
Table 11.6:	Detailed flow measurement data, -6° 2/rev, $\Phi = 0.420$	174
Table 11.7:	Detailed flow measurement data, -16° 2/rev, $\Phi = 0.353$	175
Table 11.8:	Detailed flow measurement data, -16° 2/rev, $\Phi = 0.420$	175

LIST OF FIGURES

Figure 1.1:	Stall/surge boundary for a multistage compressor, Copenhagen [1]	2
Figure 1.2:	Propagation of stall in a cascade [2]	5
Figure 1.3:	Fully developed rotating stall cell [3]	6
Figure 2.1:	Typical airfoil pitching about a midchord axis	15
Figure 2.2:	Airfoil geometry and important angular quantities, McCroskey [5]	17
Figure 2.3:	Experimental stall boundary according to McCroskey [5]	18
Figure 2.4:	Dynamic stall angle increase as a function of K , Halfman et al. [6]	20
Figure 3.1:	Blade setting angle variations, (a) Sinusoidal, (b) Rectified Sine-wave, and (c) Asymmetric.	26
Figure 3.2:	Two-stage axial-flow fan apparatus	30
Figure 3.3:	Blade-to-blade view of two-stage, axial-flow fan blade rows	32
Figure 3.4:	One-stage axial-flow fan results, $\Delta\phi = 5^\circ$, $n = 3$ cycles/rev, rotor speed = 2000 rpm	36
Figure 3.5:	Two-stage axial-flow fan results, $\Delta\phi = 5^\circ$, $n = 3$ cycles/rev, rotor speed = 1600 rpm	37

Figure 3.6:	Three-stage axial-flow compressor apparatus	40
Figure 3.7:	Blade-to-blade view of three-stage, axial-flow compressor blade rows	41
Figure 3.8:	Three-stage axial-flow compressor results, inlet guide vane an- gle variation, $\Delta\phi = 6^\circ$, $n = 2$ cycles/rev, rotor speed = 1400 rpm.	47
Figure 3.9:	Three-stage axial-flow compressor results, inlet guide vane an- gle variation, $\Delta\phi = +6^\circ$, $n = 2$ cycles/rev, rotor speed = 1400 rpm.	49
Figure 3.10:	Three-stage axial-flow compressor results, inlet guide vane an- gle variation, $\Delta\phi = -6^\circ$, $n = 2$ cycles/rev, rotor speed = 1400 rpm.	50
Figure 3.11:	Three-stage axial-flow compressor results, inlet guide vane an- gle modification, $\Delta\phi_1 = -16^\circ$, $\Delta\phi_2 = -8^\circ$, $n = 2$ cycles/rev, rotor speed = 1400 rpm.	51
Figure 3.12:	Three-stage axial-flow compressor results, inlet guide vane, first and second stage stationary row angle variation, $\Delta\phi =$ 6° , $n = 2$ cycles/rev, rotor speed = 1400 rpm.	53
Figure 3.13:	Three-stage axial-flow compressor results, all inlet guide vanes set 6° more than the baseline setting angle, rotor speed = 1400 rpm.	54
Figure 3.14:	Three-stage axial-flow compressor results, all inlet guide vanes set 6° less than the baseline setting angle, rotor speed = 1400 rpm.	55

Figure 3.15: Measurement plane for detailed measurements at the exit of the inlet guide vane row	58
Figure 3.16: Setting angle variation regions for detailed measurements data	60
Figure 3.17: Total-pressure variation across two blade passages, inlet guide vane exit, baseline at 50% immersion, $\Phi = 0.353$ and $\Phi = 0.420$	62
Figure 4.1: Pratt & Whitney research compressor test stand	79
Figure 4.2: Pratt & Whitney compressor detail	80
Figure 4.3: Pratt & Whitney throttle section detail	85
Figure 4.4: Pratt & Whitney automatic surge detection and relief system	86
Figure 4.5: Scanivalve pressure system diagram	89
Figure 4.6: Scanivalve ZOC14 pressure scanning module	90
Figure 4.7: Scanivalve Thermal Control Unit (TCU)	92
Figure 4.8: Scanivalve Mux Address Control Unit (MACU)	93
Figure 4.9: Control pressure electrical circuit diagram	97
Figure 4.10: Electrical wiring diagram for ZOC pressure scanning	98
Figure 4.11: Using "Step" and "Home" commands on HP scanner	100
Figure 4.12: NPN transistor connectors for binary code deciphering	102
Figure 4.13: Calibration curve for ZOC channel #24	104
Figure 4.14: Total-pressure probe and measuring locations	110
Figure 5.1: Pratt & Whitney blade velocity diagram at stall for 50 percent speed	123
Figure 5.2: Pratt & Whitney blade velocity diagram at stall for 60 percent speed	123

Figure 5.3:	Pratt & Whitney blade velocity diagram at stall for 70 percent speed	124
Figure 5.4:	Pratt & Whitney blade velocity diagram at stall for 80 percent speed	124
Figure 5.5:	Pratt & Whitney blade velocity diagram at stall for 90 percent speed	125
Figure 5.6:	Pratt & Whitney blade velocity diagram at stall for 100 percent speed	125
Figure 5.7:	Typical first stage rotor inlet flow velocity diagram at the stall point of the three-stage compressor	127
Figure 5.8:	IGV row blade setting angle pattern - Equation (3.3), $\Delta\phi_1 = -16^\circ$, $\Delta\phi_2 = -8^\circ$, $n = 2$ cycles/rev	130
Figure 5.9:	Estimated rotor inlet flow angle for Equation (3.3), $\Delta\phi_1 = -16^\circ$, $\Delta\phi_2 = -8^\circ$, $n = 2$ cycles/rev	131
Figure 6.1:	Pratt & Whitney baseline versus modified compressor configuration performance	137
Figure 6.2:	Pratt & Whitney detailed measurement operating points for baseline compressor configuration	139
Figure 6.3:	Pratt & Whitney detailed measurement operating points for modified compressor configuration	140
Figure 6.4:	Pratt & Whitney detailed flow measurements at inlet, baseline, 50 percent speed	143
Figure 6.5:	Pratt & Whitney detailed flow measurements at inlet, baseline, 60 percent speed	143

Figure 6.6:	Pratt & Whitney detailed flow measurements at inlet, baseline, 70 percent speed	144
Figure 6.7:	Pratt & Whitney detailed flow measurements at inlet, baseline, 80 percent speed	144
Figure 6.8:	Pratt & Whitney detailed flow measurements at inlet, baseline, 90 percent speed	145
Figure 6.9:	Pratt & Whitney detailed flow measurements at inlet, baseline, 100 percent speed	145
Figure 6.10:	Pratt & Whitney detailed flow measurements at inlet, modified, 50 percent speed	146
Figure 6.11:	Pratt & Whitney detailed flow measurements at inlet, modified, 60 percent speed	146
Figure 6.12:	Pratt & Whitney detailed flow measurements at inlet, modified, 70 percent speed	147
Figure 6.13:	Pratt & Whitney detailed flow measurements at inlet, modified, 80 percent speed	147
Figure 6.14:	Pratt & Whitney detailed flow measurements at inlet, modified, 90 percent speed	148
Figure 6.15:	Pratt & Whitney detailed flow measurements at inlet, modified, 100 percent speed	148
Figure 6.16:	Pratt & Whitney detailed flow measurements at exit, baseline, 50 percent speed	149
Figure 6.17:	Pratt & Whitney detailed flow measurements at exit, baseline, 60 percent speed	149

Figure 6.18: Pratt & Whitney detailed flow measurements at exit, baseline, 70 percent speed	150
Figure 6.19: Pratt & Whitney detailed flow measurements at exit, baseline, 80 percent speed	150
Figure 6.20: Pratt & Whitney detailed flow measurements at exit, baseline, 90 percent speed	151
Figure 6.21: Pratt & Whitney detailed flow measurements at exit, baseline, 100 percent speed	151
Figure 6.22: Pratt & Whitney detailed flow measurements at exit, modi- fied, 50 percent speed	152
Figure 6.23: Pratt & Whitney detailed flow measurements at exit, modi- fied, 60 percent speed	152
Figure 6.24: Pratt & Whitney detailed flow measurements at exit, modi- fied, 70 percent speed	153
Figure 6.25: Pratt & Whitney detailed flow measurements at exit, modi- fied, 80 percent speed	153
Figure 6.26: Pratt & Whitney detailed flow measurements at exit, modi- fied, 90 percent speed	154
Figure 6.27: Pratt & Whitney detailed flow measurements at exit, modi- fied, 100 percent speed	154

NOMENCLATURE

<i>a</i>	polynomial coefficient for chromel-alumel thermocouple
<i>A</i>	compressor flow passage annulus area, ft^2 (m^2)
<i>c</i>	airfoil or rotor blade chord length, <i>in</i> (<i>cm</i>)
<i>D</i>	diameter, <i>in</i> (<i>m</i>)
<i>f</i>	frequency of pitching motion of dynamic stall airfoils, 1/s and frequency of periodic setting angle variation, 1/s
<i>g</i>	local acceleration of gravity, ft/s^2 (m/s^2)
<i>i</i>	blade incidence angle, °
<i>k</i>	ideal gas specific heat ratio
<i>K</i>	reduced frequency, $K = \frac{\pi fc}{V}$
<i>m</i>	maximum order of the chromel-alumel polynomial
<i>ṁ</i>	mass flowrate, <i>lb/s</i> (<i>kg/s</i>)
<i>M</i>	Mach number
<i>n</i>	number of setting angle variation cycles per rotor revolution, 1/rev
<i>N</i>	number of blades in stationary rows
<i>P</i>	absolute pressure, <i>lb/in²</i> (<i>N/m²</i>)
<i>P_{atm}</i>	barometric pressure, <i>lb/in²</i> (<i>N/m²</i>)
<i>PHH</i>	percent passage height from hub

Q	volume flow rate, ft^3/s (m^3/s)
r	radius from compressor axis, in (m)
R	gas constant, $\frac{ft \cdot lb_f}{lb_m \cdot ^\circ R}$ (kJ/kgK)
RPM	rotor rotational speed, rpm
S	circumferential space between blades, in (cm)
t	time, s
t	blade thickness, in (cm)
T	absolute temperature, $^\circ R$ (K)
U	rotor blade velocity, ft/s (m/s)
V	representative freestream speed of fluid past the airfoil, ft/s (m/s) and fluid relative velocity at rotor inlet, ft/s (m/s) and absolute fluid velocity, ft/s (m/s)
V_z	axial component of fluid velocity, ft/s (m/s)
w	rotor relative velocity, ft/s (m/s)
x	thermocouple emf voltage, volts
α	angle of attack, $^\circ$ and air flow angle, $^\circ$
β	absolute relative flow angle, $^\circ$
γ	blade stagger angle, $^\circ$
δ	deviation angle, $^\circ$ and $\frac{\text{total pressure at compressor inlet}}{\text{sea level standard pressure}}$
κ	blade metal angle, $^\circ$
θ	blade camber angle, $^\circ$ and $\frac{\text{total temperature at compressor inlet}}{\text{sea level standard temperature}}$
ρ	density of air, lb/ft^3 (kg/m^3)

σ	blade row solidity
ϕ	blade setting angle, °
ω	rate of airfoil pitching, rad/s
ϑ	fluid turning angle, °
% Imm.	percent immersion
Φ	flow coefficient
Ψ	total-head rise coefficient

Additional General Subscripts

<i>baro</i>	barometric
<i>baseline</i>	baseline compressor
<i>comp</i>	three-stage axial-flow compressor
<i>fan</i>	two-stage axial-flow fan
<i>hub</i>	annulus inner surface, hub
<i>i</i>	increment
<i>IGV</i>	inlet guide vane
<i>in stall</i>	in stall point
<i>inlet</i>	inlet
<i>max</i>	maximum
<i>mean</i>	annulus mean line
<i>min</i>	minimum
<i>modified</i>	modified compressor
<i>outlet</i>	outlet

<i>out of stall</i>	out of stall point
<i>recovery</i>	stall recovery point
<i>s</i>	static
<i>ss</i>	static stall
<i>stall</i>	stall point
<i>t</i>	total
<i>tip</i>	annulus outer surface, tip
<i>v</i>	venturi
1	amplitude and blade-row inlet
2	blade-row outlet
H_2O	water
θ	tangential direction

ABSTRACT

The useful operating range of the multistage, axial-flow compressor component of a gas turbine engine limits the extent of operation of that engine. Generally, the compressor stalls or surges at low flow rates and chokes at high flow rates. Thus, any improvement in the range between these compressor aerodynamic limits is normally of benefit to the engine also. An idea for delaying the onset of rotating stall in a multistage, axial-flow compressor which involved circumferentially varying the blade setting angles of stationary blades upstream of the compressor rotors was investigated. Tests involving two low-speed, multistage, axial-flow compressors and an intermediate-speed, three-stage, axial-flow compressor were completed. Comparisons between baseline compressor (circumferentially uniform setting angles) and modified compressor (circumferentially varying setting angles) performance data were made. A variety of blade setting angle circumferential variation patterns were tested. Test results suggest that rotating stall onset in the low-speed compressors could be delayed slightly but consistently with circumferentially varying setting angles. The low-speed compressor results indicated that a small improvement in stall recovery was also possible. The intermediate-speed compressor data indicated that there was a slight stall margin improvement at low compressor rotational speeds only. At higher rotational speeds no improvement was noticed.

1. INTRODUCTION

The compressor is one of three primary components of a gas turbine engine, along with the combustor and turbine. Of these components, the compressor has certain aerodynamic limits which usually set the range of operation of the engine. The compressor is limited by choking at higher flowrates and by stall or surge at lower flowrates. In Figure 1.1 from Copenhaver [1] is illustrated the stall-limit line which is defined as a line that connects the compressor operating points, for different speeds, at which stall or surge is likely to occur with any further decrease in flowrate. Because stall and surge are aerodynamic instabilities, the stall-limit line generally represents the boundary between stable and unstable operation of the compressor. To avoid compressor stall or surge, a sufficient stall margin is desired. Stall margin is a measure of how much the compressor back pressure can be increased from the design value at a constant flow and variable speed or how much the flowrate can be reduced from the design value at a constant speed before the compressor stalls.

The research described in this dissertation involved an effort to improve compressor stall margin by scheduling the blade setting angles of stationary blades upstream of a rotor in a circumferentially periodic pattern to delay the onset of rotating stall. Shifting the throttle line away from the stall-limit line is not generally acceptable because of the performance penalties involved. Achieving more operating margin by

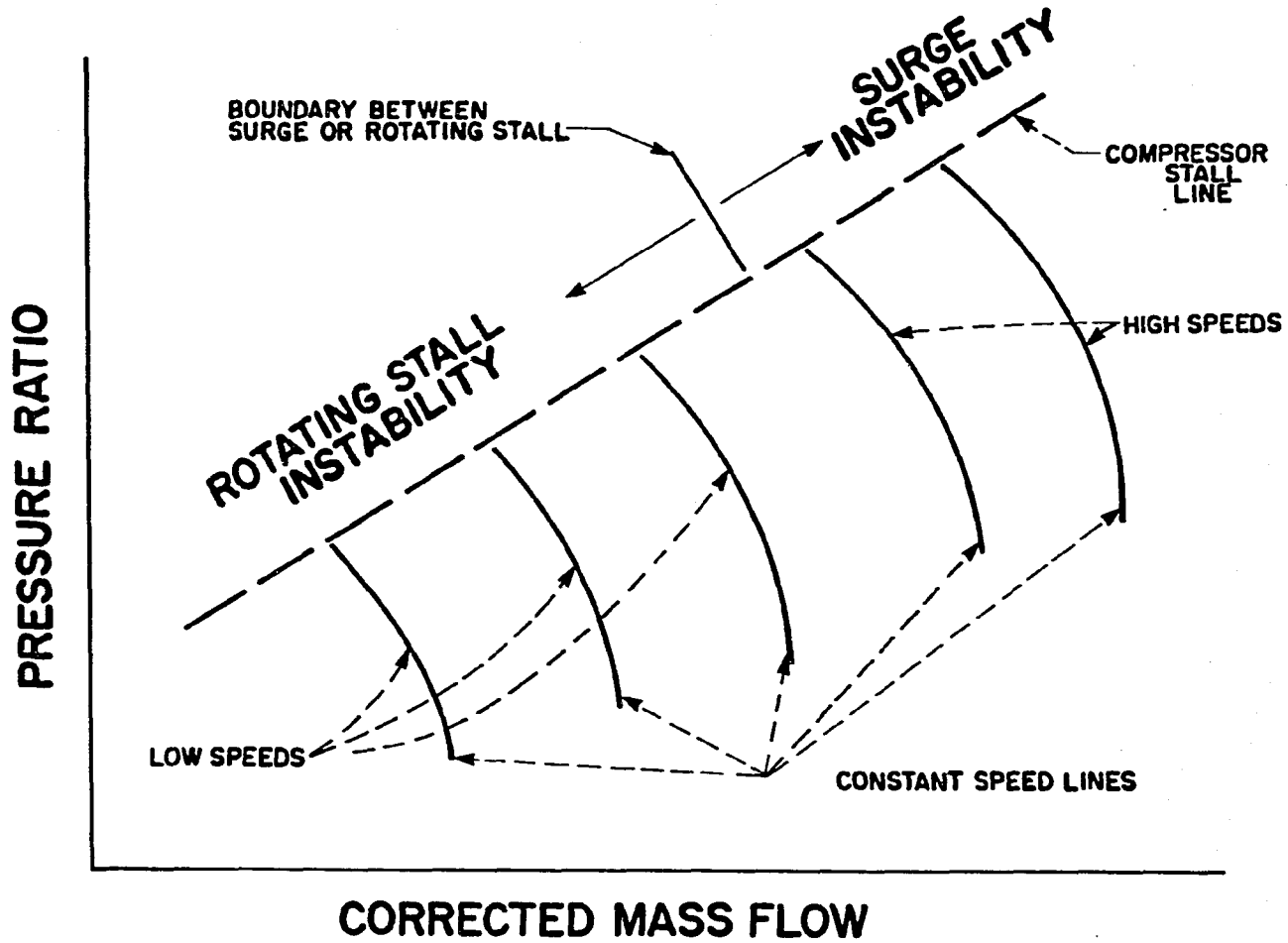


Figure 1.1: Compressor surge/rotating stall boundary, Copenhaver [1]

shifting the stall-limit line further away from the throttle line is attractive if it can be done without compromising other operating characteristics of the compressor.

It is important to understand some of the physical mechanisms of stall and surge. Stall and surge are two distinct aerodynamic flow instabilities which can occur during the operation of a multistage compressor. Stall is generally described as the unsteady separation of flow from blade surfaces and/or end walls resulting in rotating low-flow or localized reversed flow regions. Rotating stall typically occurs at lower compressor rotational speeds. Surge, in contrast, is characterized by global fluctuations in mass flow throughout the entire compressor. Surge is generally encountered at higher compressor rotational speeds and is easier to recover from than stall. Although these flow instabilities are distinct, they are related. It is known that surge is generally a result of the more localized instability of stall.

It is of great importance to compressor users to be able to understand, detect and avoid the instabilities of stall and surge. Not only do these instabilities limit compressor and engine performance. They can also cause damage to the compressor blading. The unsteady nature of these instabilities leads to large periodic forces being placed on the blades. The flow reversals associated with surge can introduce hot combustion gas into the compressor. Another important reason to avoid stall and surge is that these instabilities result in significant compressor and engine performance deterioration. The engine performance may actually fall below the level necessary to sustain flight. In the following two sections some of the physical mechanisms of stall and surge are described in further detail.

1.1 Stall

The first and most common flow instability encountered in multistage compressor operation is stall. For the present study, particular attention was focused on the flow mechanisms of rotating stall which are well known and documented. As mentioned earlier, low-flow and locally reversed flow regions occur as a result of separation from blade surfaces and/or end walls. The propagation rate of stall and extent of compressor annulus area stalled, however, are subject to the particular compressor design and operating conditions. A physical description of the process of rotating stall is outlined in reference [2] and summarized here. In Figure 1.2 is shown a cascade of rotor blades with the direction of rotation noted. If all of the blades are operating near stall and one of them, blade 2, does stall, a retarded flow region (or low-flow region) will occur upstream of blade 2. This local region of retarded flow will tend to direct flow towards rotor blades 1 and 3. The resulting larger incidence angle perceived by rotor blade 3 tends to stall it because it was near stall to begin with. The lowered incidence flow for rotor blade 1 unloads this blade. Once rotor blade 3 stalls, the retarded flow produced upstream of this blade will unstall rotor blade 2. This process continues as described propagating in the direction shown. The stall cell typically covers a portion of the annulus area and rotates circumferentially at a fraction of the compressor speed in the direction of rotation (perceived from an absolute frame of reference). Figure 1.3 from Greitzer [3] shows a fully developed rotating stall cell as seen from the front of the compressor.

Rotating stall may be classified as either "progressive" or "abrupt" rotating stall depending on the stage performance characteristic involved. A "progressive" rotating stall stage performance characteristic is smooth and continuous in the stall

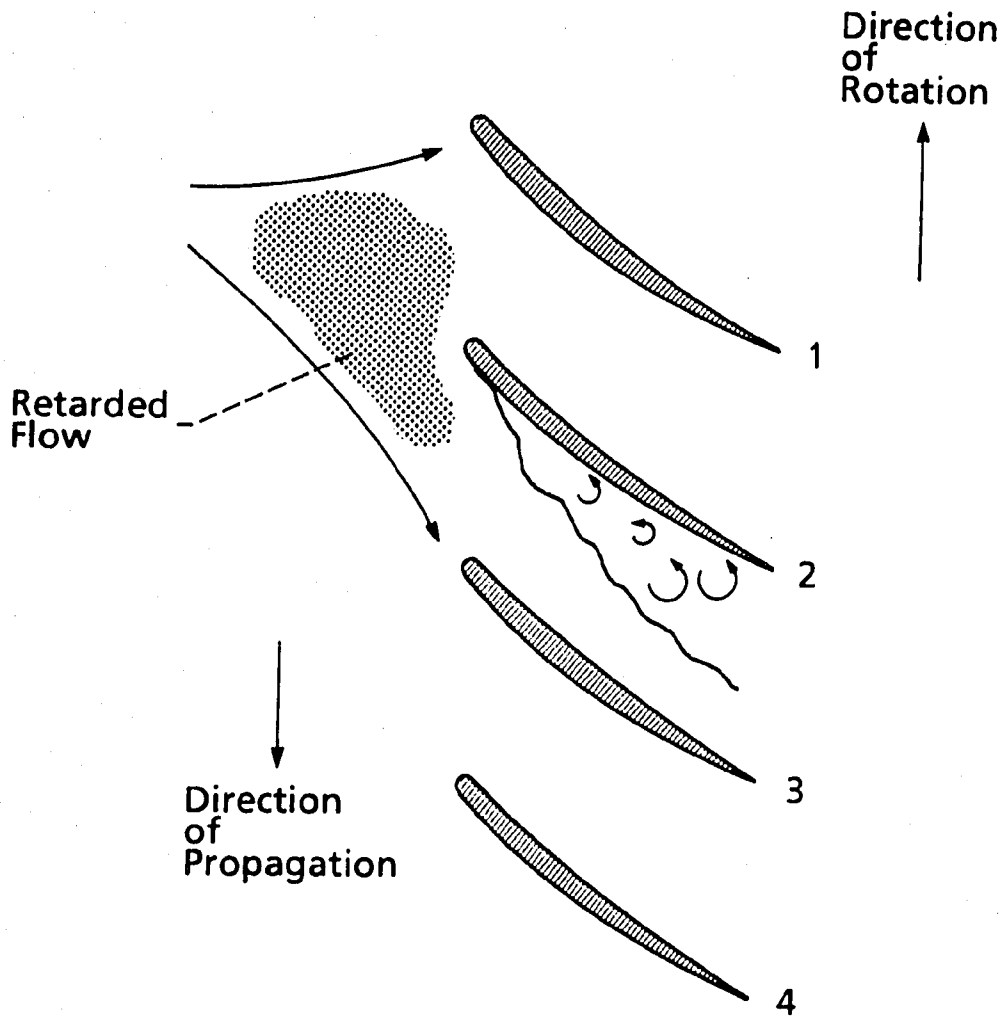


Figure 1.2: Propagation of stall in a cascade [2]

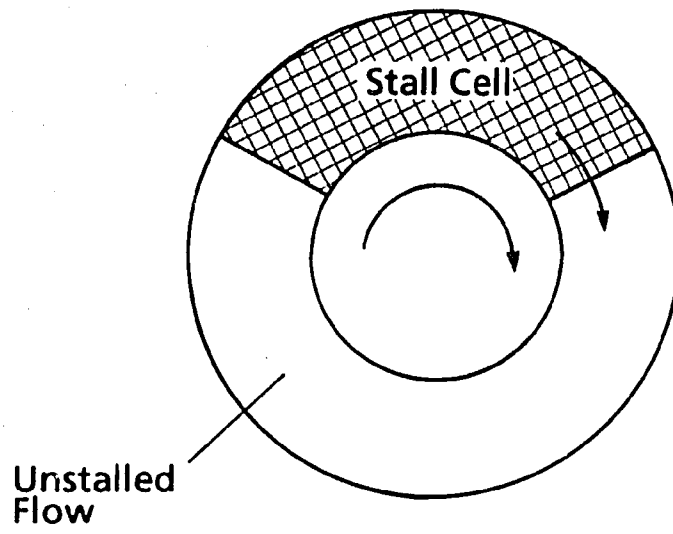


Figure 1.3: Fully developed rotating stall cell [3]

region indicating a gradual increase in blocked annulus area due to stall. In contrast, an "abrupt" rotating stall characteristic is discontinuous in the stall region due to the stall cell zone covering a larger portion of the annulus area.

Whether "progressive" or "abrupt", there is a significant loss in performance when a compressor is operating in rotating stall. A decrease in pressure rise and flowrate occur as a result of flow separation and annulus area blockage. Once the compressor operates in the fully stalled condition, the process of relieving this situation involves a hysteresis effect. The process of recovering from rotating stall at constant speed involves increasing the flowrate by opening the compressor throttle. The flowrate is increased until the compressor operating point is again on the unstalled characteristic line. The flowrate required to unstall the compressor is typically larger than the in-stall flowrate. In the case of a multistage device, significant unthrottling may be necessary to totally unstall the compressor. For reasons mentioned earlier, the in-stall operation of a compressor is undesirable and should be avoided; if encountered, it should be recovered from as quickly as possible.

1.2 Surge

A second type of instability common in multistage compressor operation is surge. Compressor surge is characterized by large amplitude oscillations of annulus average mass flow and system pressure rise. As mentioned earlier, the global instability of surge is generally a result of the localized instability of stall. During compressor surge, the compressor operating point may pass in and out of a rotating stall as well as a totally reversed flow regime and a steady-state operating condition. There are two main types of surge, namely, surge due to progressive stall and surge due to abrupt

stall. Surge due to progressive stall, is generally mild and inaudible when encountered in multistage compressor operation. Experimental investigations indicate that this type of surge occurs when there are no abrupt changes in the pressure ratio due to stall. Tests indicate that the total-pressure fluctuations measured may be only 15 to 20 percent of that encountered when the compressor surges abruptly. Whereas surge due to progressive stall is mild and inaudible, surge due to abrupt stall is violent and very audible. In fact, certain surge cycles observed in jet engine operation can cause flames from the combustion chamber to exit from the front of the compressor. This situation is very undesirable. Examination of actual data indicates that large pressure fluctuations can exist at the compressor discharge which may be up to 75 percent of the compressor pressure rise at the surge point.

The importance of detecting and avoiding stall and surge was mentioned earlier. When the compressor is subjected to periodic forces as a result of rotating stall or surge, a significant loss in performance is realized and blade failure may occur. In general, avoiding these instabilities, or if encountered, recovering quickly, are worthwhile objectives. In the following section, some of the current methods being investigated to avoid stall or surge, including extending the useful operating range of the compressor are considered.

1.3 Avoiding Stall

Current methods for avoiding stall or surge can be broken down into two major categories, static control and active control. Some static control methods for avoiding stall include designing blades with a higher tolerance to stall (higher diffusion limits), using boundary layer control methods such as vortex generators, suction, and blowing,

and using casing treatments, and using existing control variables such as compressor rotational speed and mass flow. Active control of rotating stall involves utilizing a feedback control loop coupled to a variable geometry feature of the compressor to avoid or recover from stall.

Static control methods for avoiding stall are somewhat limited as compared to active control methods for improving the useful operating range of the compressor. Although blades are being designed with a higher tolerance to stall, improvements in design cannot satisfy increased demands associated with improved compressor stall resistance. The static methods using boundary layer control have also enjoyed limited success only because the boundary layer cannot be altered enough. The final method of static control, varying compressor rotational speed and flowrate, is also very limited in its scope as a potential for avoiding stall. During compressor operation, the rotational speed and flowrate are often set parameters which cannot be altered quickly enough to reach a more stable operating point. The active methods of avoiding stall and surge have been significantly more successful in controlling these instabilities and extending the useful operating ranges of compressors. A. H. Epstein, a professor of Aeronautics and Astronautics at MIT, envisions a multistage compressor in which there is a microprocessor in every blade [4]. Commonly known as "smart" engine technology, the idea is that the microprocessor senses local flow conditions (velocity, pressure, etc.) and sends a feedback control signal to a computer processor. If the local flow conditions indicate that an instability is about to occur, the computer processor will send a signal to actuate some variable geometry feature of the compressor to avoid the instability. Some possible variable geometry features that have been considered are bleed doors, adjustable inlet guide vanes and stators, flaps on

inlet guide vanes, and even recamberable blades. Although these variable geometry features can add weight to the compressor, the trade-off in improved performance and stability make them attractive.

The proposed method for improving the stall margin of a multistage, axial-flow compressor considered in this dissertation is classified as a static method which could become a component of an active system. The method utilizes a circumferential variation of stationary blade setting angles to create a specific flowfield variation for the downstream rotor. The method is based on airfoil dynamic stall results which suggest that an airfoil oscillating about an axis perpendicular to the blade section can achieve angles of attack (average and instantaneous) that are higher than its static stall angle of attack. When the blade is oscillated at certain angle amplitudes and frequencies, its dynamic stall angle of attack may be as much as 20 percent higher than its static stall angle of attack. The intent of the circumferential variation in stationary blade setting angles is to produce a flowfield for the downstream rotor blades that is similar to the flowfield of an oscillating airfoil. By making the rotor flowfield similar to that of an oscillating airfoil, the rotor is expected to achieve higher instantaneous and average angles of attack before stalling. The higher angles of attack achieved allow the rotor to be loaded more without stalling and thus previously unattainable low flowrates can be realized before stall occurs. This reduction in the compressor flowrate before stall occurs corresponds to an increase in the useful operating range of the compressor and thus stall margin which is the intent of the method. In the following chapter airfoil dynamic stall research and how it can be extended to multistage, axial-flow compressor operation is discussed. Some possible

limitations associated with extending dynamic stall research concepts to compressor operation are also outlined.

2. RELATED ISOLATED AIRFOIL DYNAMIC STALL RESEARCH

The idea for modifying the stall margin of axial-flow compressors by circumferentially varying the setting angles of stationary blades upstream of a rotor stems from airfoil dynamic stall research. Dynamic stall research involves studies performed on airfoils pitching harmonically about an axis perpendicular to the blade section. Helicopter rotor blade development has led to several airfoil dynamic stall studies that suggest that a pitching blade, whose setting angle is varied periodically over a range of values, is able to sustain without stalling, angles of attack (instantaneously and on an average basis) that are larger than the static (stationary blade) stall angle. The increased stalling angle (average) of the airfoil can be credited to the oscillatory nature of the airfoil. The basic idea is that although the blade becomes highly loaded as it periodically cycles to an angle greater than the static stall angle, it is subsequently relieved as it moves to angles less than the static stall angle. Results show that this increased stalling angle (average), also called the dynamic stall angle, may be as high as 20 percent greater than the static stall angle of attack.

For an axial-flow compressor to benefit from the dynamic stall effect, the flowfield for the rotor blade must be made similar to that of a harmonically oscillating airfoil. An attempt at accomplishing this is done by repositioning upstream stationary blade setting angles in a periodic pattern around the circumference. As the rotor blade

rotates around the circumference, it sees a varying relative angle of attack which is similar to the varying angle of attack that a pitching airfoil sees. The angle amplitude and frequency of the setting angle variation upstream results in a predetermined change in relative angle of attack and frequency of variation perceived by the rotor.

The concept described for improving the stall margin of axial-flow compressors using the dynamic stall effect is simplistic in that it does not account for possible differences existing between the two flowfields. Dynamic stall studies are largely two-dimensional flow studies performed on simple airfoil geometries with negligible three-dimensional flow effects. These three-dimensional effects are very much present in the complex flowfield of a compressor and they determine the performance of the compressor. Additional compressor effects not fully addressed by dynamic stall studies are the effects of increasing Mach number and lowering blade aspect ratio. Regardless of the differences which may exist in the two flowfields, dynamic stall studies lead to some important ideas that are worth examining.

From a two-dimensional standpoint, some of the important factors affecting the dynamic stall angle are:

1. Rate of airfoil oscillation
2. Amplitude of airfoil oscillation
3. Airfoil geometry
4. Airfoil Mach number

Perhaps the most important factor listed is the rate at which the airfoil pitches. The rate at which the airfoil pitches is usually non-dimensionalized and called the reduced frequency, K . The reduced frequency represents the ratio of the time required

for the fluid to pass over one-half blade chord to the time period of pitching motion of the airfoil. The reduced frequency is defined as follows:

$$K = \frac{\pi f c}{V} \quad (2.1)$$

where

f = frequency of pitching motion of dynamic stall airfoils

c = airfoil chord length

V = representative freestream speed of fluid past the airfoil

It is noteworthy that as $K \rightarrow 0$, the airfoil oscillation rate approaches the static limit (stationary airfoil) and the effect of oscillation is negligible.

The selection of the proper reduced frequency to use in the low-speed compressor tests was guided by data presented in some of the isolated airfoil dynamic stall studies. In Figure 2.1 is depicted a typical airfoil pitching about a midchord axis with some of the important parameters associated with airfoil dynamic stall studies noted.

The two-dimensional pitching airfoil data presented by McCroskey [5] indicate that the extent by which the static stall angle can be exceeded by an airfoil pitching angle amplitude without dynamic stall occurring increases with increased reduced frequency, reaching a maximum in the range of K from 0.30 to 0.35. In that study, an NACA 0012 airfoil was oscillated in pitching motion as indicated by the equation:

$$\alpha = \alpha_0 + \alpha_1 \sin \omega t \quad (2.2)$$

where

α = instantaneous angle of attack

α_0 = angle about which the airfoil pitches

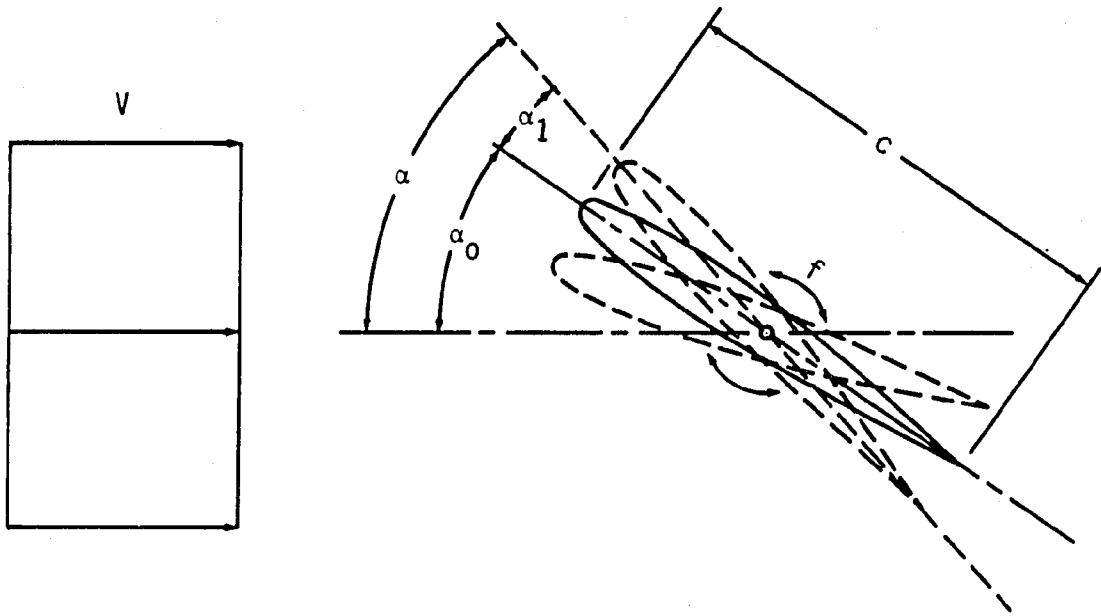


Figure 2.1: Typical airfoil pitching about a midchord axis

α_1 = amplitude of angle variation

ω = rate of airfoil pitching, $\omega = 2\pi f$

t = time

The three parameters: α_0 , angle about which the airfoil pitches; α_1 , amplitude of angle variation; and ω , rate of airfoil pitching, were varied over a range of values in an attempt to construct the experimental stall boundary for the NACA 0012 airfoil. In Figure 2.2 is a sketch of the airfoil geometry and some of the important angular positions associated with these tests. The data of Figure 2.3, including the experimental stall boundary, illustrate the extent by which the static stall angle can be exceeded without dynamic stall occurring anywhere in the cycle. The angle $\alpha_{s,s}$ represents the angle of attack for which static stall was observed. Thus, $\frac{\alpha_1}{\alpha_{s,s} - \alpha_0}$ is the amount by which the airfoil is oscillated past the static stall position, as illustrated in Figures 2.2 and 2.3. The open symbols denote absence of stall throughout the cycle, half-solid symbols denote test points for which stall was observed during some cycles and not during others, and the solid symbols denote complete stall during some part of every cycle. The resulting experimental stall boundary suggests that the delay of stall increases with reduced frequency, reaching a maximum in the range of reduced frequency, K , from 0.30 to 0.35. With further increases in the reduced frequency, no additional delay of stall was noticed.

The pitching airfoil data presented by Halfman, Johnson, and Haley [6] seem to verify and extend the results presented by McCroskey [5]. In their study, three different airfoil geometries (blunt, sharp, and intermediate wings) were oscillated in pitching motion as indicated by Equation (2.2). In their study, Halfman et al. performed tests at a constant amplitude of oscillation, α_1 , of 6.08° , and varied the

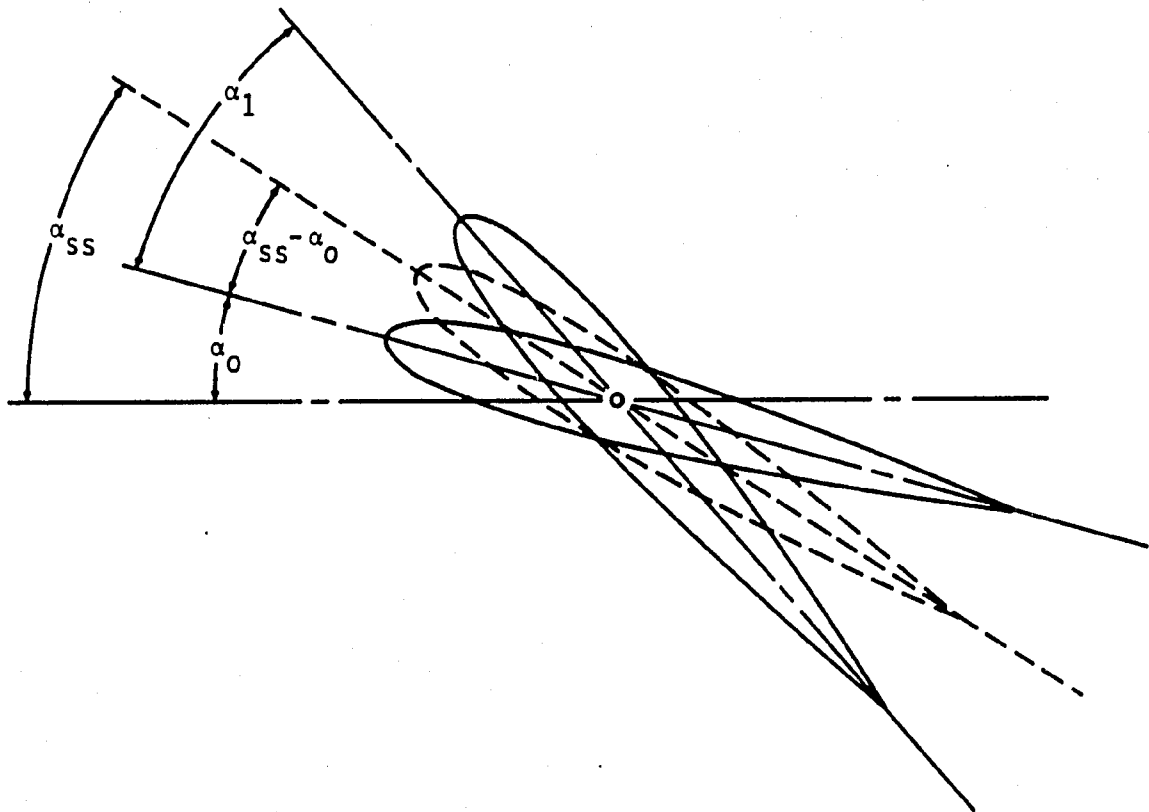


Figure 2.2: Airfoil geometry and important angular quantities. McCroskey [5]

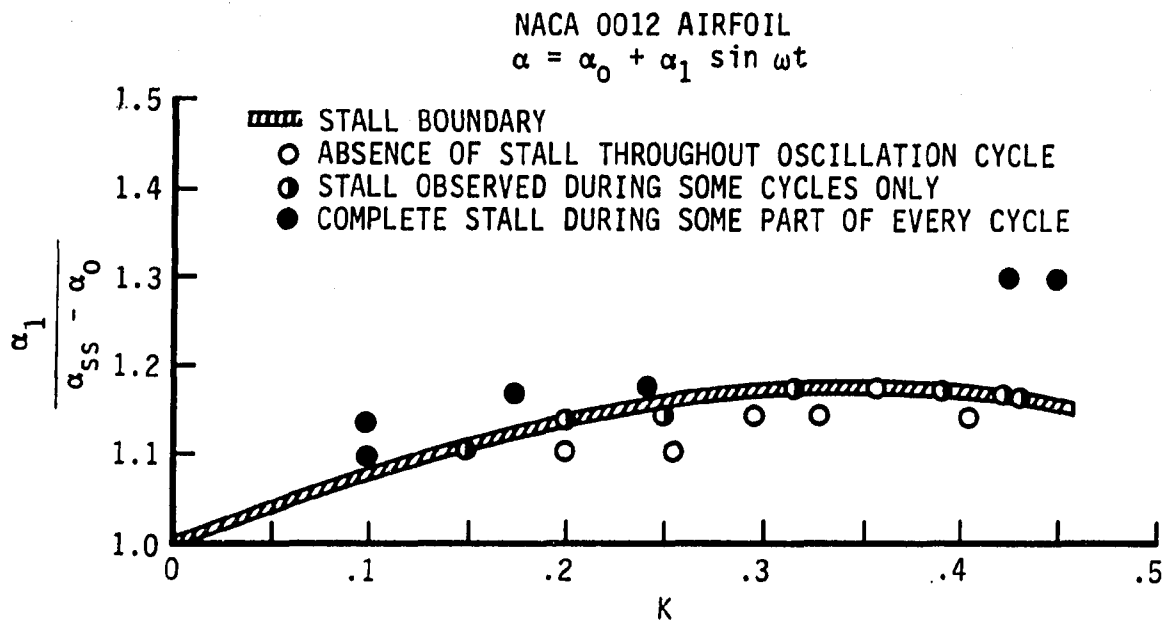


Figure 2.3: Experimental stall boundary according to McCroskey [5]

parameters α_o and K to determine the extent by which the static stall angle could be exceeded at various reduced frequencies. In addition, they also performed tests at different $\Delta\alpha$ values, where

$$\Delta\alpha = \alpha_o - \alpha_{ss} \quad (2.3)$$

In their report, Halfman et al. described the increase in the dynamic stall angle by the quantity:

$$\delta\alpha = \alpha_{stall} - \alpha_{ss} \quad (2.4)$$

where

α_{stall} = instantaneous stall angle of attack

α_{ss} = static stall angle of attack

The data in Figure 2.4 show the results of tests performed on the intermediate wing airfoil geometry and is a plot of $\delta\alpha$ versus the reduced frequency, K , for three different values of $\Delta\alpha$ (-2° , 0° , and 4°). The solid symbols denote the instantaneous angle of attack for which the intermediate wing stalled. The instantaneous stalling angle was determined from traces of the variation of moment in pitch throughout a cycle of oscillation and corresponds to the angle of attack at which the moment drops sharply. The open symbols indicate "no stall" occurring throughout the cycle of oscillation. The solid lines are curves that are faired through the data points for $\Delta\alpha$ values of -2° , 0° , and 4° . Additional plots showing similar trends were constructed by Halfman et al. for the remaining two wing airfoil geometries, blunt and sharp wings, but are not included here. It is evident from the information of Figure 2.4 that the quantity $\delta\alpha$ increases with larger reduced frequency and reaches a maximum in the range of K from 0.30 to 0.35, depending on the particular value of $\Delta\alpha$. In

INTERMEDIATE WING AIRFOIL

$$\alpha = \alpha_0 + \alpha_1 \sin \omega t$$

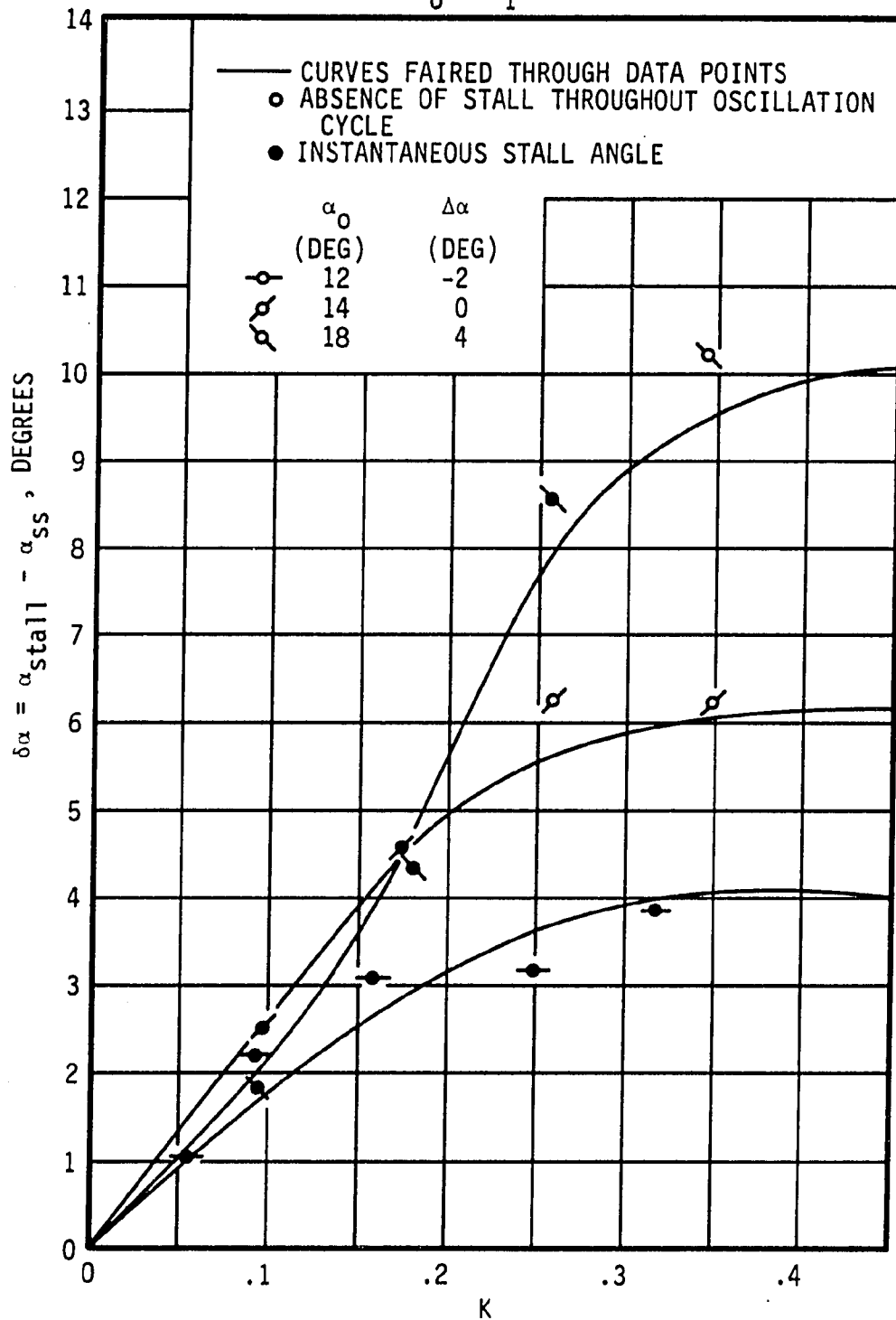


Figure 2.4: Dynamic stall angle increase as a function of K , Halfman et al. [6]

fact, the data point corresponding to $\delta\alpha = 10^\circ$ and $K = 0.35$ for $\Delta\alpha = 4^\circ$ involved no evidence of stall anywhere in the cycle. Thus, in tests where the intermediate wing airfoil oscillated about a nominal angle of attack (α_o) 4° above its static stall angle of attack (α_{ss}) with a pitching angle amplitude (α_1) of 6.08° , the airfoil showed no signs of stalling anywhere in the cycle at a reduced frequency, $K = 0.35$. This observation leads to the conclusion that a pitching airfoil can sustain average as well as instantaneous angles of attack that are larger than the static stall angle of attack at certain amplitudes of oscillation and reduced frequencies.

The studies performed on simple two-dimensional airfoil geometries by McCroskey [5] and Halfman et. al. [6] suggest that the maximum delay of stall occurs at a reduced frequency, K , in the range from 0.30 to 0.35. This range of reduced frequency was considered when initial attempts were made for improving the stall margin of two low-speed compressors.

Another parameter affecting the extent to which airfoils experience the dynamic stall phenomena is the amplitude of pitching motion, α_1 of Equation (2.2). According to McCroskey, Carr, and McAlister [7], the amplitude of pitching motion, α_1 , generally determines the characteristics of the time dependent aerodynamic forces and moments for a pitching airfoil. McCroskey further states that these aerodynamic quantities may be considerably larger and different in nature from their steady-state counterparts. Because the dynamic stall angle is usually determined from time dependent aerodynamic force and moment traces, the amplitude of pitching motion is very important. Past pitching airfoil experiments were performed over a wide range of pitch angle amplitudes. McCroskey [5] performed tests on an oscillating NACA 0012 airfoil section with a 4° to 19° range of pitching motion angle amplitude. Later,

McCroskey et al. [7] used an angle amplitude range of 6° to 14° . Experiments performed on different airfoil sections by Halfman et al. [6] were pitched at a constant angle amplitude of 6.08° . Other tests by McCroskey and Pucci [8] involved a 5° angle amplitude, while Liiva [9] performed tests with angle amplitudes in the range from 2.5° to 7.5° . The wide range of amplitudes of pitching motion mentioned in the studies cited above can be attributed to attempts by the authors involved to identify some of the stalling characteristics of pitching airfoils for different airfoil geometries. These values of pitching motion amplitude were considered in selecting the proper amplitude of blade setting angle variations for the low-speed compressor tests.

Another important feature affecting the increased stall angle of harmonically pitching airfoils is the airfoil geometry. Halfman et al. [6] concluded that the airfoil shape primarily affects the suddenness and type of flow separation under dynamic stalling conditions. Similarly, McCroskey et al. [7] and McCroskey and Pucci [8] stated that airfoil leading edge geometry has a strong affect on the type of boundary-layer separation that occurs. Liiva [9] contended that a cambered airfoil has better aerodynamic characteristics under dynamic stalling conditions because the adverse pressure gradient is decreased by nose camber. It is expected that the airfoil geometry as well as the compressor geometry will be important in determining the success of the method outlined for improving the stall margin of compressors. Simple two-dimensional airfoils sustaining increased angles of attack does not necessarily mean that a compressor rotor may achieve this as well. Further, as the rotational speed (and thus Mach number) increases, so does the effect of geometry on the overall performance of the compressor. For the low-speed compressor tests, the rotor of the two-stage axial-flow fan had minimal nose camber, while the British C4 section rotor

blades of the three-stage axial-flow compressor involved substantial nose camber.

The remaining parameter affecting dynamic stall is airfoil Mach number. The major effect of Mach number on the stalling characteristics of a harmonically pitching airfoil are leading edge effects and the corresponding separation type as mentioned by McCroskey and Pucci [8] and Liiva [9]. As with airfoil and compressor geometry, the Mach number is expected to be an important factor in the success of the method outlined in this dissertation. It may be that the effect of increasing Mach number in a compressor degrades the increased stalling angle found in the dynamic stall phenomena. Typical Mach numbers evaluated at the design point operating conditions for the two-stage fan and three-stage compressor were near 0.10. The Mach numbers associated with the stalling condition of the Pratt & Whitney compressor varied with rotational speed and were in the range from 0.08 to 0.21.

3. PROOF OF CONCEPT IN LOW-SPEED COMPRESSORS

The following chapter describes experimental tests performed at Iowa State University on two low-speed compressors, namely a two-stage, axial-flow fan and a three-stage, axial-flow compressor. These tests were used as a preliminary step in evaluating the potential for using circumferentially varying stationary blade setting angles to improve compressor stall margin. Descriptions of the two compressors, related equipment, experimental procedures and results are presented. This chapter also presents some detailed measurements taken with the three-stage compressor. The detailed measurements (flow angle and magnitude) were performed behind the inlet guide vanes of the baseline compressor configuration as well as some modified compressor configurations. These measurements provided additional information about the flowfield being produced by the blade setting angle variation upstream. Using the detailed flow information, comparisons were made between the estimated and actual reduced frequencies and rotor inlet flow angle variations for the low-speed compressor. The analysis of this preliminary work guided further attempts with an intermediate-speed, three-stage, axial-flow compressor.

3.1 Stationary Blade Setting Angle Variations

The main research objective was to determine the influence on stall point of circumferential variations of stationary blade setting angles involving different reduced frequencies and amplitudes of rotor inlet flow angle variation. Blade setting angle patterns could be changed easily in the two-stage fan and three-stage compressor. These pattern changes were not as easily accomplished in the Pratt & Whitney compressor because of its complexity. Three different blade setting angle variation patterns were evaluated in tests. These patterns consisted of sinusoidal, rectified sine-wave, and asymmetric variations of angles and are illustrated in Figure 3.1. The equations describing these angle schedules are given below:

Sinusoidal Variation:

$$\phi_i = \phi_o + \Delta\phi \sin \left[\frac{2n\pi}{N} (i - 1) \right] \quad (3.1)$$

where

ϕ_i = individual blade setting angle

ϕ_o = baseline blade setting angle

$\Delta\phi$ = amplitude of blade setting angle circumferential variation

n = number of setting angle variation cycles per rotor revolution

N = number of blades in stationary row

i = individual blade number

Rectified Sine-wave Variation:

$$\phi_i = \phi_o + \Delta\phi \left| \sin \left[\frac{2n\pi}{N} (i - 1) \right] \right| \quad (3.2)$$

where the parameters are explained above.

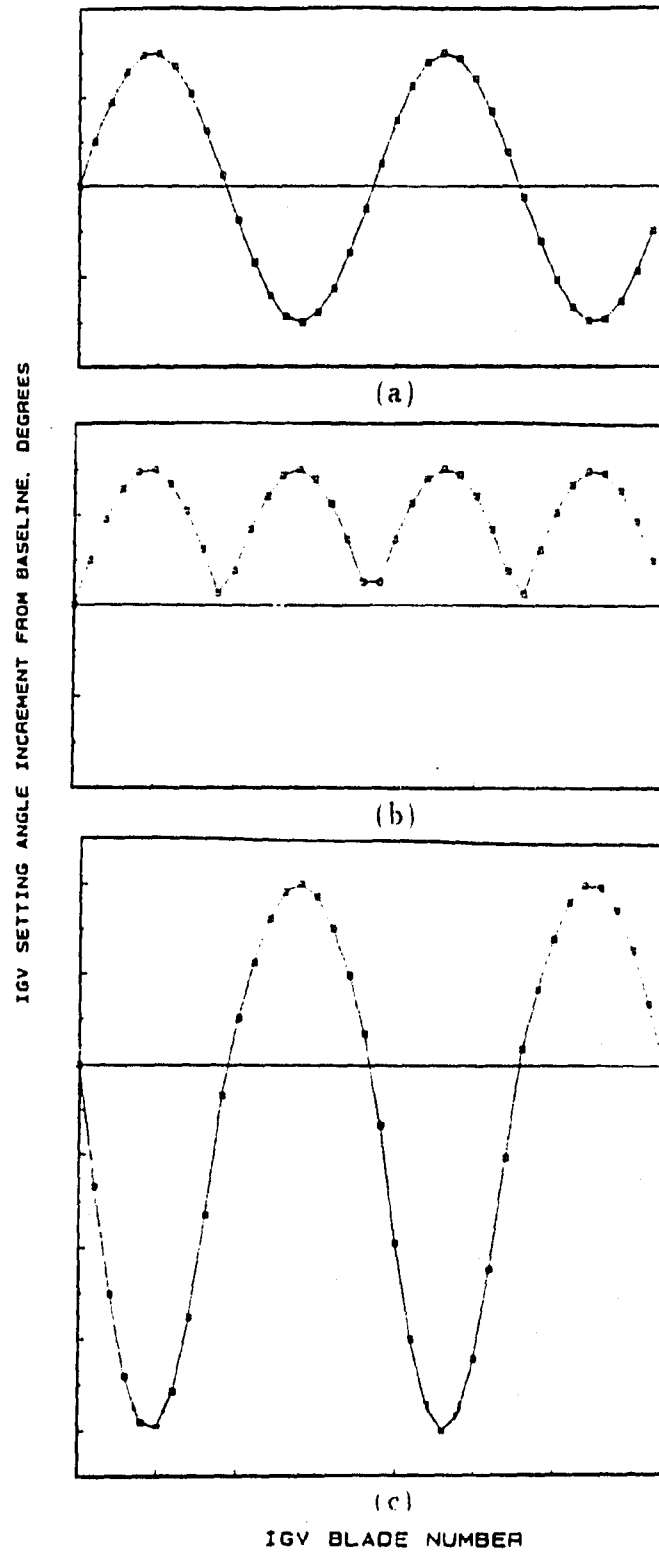


Figure 3.1: Blade setting angle variations, (a) Sinusoidal, (b) Rectified Sine-wave, and (c) Asymmetric.

Asymmetric Variation:

$$\phi_i = \begin{cases} \phi_o + \Delta\phi_1 \sin \left[\frac{2n\pi}{N} (i-1) \right] & \text{for } i=1-10, 20-28 \\ \phi_o + \Delta\phi_2 \sin \left[\frac{2n\pi}{N} (i-1) \right] & \text{for } i=11-19, 29-37 \end{cases} \quad (3.3)$$

where $\Delta\phi_1$ and $\Delta\phi_2$ are different amplitudes of blade setting angle circumferential variation and the number of setting angle variation cycles per rotor revolution, n , was set at 2, for 37 blades in a stationary row.

The two-stage fan tests involved only sinusoidal variations in blade setting angle while during the three-stage compressor tests, all three kinds of variations in blade setting angle were used. The Pratt & Whitney compressor tests were accomplished with only one asymmetric variation in blade setting angle.

The intent of the circumferential variations in stationary blade setting angle was to create a variation in inlet flow angle amplitude and frequency for a downstream rotor blade row. The amplitude of setting angle variation, $\Delta\phi$, resulted in a specific rotor inlet flow angle variation and the number of setting angle variation cycles per rotor revolution, n , gave the frequency of the variation. The frequency of the periodic variation imposed on each downstream rotor blade was given by the following equation

$$f = \frac{n(RPM)}{60} \quad (3.4)$$

where

f = frequency of circumferentially periodic setting angle variation

n = number of setting angle variation cycles per rotor revolution

RPM = rotor rotational speed

Substituting Equation (2.1) into Equation (3.4) and rearranging gives an estimate for

the number of setting angle variation cycles, n , to be used in the compressor tests.

$$n = \frac{60KV}{\pi c(RPM)} \quad (3.5)$$

where

K = reduced frequency

V = representative midspan fluid relative velocity at rotor inlet

c = rotor blade chord length

Values of reduced frequency, K , reported in the literature on dynamic stall for which the maximum delay of dynamic stall seemed to occur were used in calculating n . For a given compressor geometry and set of test conditions, Equation (3.5) gives an appropriate value of the frequency of setting angle variation cycles per rotor revolution. The value of n used must be an integer value in order to preserve the periodic nature of the blade setting angle variation and thus, the value calculated with Equation (3.5) was rounded to the nearest integer value.

3.2 Two-Stage Axial-Flow Fan

Presented in Figure 3.2 is a sketch of the General Electric, two-stage, low-speed, axial-flow fan research apparatus. The configuration of the fan consisted of two identical stator-rotor stages which could be tested as either a one-stage or two-stage unit. The blade rows were within an annulus having constant hub (12.36 in. (0.314 m)) and tip (18.00 in. (0.457 m)) diameters, resulting in a hub/tip radius ratio of 0.687. All stationary blade rows had the same number of blades (37) and were cantilever mounted on the outer casing flange. Individual blade setting angles could be easily changed. The rotor blade rows each included the same number of blades (24) that were securely mounted on the hub flange. The stator blades were constructed of sheet steel using a circular-arc profile while the rotor blades were cast out of an aluminum alloy and involved RAF-#6 propeller blade sections. A blade-to-blade view of the two-stage, axial-flow fan blade rows is shown in Figure 3.3. Important blade characteristics are summarized below:

Number of blades per row	stator rows - 37, rotor rows - 24
<u>Stationary blade details:</u>	
Blade span (constant)	2.80 in. (7.11 cm.)
Blade chord (constant), c	1.75 in. (4.44 cm.)
Blade section thickness/chord ratio, t/c	6 %
Blade setting angle	26.0° @ $r = 7.59$ in.
<u>Rotor blade details:</u>	
Blade span (constant)	2.80 in. (7.11 cm.)
Blade chord (constant), c	1.70 in. (4.32 cm.)

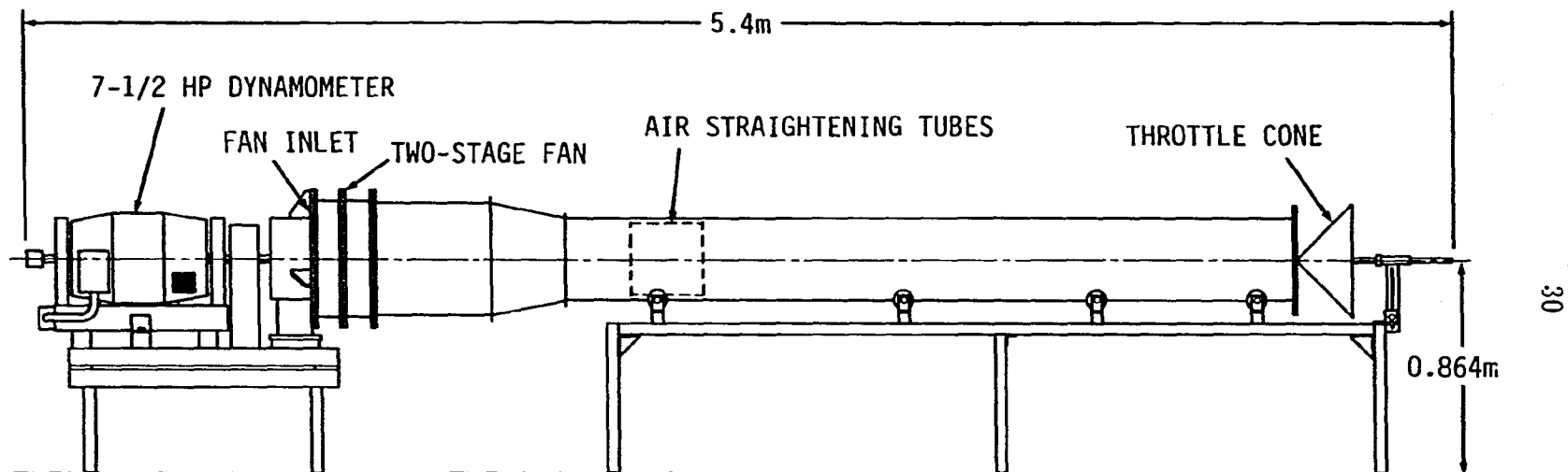


Figure 3.2: Two-stage axial-flow fan apparatus

Blade section maximum thickness/ chord ratio, t_{max}/c	12 %
Blade setting angle	65.0° @ $r = 7.59$ in.

The two-stage, axial-flow fan was driven by a $7\frac{1}{2}$ HP cradled D.C. dynamometer. Variable voltage control for the dynamometer was provided by a General Electric speed variator which permitted testing within a range of shaft speed from 500 rpm minimum to 3000 rpm maximum. Rotor speed was measured with a frequency counter mounted on the dynamometer shaft. A General Electric voltage variac was added to the control circuitry of the GE speed variator to enable the rotor speed to be adjusted and held constant to within ± 2 rpm. Rotational speed was measured with a frequency counter mounted on the dynamometer shaft. Further details about the two-stage, low-speed, axial-flow fan may be found in reference [10].

3.2.1 Two-stage fan performance tests

With the two-stage fan, one-stage and two-stage overall performance tests involving different circumferential variations of stator blade setting angles were performed at shaft speeds of 2000 rpm and 1600 rpm, respectively. Circumferential variations in stationary blade setting angle set in the two-stage fan builds involved resetting both stationary rows of the fan with identical blade setting angle variations. The stator rows were aligned axially so that the identical variations were in phase geometrically.

The overall performance characteristics of the fan, namely, fan head-rise and flowrate, were measured and non-dimensionalized into the total-head rise coefficient and flow coefficient shown in Equations (3.6) and (3.7). The fan head-rise was measured with a wall static pressure ring located one fan diameter downstream of the

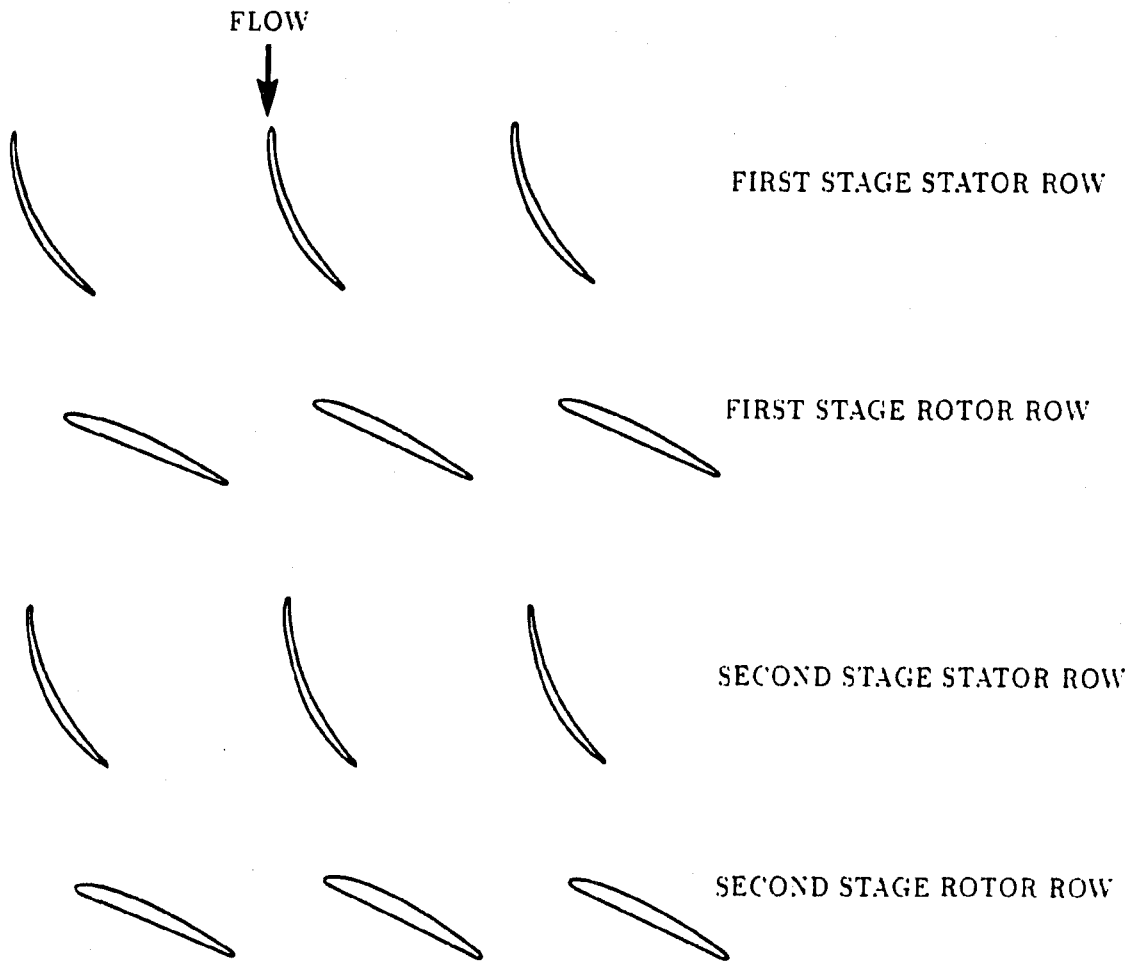


Figure 3.3: Blade-to-blade view of two-stage, axial-flow fan blade rows

fan exit. The fan flowrate was measured with a pitot-tube traverse of five equal areas located in the downstream ductwork.

$$\Psi_{fan} = \frac{\Delta P + \rho V^2 / 2}{\rho (RPM)^2 D^2} \quad (3.6)$$

$$\Phi_{fan} = \frac{\bar{V}_z}{U_{tip}} \quad (3.7)$$

The stall point for the two-stage fan was determined by listening for the unmistakable sound produced by the stalling fan. The fan flowrate was slowly reduced using fractional turns of the fan cone shaped throttle. With each turn, overall performance data were collected. The data taken before the audible detection of stall were considered to be for the stall point operating condition. Because stall point data were consistent throughout a data run and did not vary significantly from run to run or from day to day, it was felt that the error band for these measurements was within the symbol used.

3.2.2 Axial-flow fan results

The General Electric, two-stage axial-flow fan was tested in a variety of configurations and the results are presented in this subsection. Values of reduced frequency, K , at the stall limit for several of the GE fan one-stage and two-stage configurations tested are summarized in Table 3.1. Also included in Table 3.1 are brief comments about the stall limit observed.

Single-stage results presented in Table 3.1 suggest that as the amplitude of blade setting angle, $\Delta\phi$, was increased from 1° to 5° , (with the reduced frequency at stall remaining constant) the stall margin was also increased. Comparison of single-stage builds where $\Delta\phi = 5^\circ$ and $\Delta\phi = 7^\circ$ showed no additional increase in the stall margin

Table 3.1: Summary of two-stage fan builds and results

Number of stages	Estimated reduced frequency at stall, K_{stall}	Blade setting angle amplitude $\Delta\phi, ^\circ$	Tests results
1	0.3	1	no discernible change from baseline
1	0.3	3	slight increase in stall margin with a decrease in head rise coefficient
1	0.3	5	modest increase in stall margin with a decrease in head rise coefficient Figure 3.4
1	0.3	7	modest increase in stall margin with a decrease in head rise coefficient
2	0.3	5	modest increase in stall margin with no change in head rise coefficient Figure 3.5
2	0.6	5	no discernible change from baseline
2	0.3	7	slight increase in stall margin with a slight decrease in head rise coefficient
2	0.2	7	no discernible change from baseline

suggesting that an optimum blade setting angle amplitude was reached. Shown in Figure 3.4 is a comparison of one-stage baseline performance and modified compressor performance in which a sinusoidal variation in blade setting angle was used. The modified performance shows a slight drop in head rise but also an increase in stall margin. This increase in stall margin was modest at best but was very repeatable.

Two-stage fan tests proceeded with the amplitude of setting angle variation set in the range of optimum results seen with the one-stage variations. A comparison of data for two-stage builds involving a reduced frequency at stall held constant at a value of 0.3 and the blade setting angle amplitudes varying from 5° to 7° , suggests a decrease in stall margin with an increase in angle amplitude. Results of Table 3.1 also suggest that when the reduced frequency was doubled to 0.60 or reduced to 0.20 no additional increase in stall margin was noticed. This indicated that the optimum reduced frequency was near a value of 0.30. Shown in Figure 3.5 is a comparison between two-stage baseline compressor and modified compressor performance in which a sinusoidal variation in blade setting angle was used. The figure illustrates the improvement in stall margin with no degradation in overall compressor head-rise. Again, the improvement in stall margin was modest but very repeatable.

The results obtained by simple tests performed on the one-stage and two-stage configurations of the GE axial-flow fan led to some important observations. The relative magnitude of stall margin increase seemed to be most noticeable when the reduced frequency value at stall, K_{stall} , was near 0.3 and the stator blade setting angle amplitude, $\Delta\phi$, was in the range from 5° to 7° . Further, because of the small differences in performance involved it was important to confirm all results by repeating

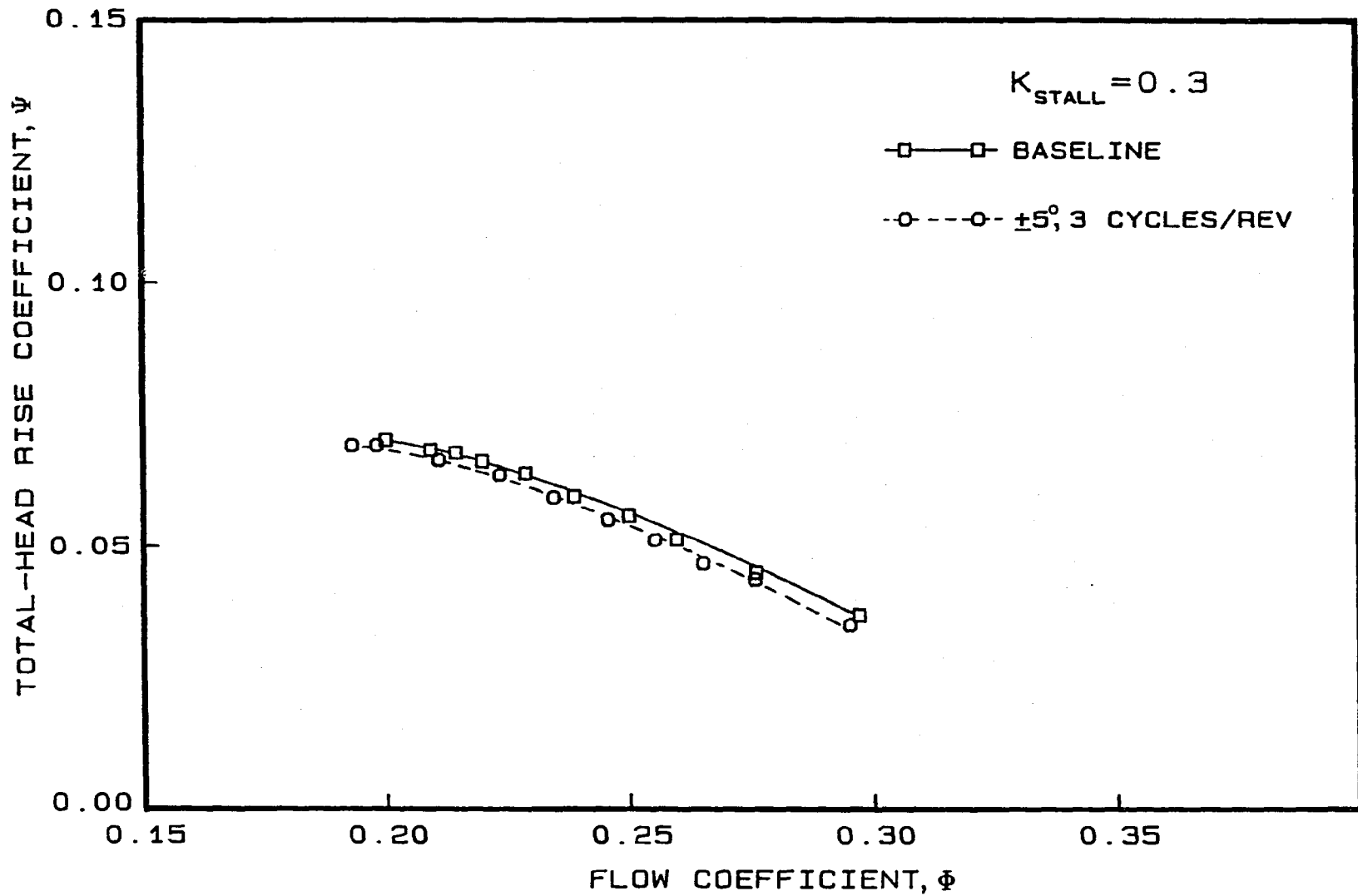


Figure 3.4: One-stage axial-flow fan results, $\Delta\phi = 5^\circ$, $n = 3$ cycles/rev, rotor speed = 2000 rpm

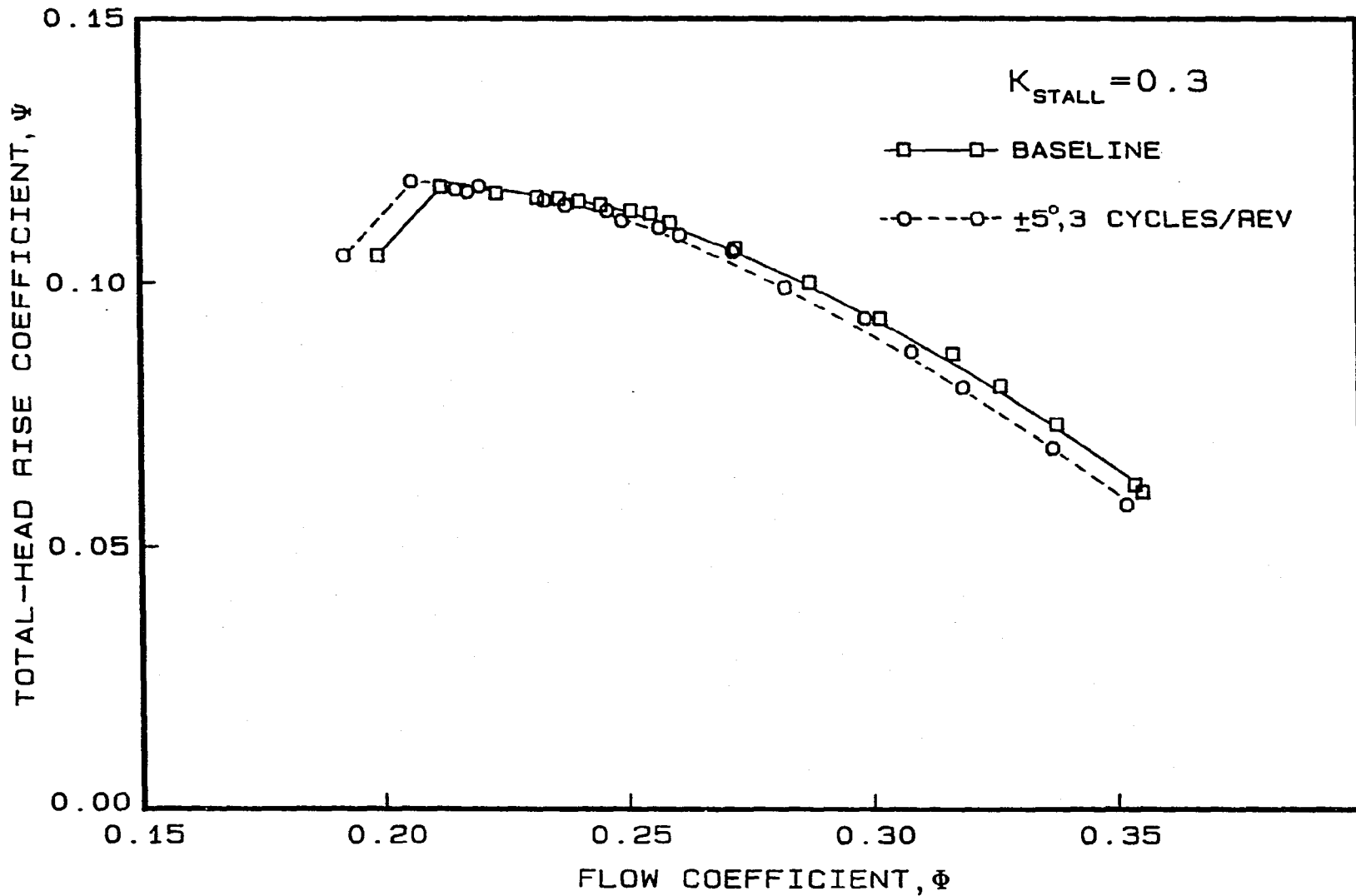


Figure 3.5: Two-stage axial-flow fan results, $\Delta\phi = 5^\circ$, $n = 3$ cycles/rev, rotor speed = 1600 rpm

tests several times. Finally, the benefit of multistage operation is shown by comparing one-stage and two-stage fan tests. Test results suggest that the loss in head-rise is more pronounced for the one-stage fan tests than the two-stage fan tests. The stall margin increases for the two-stage configurations seemed to be slightly higher than those for the one-stage configurations.

3.3 Three-Stage Axial-Flow Compressor

In Figure 3.6 is a sketch of the three-stage, low-speed, axial-flow compressor apparatus used in the experimental investigation. A smooth gradually contracting inlet to the compressor guided the flow entering the inlet guide vane (IGV) row and three downstream sets of rotor-stator stages. A blade-to-blade view of the three-stage, axial-flow compressor blade rows is shown in Figure 3.7. The IGV row and the three identical rotor-stator stages were within an annulus having constant hub (11.22 in. (0.285 m)) and tip (16.00 in. (0.406 m)) diameters, resulting in a hub/tip radius ratio of 0.702. All stationary blade rows had the same number of blades (37). These blades were cantilever mounted from the outer annulus wall on separate ring assemblies which could be moved circumferentially either independently or in groups. The rotor blade rows each included the same number of blades (38) that were attached on rings on a common drum with corresponding blade stacking axes aligned axially. All of the blades were constructed of a plastic material (Monsanto ABS) with British C4 sections stacked to form a free vortex design.

Overall blade characteristics for the three-stage, low-speed, axial-flow research compressor are summarized below:

Number of blades per row	IGV and stator rows - 37, rotor rows - 38
<u>IGV blade details:</u>	
Blade span (constant)	2.40 in. (6.10 cm)
Blade chord (constant), c	1.20 in. (3.05 cm.)
Blade section maximum thickness/ chord ratio, t_{max}/c	10 %

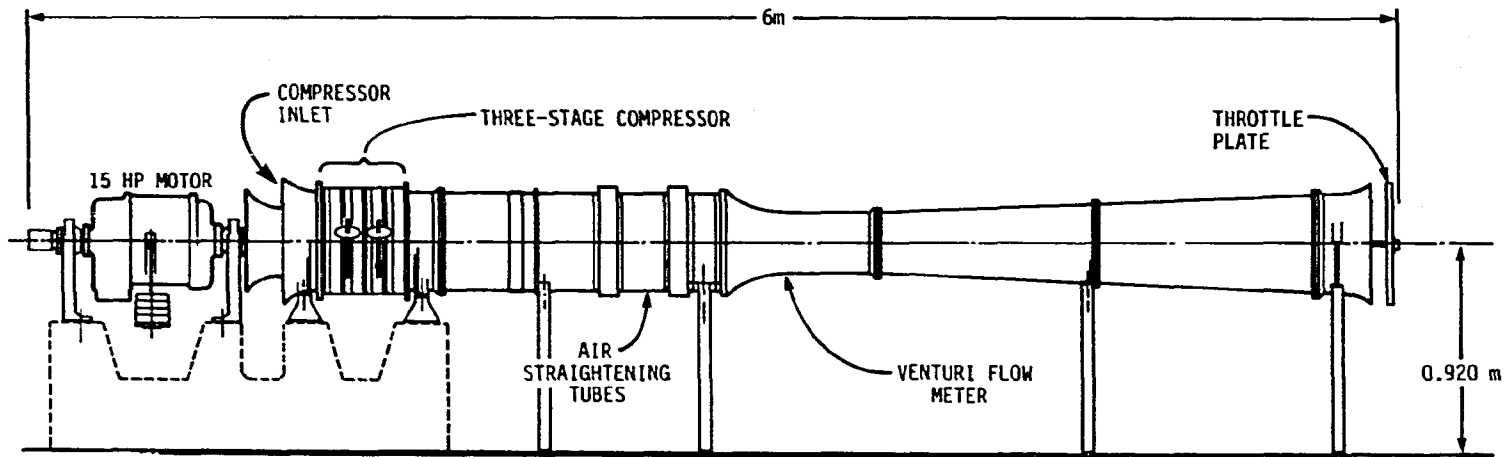


Figure 3.6: Three-stage axial-flow compressor apparatus

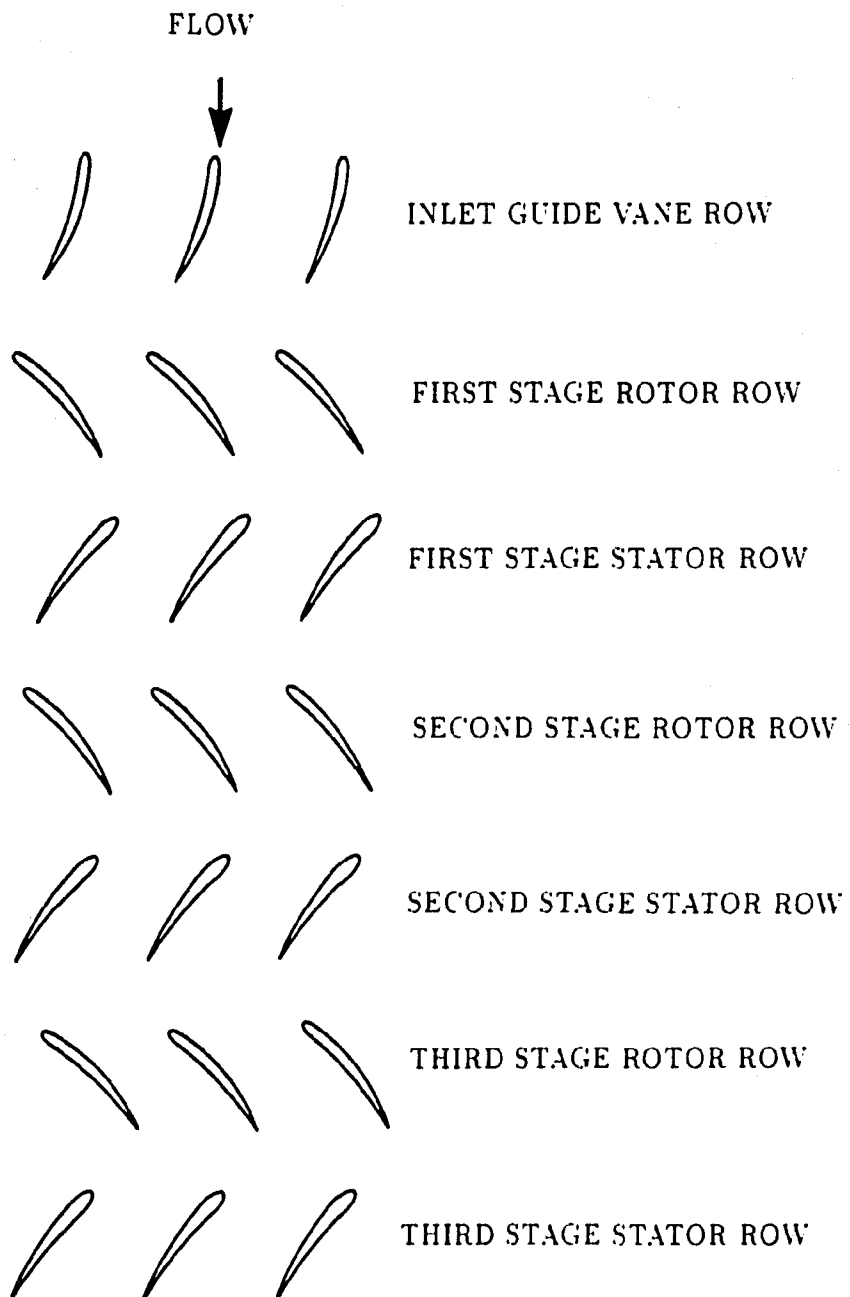


Figure 3.7: Blade-to-blade view of three-stage, axial-flow compressor blade rows

Blade setting angle 13.9° @ $r = 7.40$ in.

Stator blade details:

Blade span (constant) 2.40 in. (6.10 cm)

Blade chord (constant), c 1.20 in. (3.05 cm.)

Blade section maximum thickness/
chord ratio, t_{max}/c 10 %

Blade setting angle 35.8° @ $r = 7.40$ in.

Rotor blade details:

Blade span (constant) 2.40 in. (6.10 cm)

Blade chord (constant), c 1.20 in. (3.05 cm.)

Blade section maximum thickness/
chord ratio, t_{max}/c 10 %

Blade setting angle -33.9° @ $r = 6.21$ in.

The compressor discharged into a downstream duct (see Figure 3.6) which included an air straightening section, a venturi flow rate meter, a diffuser section, and an adjustable outlet-throttle plate. The compressor was driven by an 11 kW thyristor controlled variable speed (300 to 3000 rpm) D.C. motor mounted on air bearings. Shaft speed was measured with a frequency counter and a magnetic pickup off a 60-toothed gear on the rotor shaft. The motor speed was controlled by a multiturn helical potentiometer balanced against a feedback voltage from a dc tachogenerator which rotated with the motor shaft. It was possible to maintain a constant rotor speed to within ± 1 rpm. Further details about the three-stage, low-speed, axial-flow compressor may be found in reference [11].

3.3.1 Three-stage compressor performance tests

The three-stage, low-speed, axial-flow compressor performance tests were performed to validate and extend results observed with the two-stage axial-flow fan. In addition to determining the overall unstalled performance characteristic of the compressor, the stall hysteresis loop was also measured. The majority of tests performed on the three-stage axial-flow compressor involved varying the inlet guide vane (IGV) row setting angles only. The different blade setting angle patterns were achieved by setting individual IGV row vane setting angles according to Equations (3.1), (3.2), or (3.3). Another compressor test involved setting the inlet guide vanes and the first and second stage stator blades with identical circumferentially varying setting angle patterns after Equation (3.1) and lining up the patterns axially. One final set of tests involved setting all the inlet guide vanes either 6° more or 6° less than the baseline setting angle.

Overall compressor performance data were measured and non-dimensionalized to obtain values of total-head rise coefficient and flow coefficient calculated with Equations (3.8) and (3.9), respectively. Compressor flowrate was measured with a calibrated venturi flow meter located in the exit ductwork while compressor pressure rise was measured with a static wall pressure tap located at the compressor discharge.

$$\Psi_{comp} = \frac{\frac{P_t}{\rho} + V_z^2/2}{U_{tip}^2} \quad (3.8)$$

$$\Phi_{comp} = \frac{Q_v}{AU_{tip}} \quad (3.9)$$

Data for two different rotor speeds (1400 and 2000 rpm) were obtained in order to examine the effect of different rotational speeds on compressor stall performance

and hysteresis.

The stall point for the three-stage compressor was detected by listening for an unmistakable and distinct audible change in sound produced by the stalling compressor. This audible detection of stall was accompanied by a sudden drop in flowrate and head rise. Considerable care was taken in measuring the stall point. Experiments near the stall point involved slowly moving the throttle to a more closed position to reduce the overall flowrate while keeping the rotational speed constant. Fractional adjustments in the throttle position made possible an approach to the stall point in very small increments. Measurements were taken with each change in throttle position. The measurements of overall performance taken just before the audible detection of stall occurred were considered to be for the stall point operating condition. During any test, the stall point was approached and detected a minimum of 5 or 6 times. These tests were repeated on subsequent days to verify the repeatability of the results. Because stall point data were consistent throughout a data run and did not vary significantly from run to run or from day to day, it was felt that the error band for these measurements was within the symbol used.

For the three-stage compressor, the stall recovery point was detected by opening the throttle and thus increasing the flowrate. Again, fractional adjustments of the throttle to more open positions were used to approach the stall recovery point in small increments. The measurements taken just before the compressor recovered from stall were considered to be for the stall recovery point operating condition.

3.3.2 Three-stage compressor results

The three-stage axial-flow compressor was tested with a variety of circumferential variations of stationary row blade setting angles and the results are presented in this section. One set of tests involving circumferential variations of stationary blades in all stages was conducted. A final set of performance tests involved setting all the inlet guide vanes either 6° more or 6° less than the baseline setting angle. Stationary row blade setting angles were varied according to Equations (3.1), (3.2) and (3.3), which represent the sinusoidal, rectified sine wave, and asymmetric blade setting angle variations, respectively. The selection of appropriate setting angle patterns was guided by results from tests performed with the two-stage axial-flow fan as well as by observations made as tests involving the different modifications to the three-stage compressor were completed. Stall hysteresis loops were ascertained and compared to baseline data. The four important stall hysteresis loop operating points correspond to the operating points of the compressor just before stall, just after stall, just before coming out of stall, and just after coming out of stall.

The first set of results discussed corresponds to tests performed with the setting angles of inlet guide vane row blades varying circumferentially in a pattern established by Equation (3.1). For these tests, the amplitude of setting angle variation, $\Delta\phi$, remained essentially constant and the reduced frequency at stall, K_{stall} , was systematically altered by changing the number of setting angle variation cycles per rotor revolution, n . Two different rotor speeds, 1400 and 2000 rpm, were used.

The number of setting angle variation cycles per rotor revolution, n , took on values of 1 cycle/rev, 2 cycles/rev, 3 cycles/rev, and 4 cycles/rev, which resulted in values of reduced frequency at stall, K_{stall} , of 0.09, 0.19, 0.28, and 0.37, respectively.

Of these four schedules, the best results were seen with the 2 cycles/rev pattern, $K_{stall} = 0.19$. In Figure 3.8 is shown a comparison between baseline and modified compressor performance data for the 2 cycles/rev pattern. For $K_{stall} = 0.09$, the stall performance was worse than for the baseline configuration. For $K_{stall} = 0.28$, only a slight improvement, not as much as for $K_{stall} = 0.19$, was observed. For $K_{stall} = 0.37$, less improvement than for $K_{stall} = 0.28$ was noted. Results of tests performed at a higher rotational speed (2000 rpm) show nearly identical results as for the lower rotational speed (1400 rpm). Again, the stall point and recovery improvements were most noticeable in the 2 cycles/rev scheduling of inlet guide vane row blade setting angles.

The next set of experiments performed with the three-stage, axial-flow compressor involved rectified sine wave variations of inlet guide vane setting angles established by Equation (3.2). The blade setting angle variations were periodic half-sine waves set in either a positive (larger than baseline setting angles) or negative (smaller than baseline angles) mode which resulted respectively in either an overall decreased or increased loading of the downstream rotor blades. Different frequencies of increased or decreased loading were obtained by selecting an appropriate number of periodic half-sine wave variations per rotor revolution. The amplitude of the periodic half-sine wave variations was held constant at 6° .

When the inlet guide vanes were set with positive half-sine wave variations, a significant unloading of the compressor from baseline resulted for two different half-sine wave frequencies, namely, 2 cycles per rotor revolution and 4 cycles per rotor revolution. The stall hysteresis loop involved an unusual "kink" in recovery from stall as shown in Figure 3.9. When the inlet guide vanes were set with negative half-

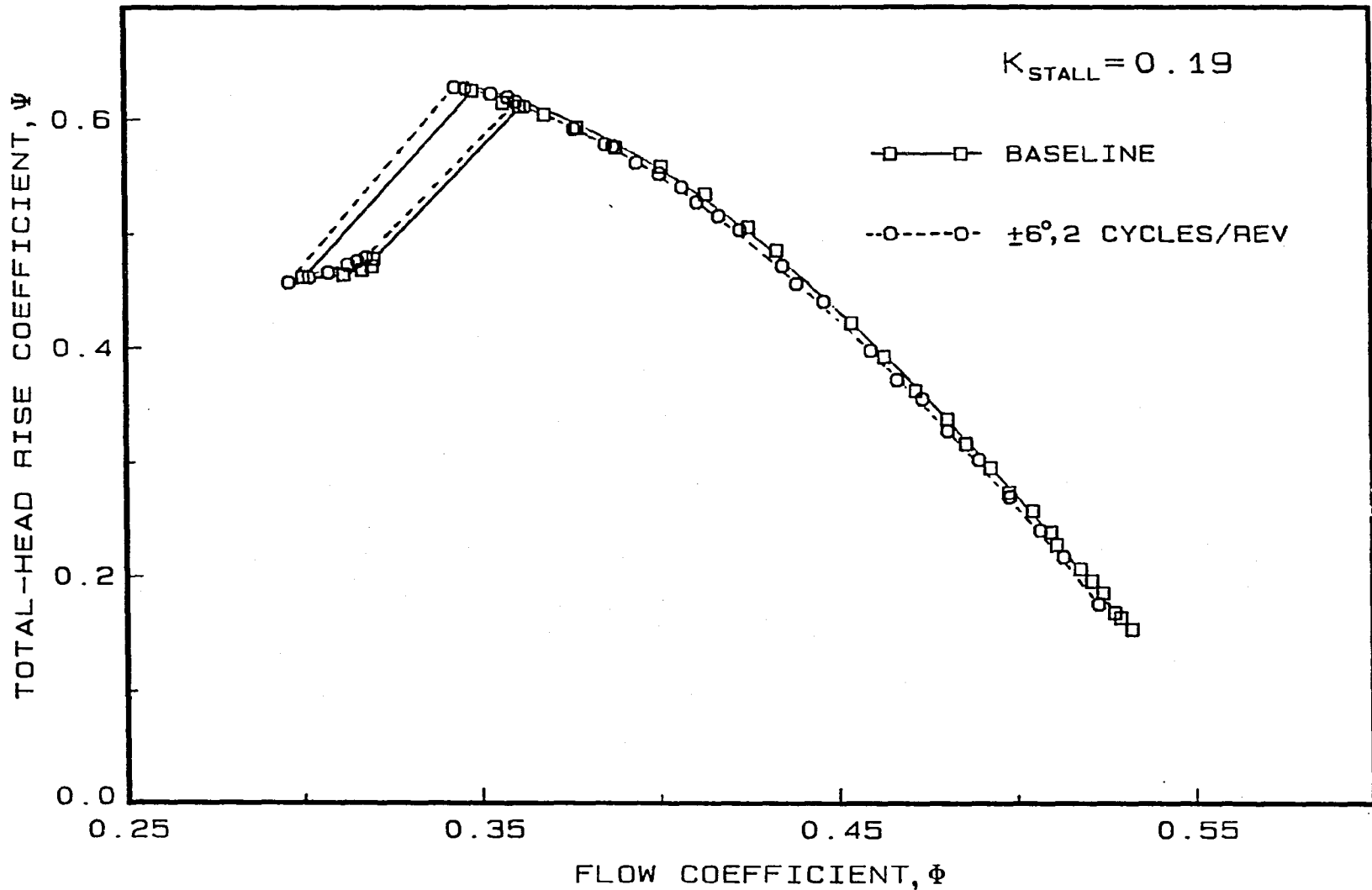


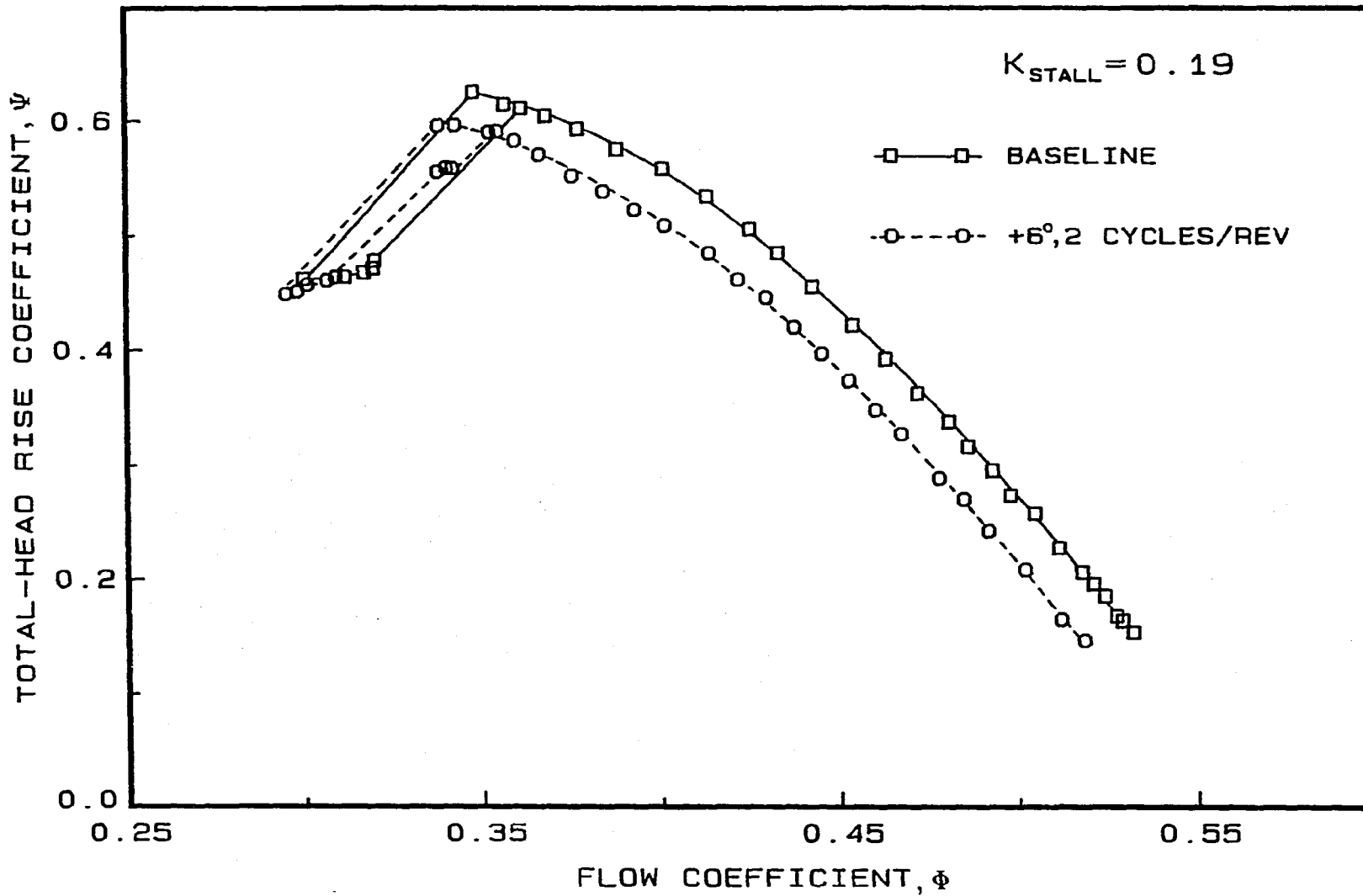
Figure 3.8: Three-stage axial-flow compressor results, inlet guide vane angle variation, $\Delta\phi = 6^\circ$, $n = 2$ cycles/rev, rotor speed = 1400 rpm.

sine wave variations, slightly more head rise but no significant change in stall point from baseline performance were noted. Also, the negative half-sine wave variations resulted in more hysteresis compared to baseline, see Figure 3.10.

A third set of tests performed with the three-stage axial-flow compressor involved the inlet guide vanes set in asymmetric blade setting angle variation patterns according to Equation (3.3). The purpose of these variations was to achieve a higher overall loading of the downstream rotor blades and some delay of stall onset.

Using asymmetric variations, two different tests were performed in which the number of setting angle variation cycles per rotor revolution, n , remained constant at 2, and the amplitudes of setting angle variation, $\Delta\phi_1$ and $\Delta\phi_2$, were altered. In Figure 3.11 are shown results of a comparison between baseline and modified compressor performance for which $\Delta\phi_1 = 16^\circ$ smaller than baseline (rotor loading) and $\Delta\phi_2 = 8^\circ$ larger than baseline (rotor unloading). These data suggest that this asymmetric variation resulted in an improvement in the stall point and also a higher head rise compared to baseline. Results from the second asymmetric variation in inlet guide vane setting angle with $n = 2$, $\Delta\phi_1 = 20^\circ$ smaller than baseline, and $\Delta\phi_2 = 10^\circ$ larger than baseline indicated a higher head rise but degradation rather than improvement in the stall point. For both asymmetric variations of IGV blade setting angle, any improvement in stall recovery was uncertain.

Additional performance tests were conducted with the inlet guide vanes, and the first and second stage stator blades set in sinusoidal setting angle variation patterns according to Equation (3.1). For these tests, $n = 3$ ($K_{stall} = 0.28$) and $\Delta\phi = 6^\circ$. This modified compressor (see Figure 3.12) produced less head rise and stalled earlier than the baseline compressor. In contrast, the compressor build involving only inlet guide



67

Figure 3.9: Three-stage axial-flow compressor results, inlet guide vane angle variation, $\Delta\phi = +6^\circ$, $n = 2$ cycles/rev, rotor speed = 1400 rpm.

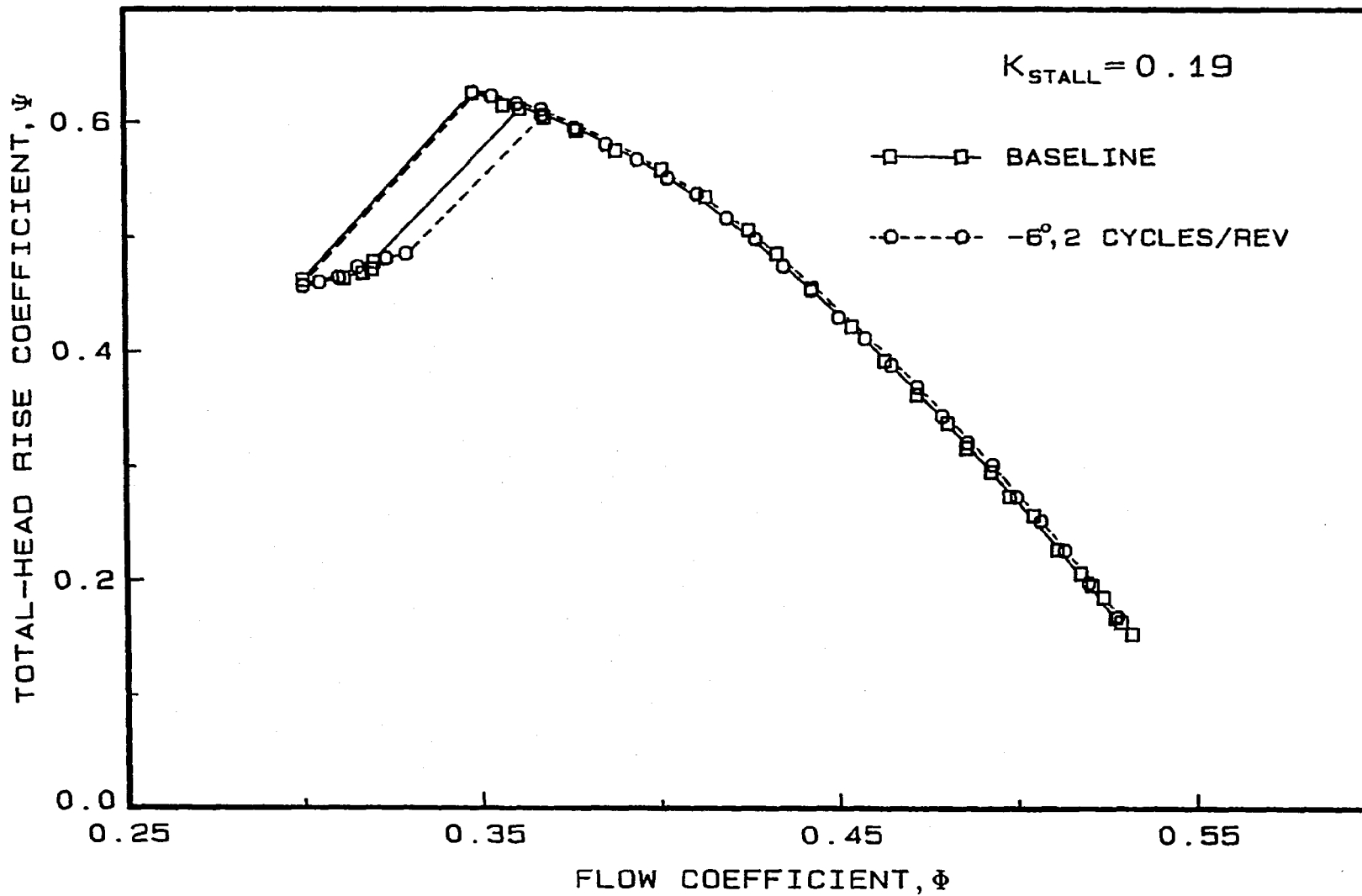


Figure 3.10: Three-stage axial-flow compressor results, inlet guide vane angle variation, $\Delta\phi = -6^\circ$, $n = 2$ cycles/rev, rotor speed = 1400 rpm.

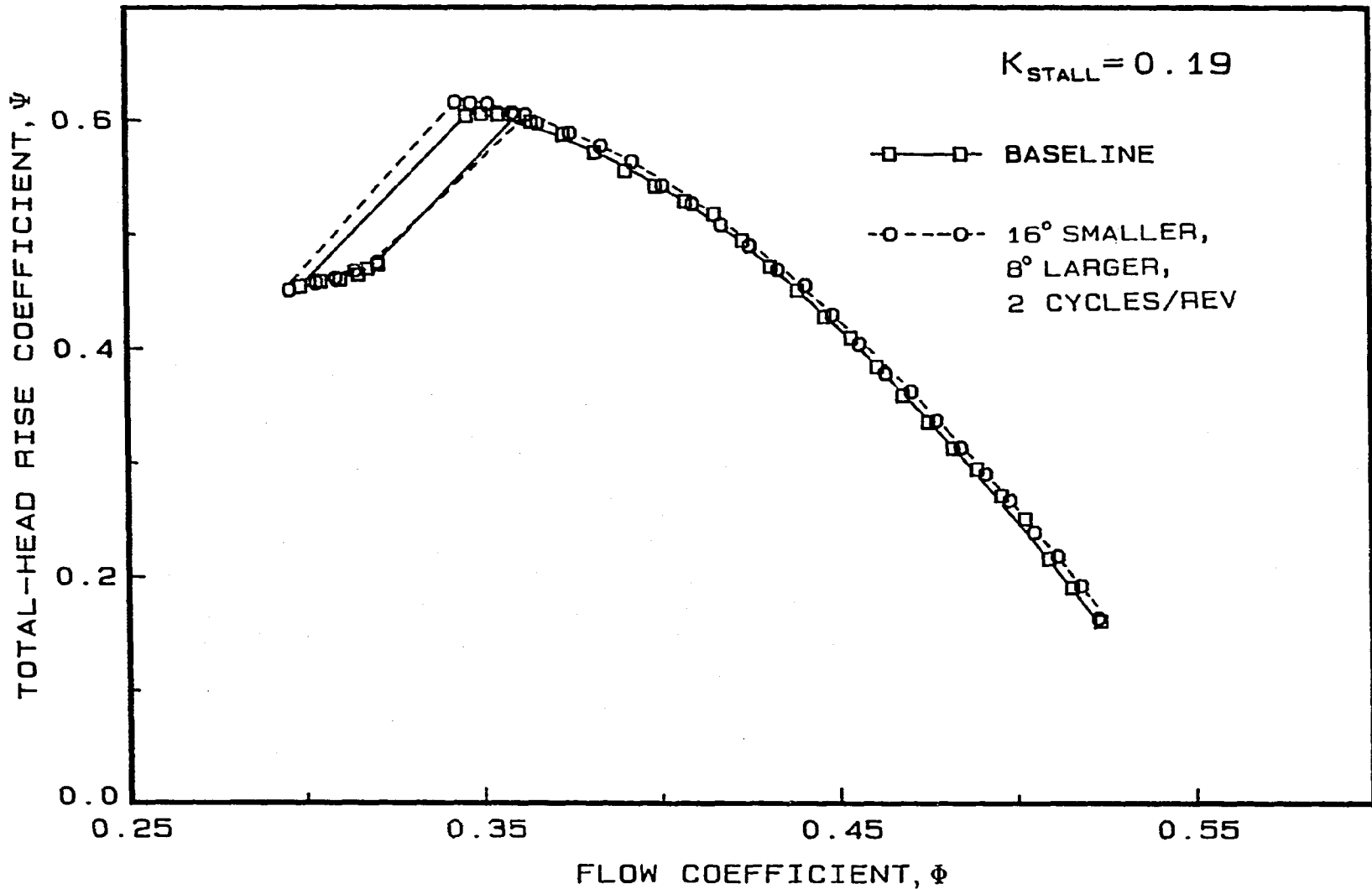


Figure 3.11: Three-stage axial-flow compressor results, inlet guide vane angle modification. $\Delta\phi_1 = -16^\circ$, $\Delta\phi_2 = -8^\circ$, $n = 2$ cycles/rev, rotor speed = 1400 rpm.

vanes set in a sinusoidal pattern with $n = 3$ and $\Delta\phi = 6^\circ$ suffered less head rise loss in comparison with this compressor and the baseline compressor. Also, periodically setting the inlet guide vanes only resulted in a slight delay in stall onset compared to baseline.

The final set of performance tests on the three-stage compressor involved setting all the inlet guide vanes either 6° more or 6° less than the baseline setting angle. A 6° change from the baseline setting angle was chosen because much of the previous data involved variations that used an amplitude of setting angle variation, $\Delta\phi$, of 6° . In particular, all the sinusoidal variations (with the exception of one, $\Delta\phi$, of 8°) in inlet guide vane setting angle used a $\Delta\phi$ of 6° . In addition, all rectified variations (loaded and unloaded) in blade setting angle used an amplitude of setting angle variation equal to 6° . Some interesting observations were made from these performance tests.

The two modifications to the baseline compressor involved setting all the inlet guide vanes either 6° more than the baseline blade setting angle or 6° less than the baseline blade setting angle. The overall result of these two inlet guide vane modifications was an unloading and loading the compressor, respectively, compared to baseline performance. In Figures 3.13 and 3.14 are shown the overall performance data where the baseline configuration of the compressor is compared to the modified compressor configurations in which all inlet guide vanes were set 6° more than or 6° less than the baseline blade setting angle, respectively.

Figure 3.13 suggests that when the inlet guide vanes are set 6° more than the baseline blade setting angle, a significant unloading of the compressor occurs at all flowrates. The drop in total-head rise coefficient is such that no conclusion can be drawn as to the stall margin improvement of this modification. Also noted is the

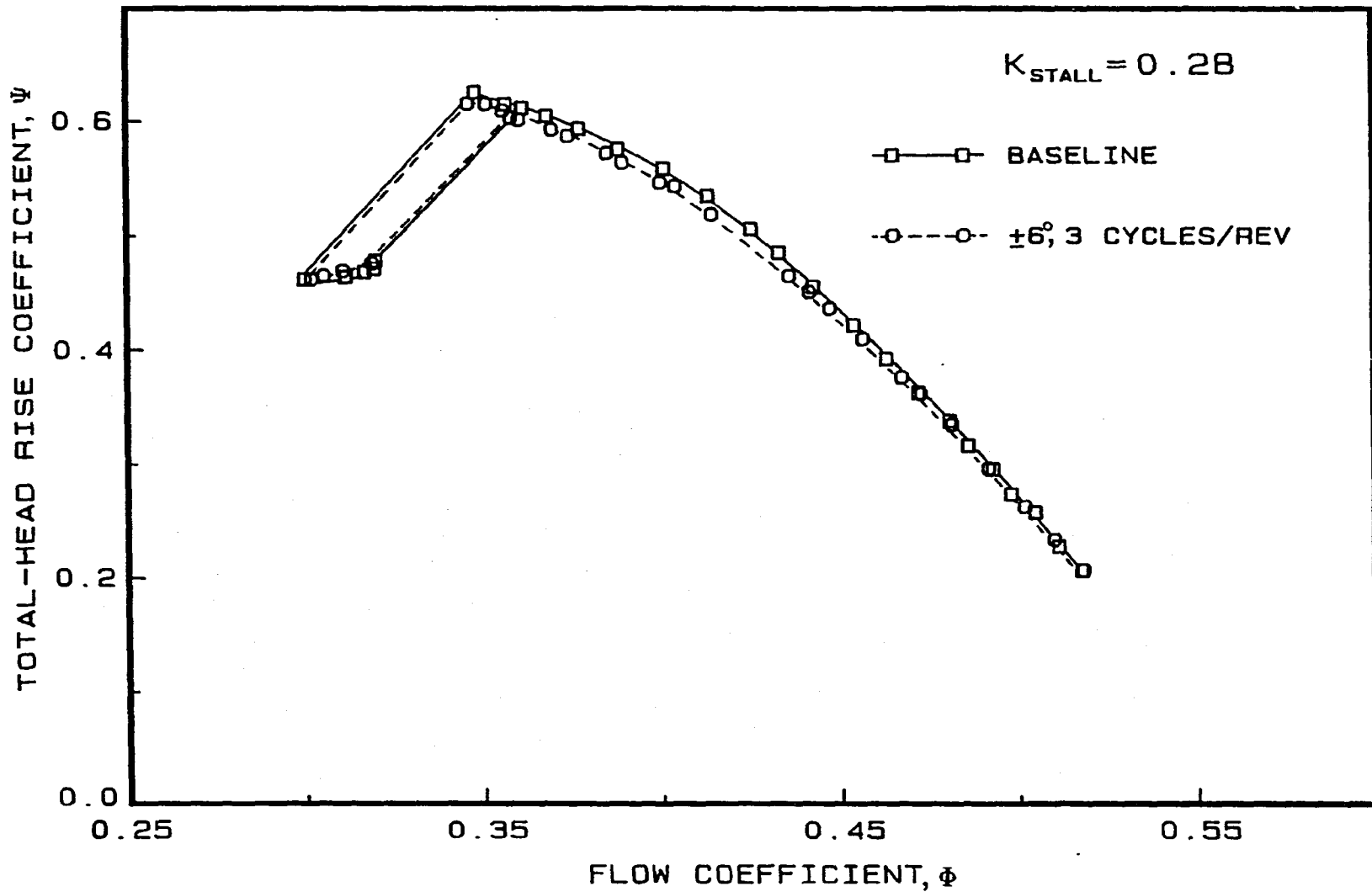


Figure 3.12: Three-stage axial-flow compressor results, inlet guide vane, first and second stage stationary row angle variation, $\Delta\phi = 6^\circ$, $n = 2$ cycles/rev, rotor speed = 1400 rpm.

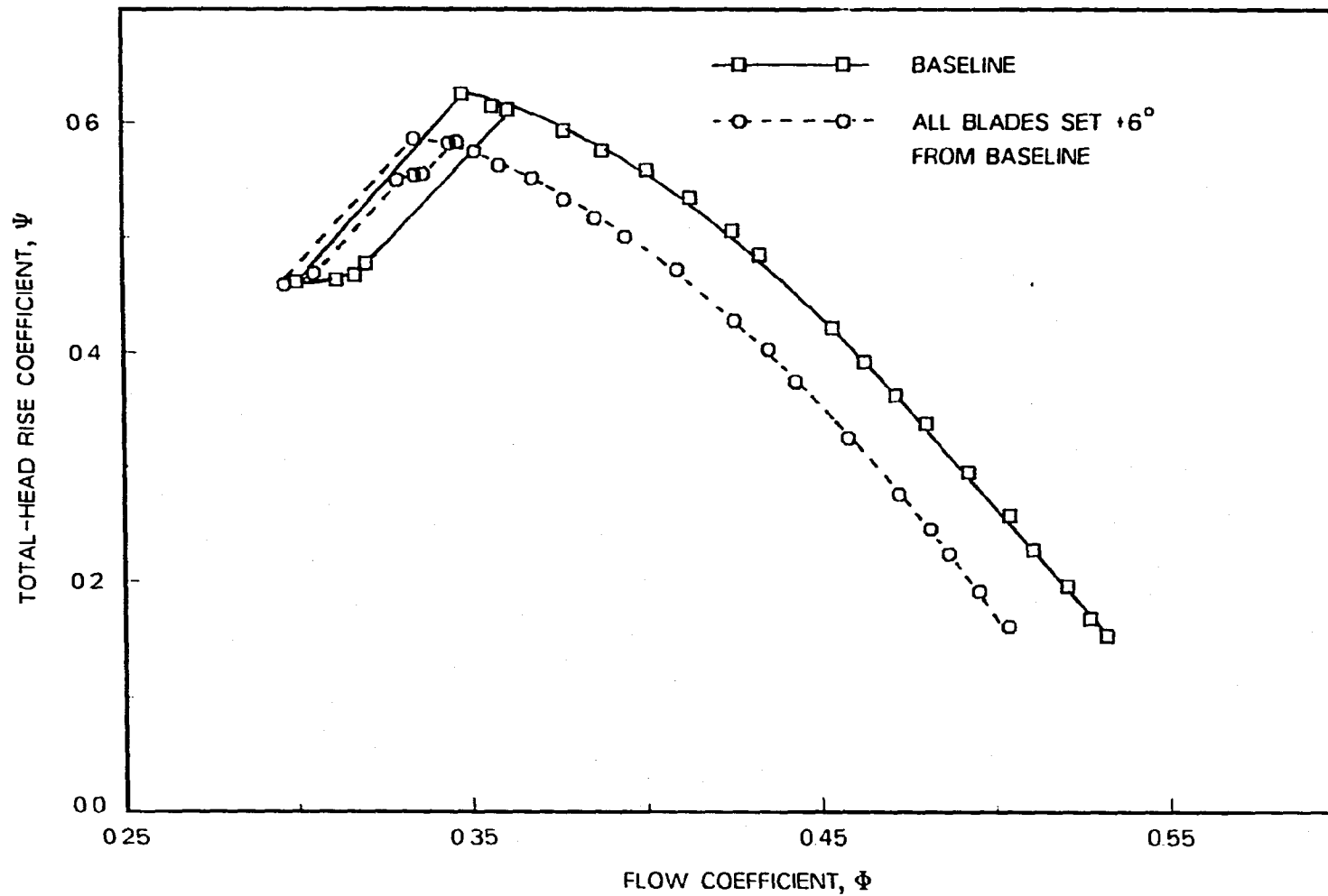


Figure 3.13: Three-stage axial-flow compressor results, all inlet guide vanes set 6° more than the baseline setting angle, rotor speed = 1400 rpm.

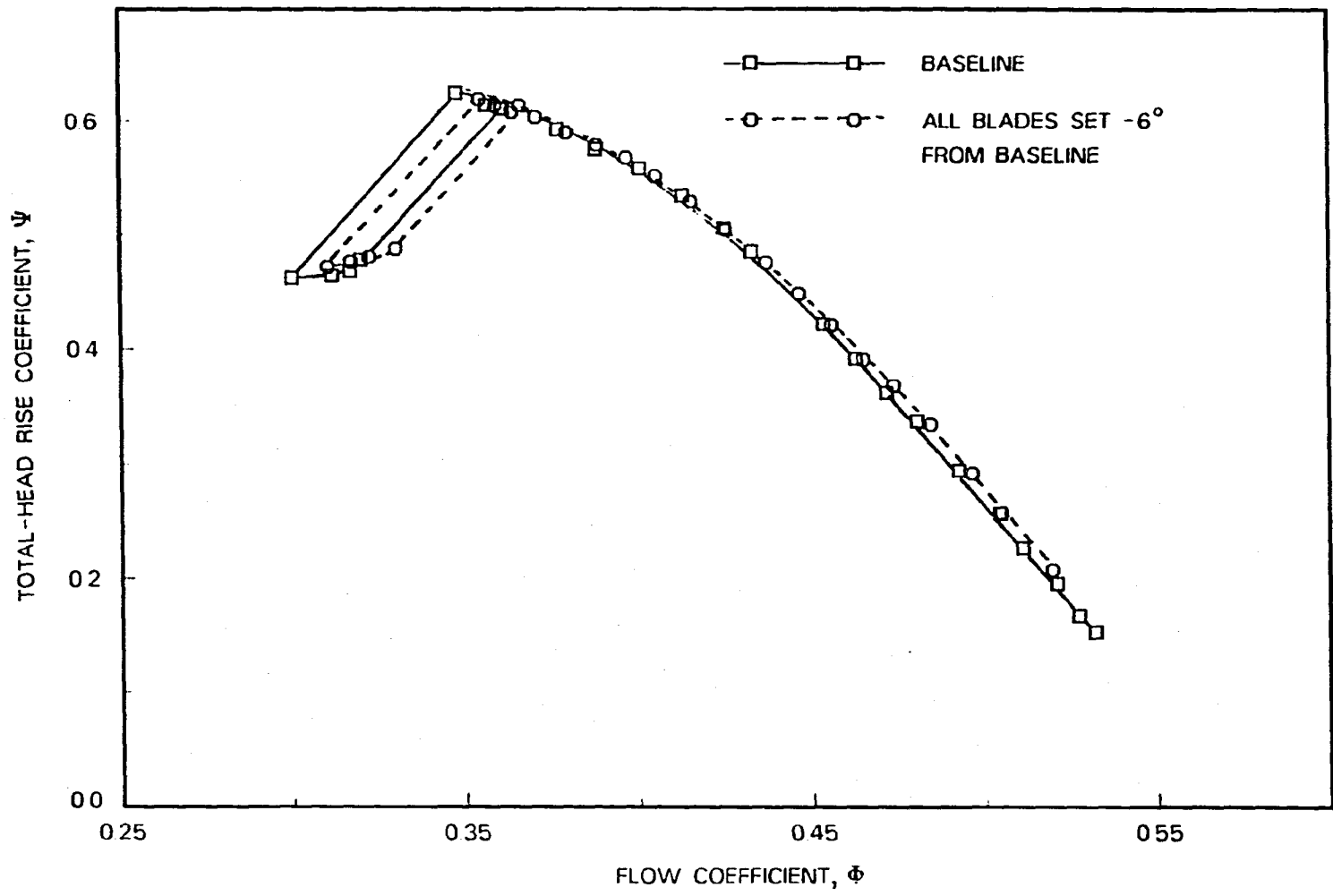


Figure 3.14: Three-stage axial-flow compressor results, all inlet guide vanes set 6° less than the baseline setting angle, rotor speed = 1400 rpm.

strange stall hysteresis behavior. The modified compressor performance suggests that two stall recovery points exist for this configuration. When unthrottled, the compressor recovers quickly but not entirely. Further unthrottling is necessary to completely recover the compressor from the stalled condition. This unusual behavior suggests that one part of the modified compressor may be operating in a stalled condition while another part operates unstalled. The similarity of Figure 3.9 and Figure 3.13 is unmistakable. Figure 3.9 involved a rectified variation of inlet guide vane setting angle with a $+6^\circ$ amplitude of setting angle in a 2/rev manner. The unloading of the compressor from baseline behavior is evident but is slightly less than the compressor configuration which reset all blades 6° more than baseline. Again, the unusual hysteresis behavior is noted for this configuration as well.

Figure 3.14 reflects those results in which all inlet guide vanes were set 6° less than the baseline blade setting angle. This figure suggests that a slight loading of the compressor is accomplished at higher flowrates, but diminishes at lower flowrates. The stall point for this modification occurs at a higher flowrate indicating a significant stall margin degradation from baseline. The stall hysteresis behavior no longer exhibits the unusual two part recovery, but is simply shifted to the higher flowrates. If these performance data are compared with those of Figure 3.10, which involved a rectified variation of inlet guide vane setting angle with a -6° amplitude of setting angle in a 2/rev manner, some interesting observations can be made. Figure 3.10 indicates that no penalty in stall margin occurs with the rectified variation, whereas Figure 3.14 indicates that a significant stall margin penalty occurs when all blades are set 6° less than baseline. This observation suggests that there is a benefit in the unsteady loading of the compressor compared to what happens with a static loading

of the compressor.

3.4 Detailed Flow Measurements for Three-Stage Compressor

For the purpose of identifying some of the detailed flow characteristics caused by the blade setting angle variations, the acquisition of detailed flow measurements (velocity angle and magnitude) behind the inlet guide vanes was accomplished with the low-speed, three-stage compressor. These measurements, however, were not possible on the Pratt & Whitney intermediate-speed, three-stage compressor. The low-speed compressor measurements confirmed that the absolute flow angle changed as a result of the blade setting angle variation in the inlet guide vane row. In this case, detailed measurements were performed for the most productive inlet guide vane setting angle patterns (in terms of stall margin improvement) and were acquired over a portion of the flow path cross-section area at various flow rates.

The detailed measurements were taken with a United Sensor total-pressure cobra probe. The cobra probe was positioned in an L. C. Smith probe actuator and was mounted on the compressor outer casing. The cobra probe head was located downstream of the inlet guide vane exit in the measurement plane shown in Figure 3.15. Absolute flow angle measurements were accomplished by positioning the angle of the cobra probe such that the two side pressures were identical as indicated by a U-tube manometer. These absolute flow angle measurements were limited to freestream flow regions because erroneous results occur when measuring in total-pressure (velocity) gradient regions. Different circumferential measurements were accomplished by movement of the inlet guide vanes in a independent ring assembly relative to the cobra probe position. Ten different circumferential measurement locations were

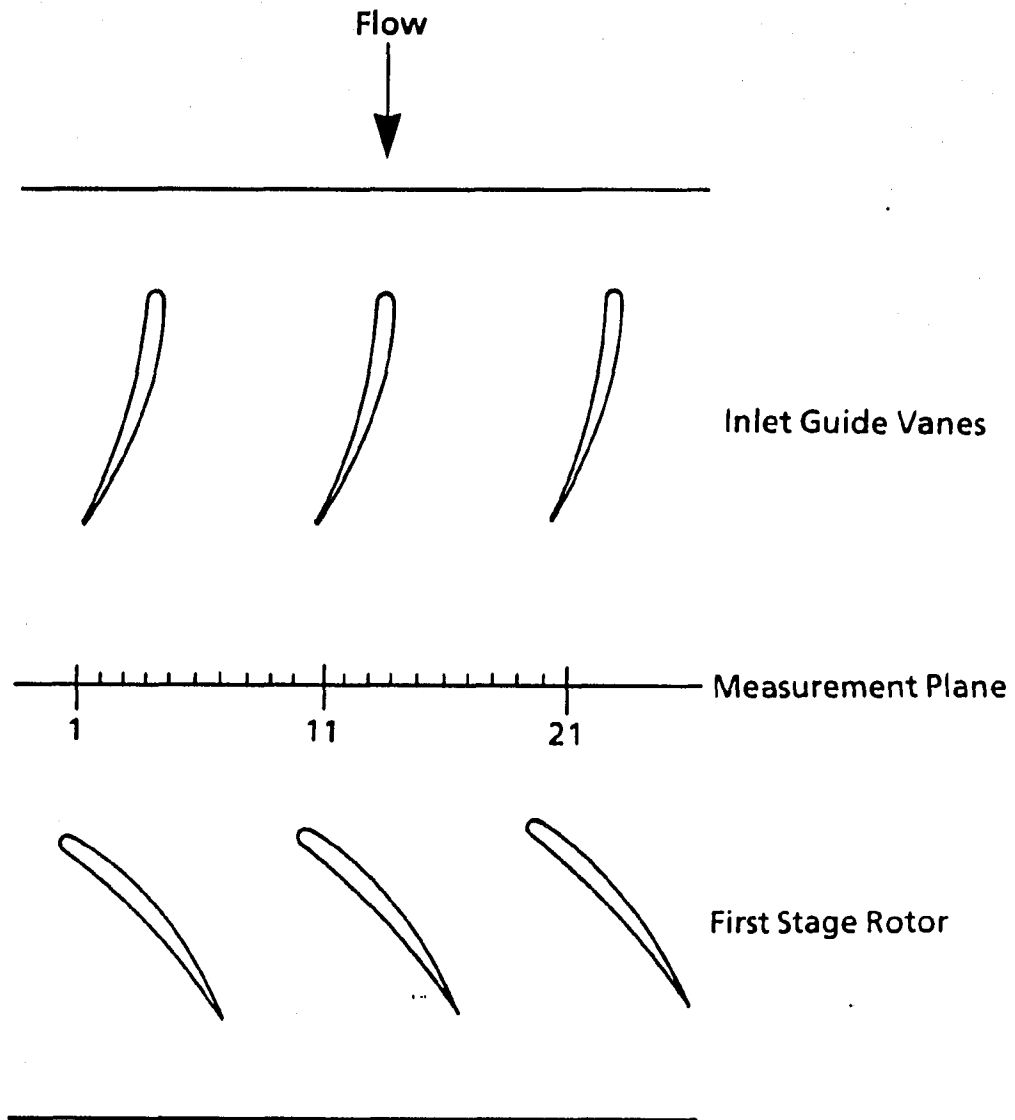


Figure 3.15: Measurement plane for detailed measurements at the exit of the inlet guide vane row

used for each blade passage (see Figure 3.15) and two complete blade passages were surveyed per test. These circumferential detailed measurements were performed at five different immersion depths from the outer casing, namely, 10, 30, 50, 70 and 90 percents of span. Detailed measurements were examined at a flowrate condition near stall where Φ equaled 0.353 and at the compressor design point where Φ equaled 0.420.

Detailed measurements were performed on the baseline configuration of the three-stage compressor as well as two candidate modified compressor configurations (with circumferentially varying stationary blade setting angle patterns). The two modified compressor configurations were those that resulted in the most noticeable increase in stall margin improvement compared to baseline performance. The first modified compressor was one that employed a sinusoidal variation of inlet guide vane setting angle with the amplitude of setting angle variation, $\Delta\phi = 6^\circ$, and the number of setting angle variations per rotor revolution, $n = 2$ ($K = 0.19$). The second modified compressor modification used an asymmetric variation of inlet guide vane setting angle with $\Delta\phi_1 = 16^\circ$ and $\Delta\phi_2 = 8^\circ$ and $n = 2$ ($K = 0.19$). For these two candidate setting angle variations, detailed measurements (velocity angle and magnitude) were acquired behind the inlet guide vanes set the maximum and minimum setting angle amplitudes from the baseline setting angle. It was determined that these surveyed regions would be sufficient to adequately describe the exit flow around the entire circumference of the compressor. In Figure 3.16 is shown the regions in which detailed measurements were acquired for the sinusoidal variation ($\Delta\phi = 6^\circ$, $n = 2/\text{rev}$) and the asymmetric variation ($\Delta\phi_1 = 16^\circ$, $\Delta\phi_2 = 8^\circ$, $n = 2/\text{rev}$). For the asymmetric variation, the maximum setting angle variation region ($\Delta\phi = +8^\circ$) was not surveyed

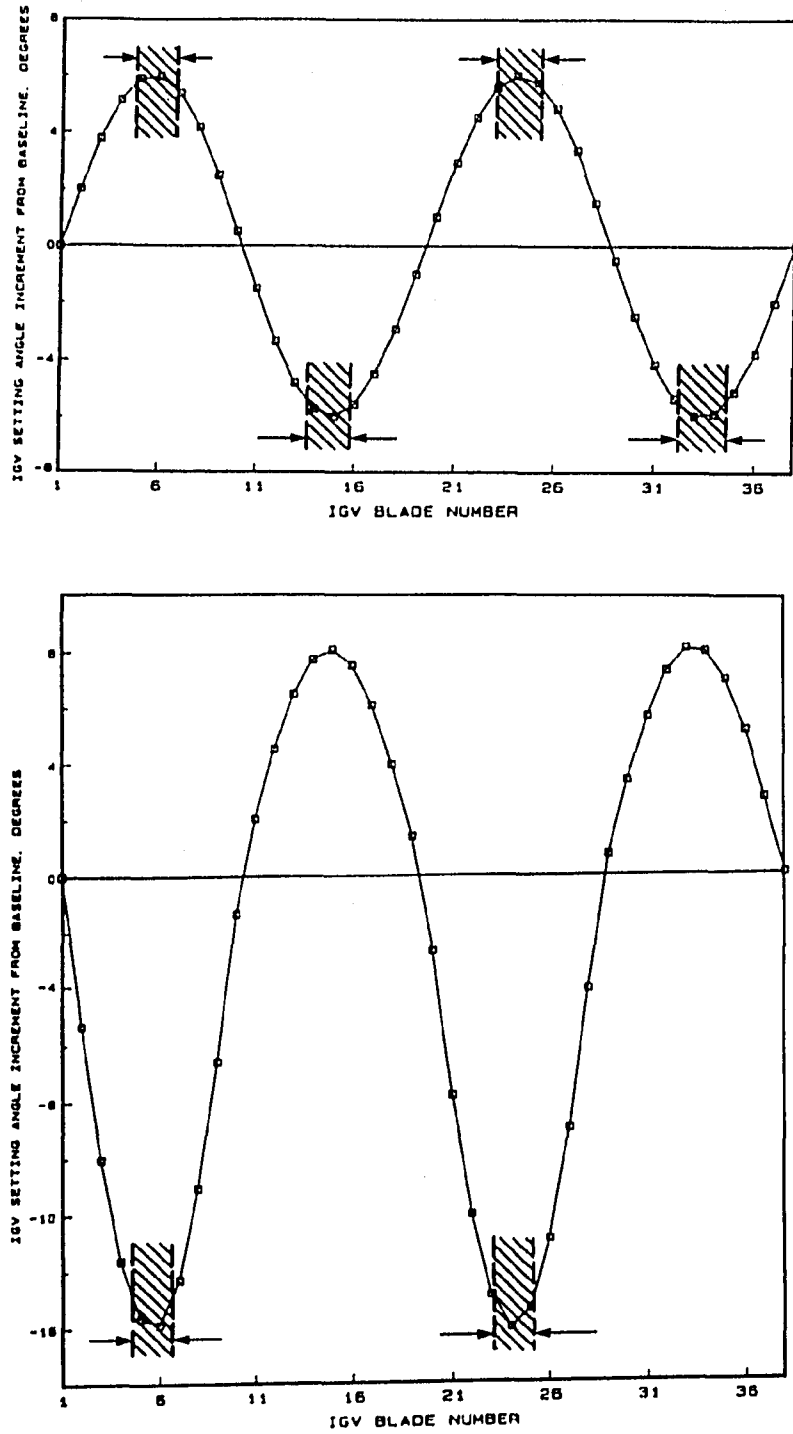


Figure 3.16: Setting angle variation regions for detailed measurements data

due to the proximity of the results with the sinusoidal variation where $\Delta\phi = +6^\circ$ was surveyed.

In Figure 3.17 is shown a typical total-pressure measurement survey for the baseline compressor configuration at the design point and near stall operating point covering two complete blade passages. The dashed lines separate the freestream flow regions and wake regions where absolute flow angle measurements were possible and not possible, respectively. The total-pressure (velocity) gradient flow regions are due to wakes being shed from the inlet guide vanes upstream. The cobra probe side pressure ports could not be equalized in these regions and therefore, absolute flow angle measurements were not possible.

In Tables 3.2 and 3.3 are shown the absolute flow angle measurements for the baseline compressor configuration at the near stall point ($\Phi = 0.353$) and the design operating point ($\Phi = 0.420$) for immersion depths of 10, 30, 50, 70 and 90 percent of span. The data presented are the average absolute flow angles for the two blade passages surveyed. The data of Tables 3.2 and 3.3 suggest that the absolute flow angle ranges from about 16° to 30° for both near stall point data and design operating point data and not only varies from hub to tip but circumferentially as well. The tabular data also suggest that the inlet guide vane performance (absolute flow angle values) at the design point is nearly identical to the performance near stall. This notion is consistent with the idea that inlet guide vane behavior, especially turning angle, is independent of flowrate variations at low inlet Mach numbers (less than 0.3).

In Tables 3.4 through 3.7 some of the actual angle differences from the baseline flow angles measured are presented for two blade setting angle variations. Additional detailed flow measurement data are tabulated in Appendix A. Those regions surveyed

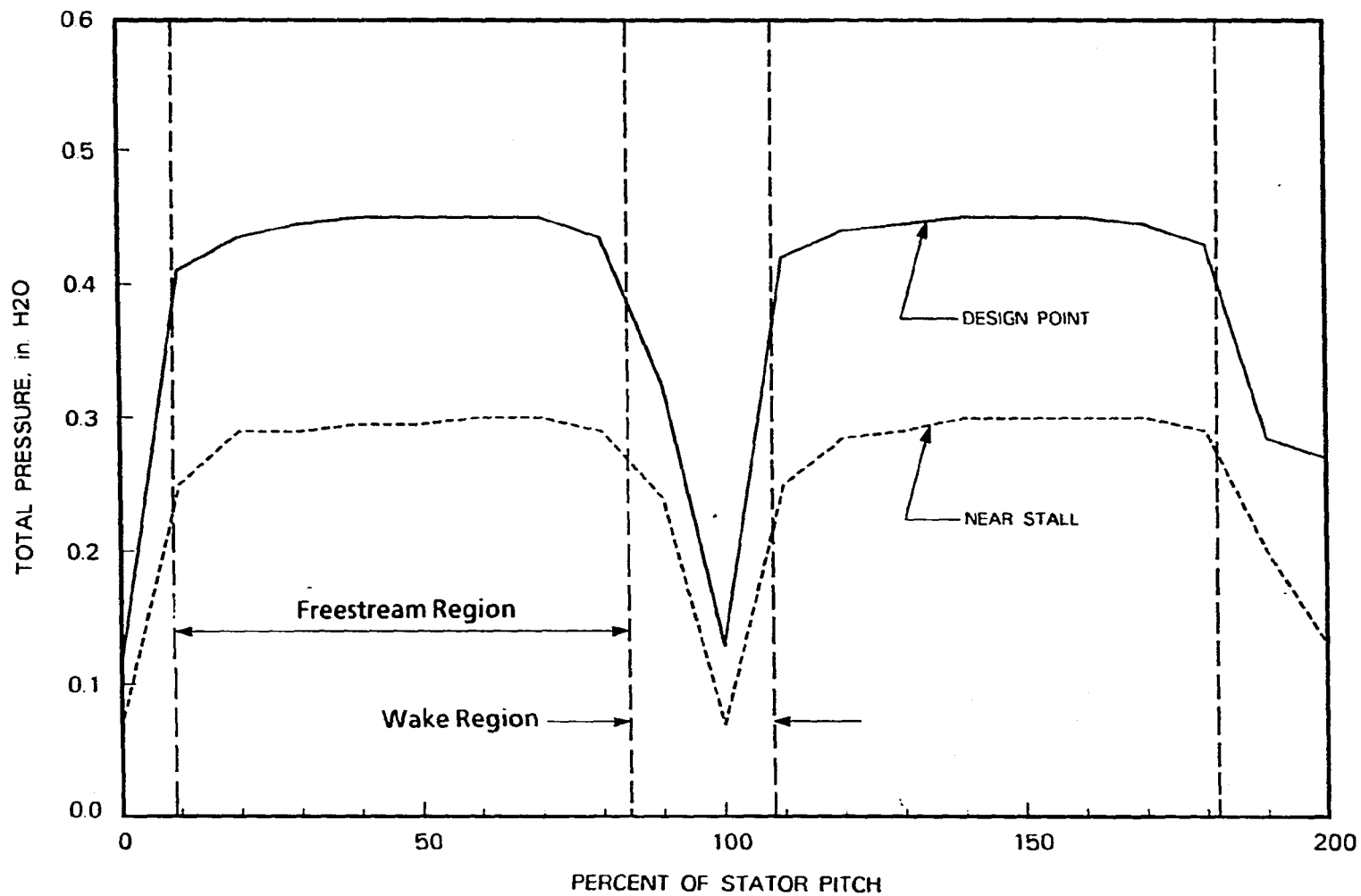


Figure 3.17: Total-pressure variation across two blade passages, inlet guide vane exit, baseline at 50% immersion, $\Phi = 0.353$ and $\Phi = 0.420$

Table 3.2: Absolute flow angle (°), baseline, $\Phi = 0.353$

Circumferential Position	% Imm.				
	10	30	50	70	90
1	-	-	-	-	-
2	-	-	20.6	19.1	16.0
3	22.1	22.5	20.8	19.8	16.5
4	25.4	23.7	21.8	20.1	17.4
5	26.3	24.6	22.8	20.7	18.1
6	26.7	25.1	23.7	21.6	18.7
7	27.7	25.8	25.3	22.7	19.6
8	29.5	27.1	26.0	23.8	20.5
9	-	28.5	-	27.0	-
10	-	-	-	-	-
Ave.	26.3	25.3	23.0	21.8	18.1

Table 3.3: Absolute flow angle (°), baseline, $\Phi = 0.420$

Circumferential Position	% Imm.				
	10	30	50	70	90
1	-	-	-	-	-
2	-	19.6	19.5	17.8	-
3	24.0	22.1	20.8	18.6	17.3
4	25.4	23.2	21.2	19.4	17.9
5	26.6	23.4	22.2	20.3	17.9
6	26.6	24.4	22.5	20.5	18.1
7	27.8	25.4	24.6	22.1	19.2
8	28.8	27.1	27.3	23.2	20.7
9	-	-	-	24.8	22.2
10	-	-	-	-	-
Ave.	26.5	23.6	22.6	20.8	19.0

are shown in Figure 3.16 and were taken at flow coefficient values of 0.353 and 0.420. The data are repetitive in that the angles for flow near stall and at the design point are nearly identical as expected. The data, however, indicate some important results. In tables 3.4 and 3.5 are tabulated the flow angle differences from the baseline flow angle from a survey taken behind three blades set to the most positive increments ($+6^\circ$) of a sinusoidal blade setting angle variation. These data suggest that there is little difference existing between the measurements taken at two different flowrates. These tables also show the actual turning accomplished by the $+6^\circ$ blade setting angle variation varies from approximately $+4^\circ$ to $+8^\circ$ and has an average of about $+5.5^\circ$. Therefore, the actual turning behind three inlet guide vanes set approximately $+6^\circ$ from the baseline setting angle is about $+5.5^\circ$.

In Table 3.6 is tabulated the detailed flow data at a flow condition near stall from a surveyed region where three blades were set approximately -6° from the baseline setting angle. This table again illustrates that the desired turning of the flow behind the inlet guide vanes was being accomplished. The angles of the surveyed region vary from -2° to -7° and the actual turning angle averages are slightly below -6° with an average of -5.6° . This actual turning is very close to the anticipated flow angle change of -6° .

In Table 3.7 are tabulated angular data from a surveyed region where three blades were set approximately -16° from the baseline setting angle. These turning angle values suggest that slightly more turning was being accomplished than expected. The turning angle variation from the baseline value ranged from -11° to -21° and averaged about -16.8° . This actual turning is slightly more than expected but nevertheless close to the anticipated turning of -16° .

Table 3.4: Absolute flow angle (°) variation from baseline, $+6^\circ$ 2/rev, $\Phi = 0.353$

Circumferential Position	% Imm.				
	10	30	50	70	90
1	-	-	-	-	-
2	-	-	+5.7	+5.4	+5.2
3	+7.8	+6.2	+6.3	+5.1	+5.2
4	+6.7	+5.4	+6.3	+5.3	+4.9
5	+6.4	+5.3	+6.0	+5.2	+5.0
6	+6.5	+5.4	+5.9	+4.6	+4.6
7	+6.2	+5.2	+5.3	+4.4	+4.7
8	+5.2	+4.2	+6.1	+5.4	+4.4
9	-	-	-	-	-
10	-	-	-	-	-
Ave.	+6.5	+5.3	+5.9	+5.1	+4.9

Table 3.5: Absolute flow angle (°) variation from baseline, $+6^\circ$ 2/rev, $\Phi = 0.420$

Circumferential Position	% Imm.				
	10	30	50	70	90
1	-	-	-	-	-
2	-	-	-	+6.7	-
3	+4.8	+5.4	+5.5	+6.3	+4.3
4	+5.8	+6.0	+6.0	+6.0	+4.2
5	+5.4	+6.6	+5.9	+5.3	+4.7
6	+5.9	+6.1	+6.3	+5.8	+5.2
7	+5.5	+5.8	+4.6	+5.5	+4.7
8	+5.7	+4.6	+2.8	+5.6	+3.9
9	-	-	-	+5.4	-
10	-	-	-	-	-
Ave.	+5.5	+5.8	+5.2	+5.8	+4.5

Table 3.6: Absolute flow angle (°) variation from baseline, -6° 2/rev, $\Phi = 0.353$

Circumferential Position	% Imm.				
	10	30	50	70	90
1	-	-	-	-	-
2	-	-	-5.6	-6.3	-5.5
3	-2.3	-5.1	-4.8	-6.2	-6.0
4	-5.2	-5.7	-5.6	-5.9	-5.8
5	-5.4	-6.1	-5.9	-6.0	-5.8
6	-5.3	-5.9	-5.6	-6.2	-5.9
7	-5.4	-5.8	-6.2	-6.7	-5.6
8	-5.7	-6.2	-5.7	-6.3	-5.5
9	-	-	-	-	-
10	-	-	-	-	-
Ave.	-4.9	-5.8	-5.6	-6.2	-5.7

Table 3.7: Absolute flow angle (°) variation from baseline, -16° 2/rev, $\Phi = 0.353$

Circumferential Position	% Imm.				
	10	30	50	70	90
1	-	-	-	-	-
2	-	-	-	-21.0	-17.1
3	-16.4	-18.5	-17.8	-18.7	-15.4
4	-17.8	-18.2	-17.8	-17.0	-14.9
5	-18.5	-18.0	-17.6	-16.0	-14.1
6	-17.9	-17.4	-16.8	-16.0	-13.7
7	-18.0	-17.3	-17.3	-15.8	-12.6
8	-17.5	-17.1	-15.9	-15.7	-11.4
9	-	-	-	-	-
10	-	-	-	-	-
Ave.	-17.7	-17.8	-17.2	-17.2	-14.2

3.4.1 Velocity diagram calculations using detailed measurements

In Chapter 5 of this dissertation, estimates for the reduced frequency and rotor inlet flow angle variation are made using a simplified approach outlined in reference [12]. These estimates were made for midspan geometry only at the stall condition. The radial survey of detailed measurements discussed in the previous section can be used to produce a more precise calculation of the actual reduced frequency at stall, K_{stall} , and the maximum and minimum rotor inlet flow angle variations. The analysis involves using hub to tip detailed measurements for the baseline flow angle to solve for the baseline velocity triangles at the stall point and/or design point. These baseline velocity triangles are then compared to those in which detailed measurements were taken behind those few inlet guide vanes reset to the minimum and maximum setting angle amplitudes from baseline.

In order to construct blade velocity diagrams from detailed measurements, the radial static pressure distribution at the exit to the inlet guide vanes must be calculated. This is accomplished by solving the hydrodynamic equation of equilibrium for the flow exiting the inlet guide vanes. Assuming radial velocities are equal to zero, the hydrodynamic equation of equilibrium can be written,

$$\frac{1}{\rho} \frac{\partial P}{\partial r} = \frac{V_{\theta}^2}{r} \quad (3.10)$$

or

$$\frac{\partial P}{\partial r} = \frac{\rho V_{\theta}^2}{r} \quad (3.11)$$

From blade velocity triangle relations,

$$V_{\theta} = V \sin \beta \quad (3.12)$$

Substitution of Equation (3.12) into Equation (3.11) results in,

$$\frac{\partial P}{\partial r} = \frac{\rho V^2 \sin^2 \beta}{r} \quad (3.13)$$

And using Bernoulli's equation for incompressible flow,

$$\frac{P}{\rho} + \frac{V^2}{2} = \frac{P_t}{\rho} \quad (3.14)$$

or

$$V = \sqrt{\frac{2(P_t - P)}{\rho}} \quad (3.15)$$

Substituting this result into Equation (3.13) gives the final form of the hydrodynamic equation of equilibrium which is written as

$$\frac{\partial P}{\partial r} = \frac{2 \sin^2 \beta (P_t - P)}{r} \quad (3.16)$$

Equation (3.16) indicates that a knowledge of the total-pressure, P_t , and the absolute flow angle, β , at different radial locations, r , may be used to solve the static pressure distribution. The average values of the absolute flow angle and total-pressure circumferential survey at different radial locations given in the previous section and in Appendix A were used in the analysis. Equation (3.16) was solved on a computer using a curve-fitting algorithm along with an initial estimate for the static pressure distribution. Because detailed measurements were acquired at five different radii, namely 10, 30, 50, 70 and 90 percent immersion depths, a five point curve-fitting algorithm was used. The initial estimate for the static pressure distribution involved using the measured value of static wall pressure and a straight line variation of static pressure from hub to tip. The algorithm then adjusted the individual static pressure values at the five different radii in successive iterations until the left hand side of

Equation (3.16) equaled the right hand side for the different radial locations. With the static distribution solution, the blade velocity diagrams were constructed with the use of Equation (3.15) for the absolute velocity, V , Equation (3.12) and Equations (5.4) through (5.9) of Chapter 5.

The process of solving for the static pressure distribution and blade velocity triangles was repeated for an operating condition near stall and at the design operating point. In Table 3.8 are summarized the results of the baseline velocity diagram calculations. These data are the static pressure, P_{st} , absolute flow angle, β_1 , absolute flow velocity, V_1 , absolute tangential velocity, V_{θ_1} , blade velocity, U_1 , relative tangential velocity, w_{θ_1} , axial velocity, V_{x_1} , relative velocity, w_1 , relative flow angle, β'_1 and the reduced frequency at stall, K_{stall} , for each radial location. The value of K_{stall} is calculated from the following equation,

$$K = \frac{14.66}{w_1} \quad (3.17)$$

Equation (3.17) is derived by rearranging Equation (3.5), $V = w_1$, and substituting values for n , c and RPM , where

$$n = 2 \text{ cycles per rotor revolution}$$

$$c = 1.20 \text{ in.}$$

$$RPM = 1400 \text{ rpm}$$

Further calculation of the minimum and maximum rotor inlet flow angle variation from the baseline value may be made by using absolute flow angle measurements for circumferential blade setting angle variations. For this calculation, it is assumed that the axial velocity remains constant from hub to tip regardless of the imposed variation in inlet guide vane setting angle. Therefore, the axial velocities calculated

from the baseline detailed measurement data become the axial velocities for the modified velocity diagram calculations. By using the following equation,

$$V = \frac{V_{x1}}{\cos \beta} \quad (3.18)$$

and Equations (5.4) through (5.9) this is accomplished.

In Tables 3.9 through 3.11 are tabulated some of the velocity triangle calculations for those modified compressor detailed measurements whose regions are shown in Figure 3.16. Additional velocity triangle calculations for the design point conditions are tabulated in Appendix B. Of particular importance in these tables is the rotor inlet flow angle variation from baseline, $\Delta\beta'_1$. This quantity is a measure of rotor loading or unloading from hub to tip. A $\Delta\beta'_1$ value of $+1.0^\circ$ would indicate a increase in rotor relative flow angle of 1.0° when the rotor passes through the particular setting angle variation. Similarly, a $\Delta\beta'_1$ value of -1.0° would indicate a decrease in rotor relative flow angle of 1.0° .

A comparison is made between the detailed measurement calculations and the estimated values for the reduced frequency and rotor inlet flow angle variation for the three-stage compressor. Because estimated values of reduced frequency and extent of rotor inlet flow angle variation exist only for midspan geometry, these values are compared. Table 3.8 indicates that the midspan reduced frequency at stall from detailed measurements is 0.19. This value is identical to the estimated value for midspan reduced frequency at stall ($K_{stall} = 0.19$). Also, midspan values for the extent of rotor inlet flow angle variation calculated with detailed data are nearly identical to estimated values (Table 5.4). This comparison suggests that the original estimates for reduced frequency and extent of rotor inlet flow angle variation are accurate. This

conclusion is important in determining the blade setting angle variation for the Pratt & Whitney compressor.

Table 3.8: Detailed flow measurement data, baseline, $\Phi = 0.353$

% Imm.	P_{st} lb/in ²	β_1 ($^\circ$)	V_1 ft/s	V_{θ_1} ft/s	U_1 ft/s	w_{θ_1} ft/s	V_{x_1} ft/s	w_1 ft/s	β'_1 ($^\circ$)	K_{RF}
10	-0.0103	18.1	36.60	11.37	94.81	83.44	34.79	90.40	67.4	0.16
30	-0.0105	21.8	36.92	13.71	88.94	75.23	34.28	82.67	65.5	0.18
50	-0.0107	23.0	37.30	14.57	83.08	68.51	34.33	76.63	63.4	0.19
70	-0.0110	25.3	37.74	16.13	77.21	61.08	34.12	69.96	60.8	0.21
90	-0.0113	26.3	38.35	16.99	71.35	54.36	34.38	64.32	57.7	0.23

Table 3.9: Detailed flow measurement data, $+6^\circ$ 2/rev, $\Phi = 0.353$

% Imm.	β_1 ($^\circ$)	V_1 (ft/s)	V_{θ_1} (ft/s)	U_1 (ft/s)	w_{θ_1} (ft/s)	V_{x_1} (ft/s)	w_1 (ft/s)	β'_1 ($^\circ$)	$\Delta\beta'_1$ ($^\circ$)
10	23.0	37.79	14.77	94.81	80.04	34.79	87.27	66.5	-0.9
30	26.2	38.21	16.87	88.94	72.07	34.28	79.81	64.6	-0.9
50	28.9	39.21	18.95	83.08	64.13	34.33	72.74	61.8	-1.6
70	30.1	39.44	19.78	77.21	57.43	34.12	66.80	59.3	-1.5
90	33.5	41.23	22.76	71.35	48.59	34.38	59.52	54.7	-3.0

Table 3.10: Detailed flow measurement data, -6° 2/rev, $\Phi = 0.353$

% Imm.	β_1 ($^\circ$)	V_1 (ft/s)	V_{θ_1} (ft/s)	U_1 (ft/s)	w_{θ_1} (ft/s)	V_{x_1} (ft/s)	w_1 (ft/s)	β'_1 ($^\circ$)	$\Delta\beta'_1$ ($^\circ$)
10	12.8	35.68	7.90	94.81	86.91	34.79	93.61	68.2	+0.8
30	14.9	35.47	9.12	88.94	79.82	34.28	86.87	66.8	+1.3
50	17.4	35.98	10.76	83.08	72.32	34.33	80.05	64.6	+1.2
70	18.6	36.00	11.48	77.21	65.73	34.12	74.06	62.6	+1.8
90	21.4	36.92	13.47	71.35	57.88	34.38	67.32	59.3	+1.6

Table 3.11: Detailed flow measurement data, -16° 2/rev, $\Phi = 0.353$

% Imm.	β_1 ($^\circ$)	V_1 (ft/s)	V_{θ_1} (ft/s)	U_1 (ft/s)	w_{θ_1} (ft/s)	V_{x_1} (ft/s)	w_1 (ft/s)	β'_1 ($^\circ$)	$\Delta\beta'_1$ ($^\circ$)
10	3.9	34.87	2.37	94.81	92.44	34.79	98.77	69.4	+2.0
30	3.9	34.36	2.34	88.94	86.60	34.28	93.14	68.4	+2.9
50	6.2	34.53	3.73	83.08	79.35	34.33	86.46	66.6	+3.2
70	6.2	34.32	3.71	77.21	73.50	34.12	81.03	65.1	+4.3
90	8.9	34.80	5.38	71.35	65.97	34.38	74.39	62.5	+4.8

3.5 Low-Speed Compressor Conclusions

A review of literature related to dynamic stall was accomplished to get an idea of what reduced frequency at stall and what amplitude of blade setting angle variation should be used for tests involving a two-stage axial-flow fan and a three-stage axial-flow compressor. Preliminary tests were performed on a two-stage axial-flow fan to investigate whether or not the stall margin of an axial-flow fan or compressor could be improved by appropriately scheduling the setting angles of the stationary blades upstream of a rotor. A three-stage axial-flow research compressor was tested with a variety of inlet guide vane circumferentially varying setting angle patterns to confirm results obtained with the two-stage fan and to reach further conclusions about stall margin improvement capability. Additional three-stage compressor tests were performed with inlet guide vanes and first and second stage stator blades set in identical circumferentially varying setting angle patterns. A final set of performance tests were performed with all the inlet guide vanes set either 6° more or 6° less than the baseline setting angle. Some detailed measurements of the flow exiting the inlet guide vane row of the three-stage compressor were also acquired for the baseline compressor configuration as well as some modified compressor configurations.

The review of relevant literature suggested that the use of a reduced frequency value in the range from 0.30 to 0.35 would give the most benefit in terms of improving the stall margin of a compressor rotor row. The amplitude of airfoil oscillation, which varied from 5° to 20° in the literature reviewed, gave guidance about the magnitude of blade setting angle, $\Delta\phi$, used in the tests.

Tests of the two-stage axial-flow fan indicated that for several different circumferential variation patterns of stator blade setting angle, the fan stall limit could

be moved to lower flow coefficients. It was also noted that the magnitude of the stall margin increase was a function of the reduced frequency at stall, K_{stall} , and the amplitude of blade setting angle, $\Delta\phi$. The optimum increase in stall margin was observed to occur when the reduced frequency at stall was near a value of 0.3 and the amplitude of blade setting angle was in the range of $\Delta\phi$ from 5° to 7° .

Tests of the three-stage axial-flow research compressor involving a variety of circumferentially varying IGV row blade setting angle patterns set according to Equation (3.1) suggest that stall margin, head-rise production, and stall hysteresis could be improved by the appropriate setting of the IGV row blade setting angles in a circumferentially varying pattern. For these tests, the optimum reduced frequency at stall for increasing the stall margin was near 0.19. In addition, a slight shift in the "out of stall" point with compressor modification indicates that the modified compressor was actually relieved from stall sooner than the baseline compressor. The amplitude of blade setting angle, $\Delta\phi$, for the above modified compressor was held constant at 6° .

Tests of the three-stage axial-flow compressor with the inlet guide vanes set according to Equation (3.2), i.e., rectified sine wave angle variations, suggest that one-sided variations are not useful. When the rotor blades were periodically unloaded only, the drop in head-rise production from baseline was appreciable, too much to justify any gain in stall margin achieved. When the rotor blades were periodically loaded only, the increase in head-rise production was minimal and no gain in stall margin was observed. A significant degradation in stall point recovery occurred.

Tests of the three-stage axial-flow compressor with the inlet guide vanes set according to Equation (3.3), i.e., asymmetric angle variations, suggest that asymmetric

angle variations can lead to increased head-rise production and improved stall margin. However, stall recovery improvement was not observed. Also, larger angle variation amplitudes result in significant stall margin degradation.

A test of the three-stage axial-flow compressor with the inlet guide vanes, and first and second stage stator blades all set in the same circumferentially varying periodic and symmetrical pattern suggest that while setting an accelerating row of blades, e.g., inlet guide vanes, in such a pattern may improve modified compressor performance in terms of stall margin, stall hysteresis and head-rise production, similar setting of diffusing blades, e.g., stator blades, may lead to worsened modified compressor performance.

A set of tests was performed on the three-stage compressor in which all inlet guide vanes were set either 6° more or less than the baseline setting angle. Results suggested that a significant unloading of the compressor occurred when the blades were set 6° more than baseline. Only a slightly higher loading was achieved when the blades were set 6° less than baseline. These tests also indicated the benefit of periodically varying the blade setting angles around the circumference as compared to simply setting all the blades 6° more or less than the baseline setting angle.

Detailed measurements taken on the low-speed, three-stage compressor suggested that the actual turning of the flow behind the inlet guide vanes was approximately equal to the amplitude of setting angle variation in the inlet guide vane row. The data also confirmed the idea that inlet guide vane turning is independent of varying flowrates at Mach numbers less than 0.3. A comparison between detailed measurement calculated and estimated values of reduced frequency at stall and extent of rotor inlet flow angle variation suggest that the estimated values are valid.

Results from the low-speed compressors suggested that slight improvements in stall margin and recovery were possible with compressor modifications using an appropriate scheduling of the setting angles of the inlet guide vanes upstream of a rotor. The varying success of these low-speed tests was primarily a function of the setting angle pattern used, the reduced frequency at stall, and the estimated rotor inlet flow angle variation. These preliminary extensions of dynamic stall notions to turbomachine flows suggests that further studies were warranted. For this reason, the idea for improving the stall margin through the use of circumferentially varying stationary blade setting angles was tested on a higher-speed, three-stage, axial-flow compressor.

4. PRATT & WHITNEY COMPRESSOR

A Pratt & Whitney, intermediate-speed, three-stage, axial-flow research compressor was used to test the effects of compressibility on the proposed method for improving the stall margin of axial-flow compressors. The research compressor and related equipment, located in the Turbomachinery Components Research Laboratory of Iowa State University, are described in the following sections. The design and installation of the data acquisition system used on the Pratt & Whitney research compressor is also described.

4.1 Pratt & Whitney Axial-Flow Compressor

The Pratt & Whitney, intermediate-speed, three-stage, axial-flow compressor is described in this section. Shown in Figure 4.1 is the compressor test stand including (from right to left) the drive motor, gearbox, inlet flow ductwork, compressor, flowrate measurement section, throttle housing and exit flow ductwork. This compressor was used for testing the effects of compressibility on the proposed method of improving the stall margin of axial-flow compressors.

The configuration of the compressor consisted of a set of inlet guide vanes followed by three stages of rotor and stator blade rows (see Figure 4.2). The blade rows were within an annulus having a constant tip (24.000 in. (0.610 m)) diameter.

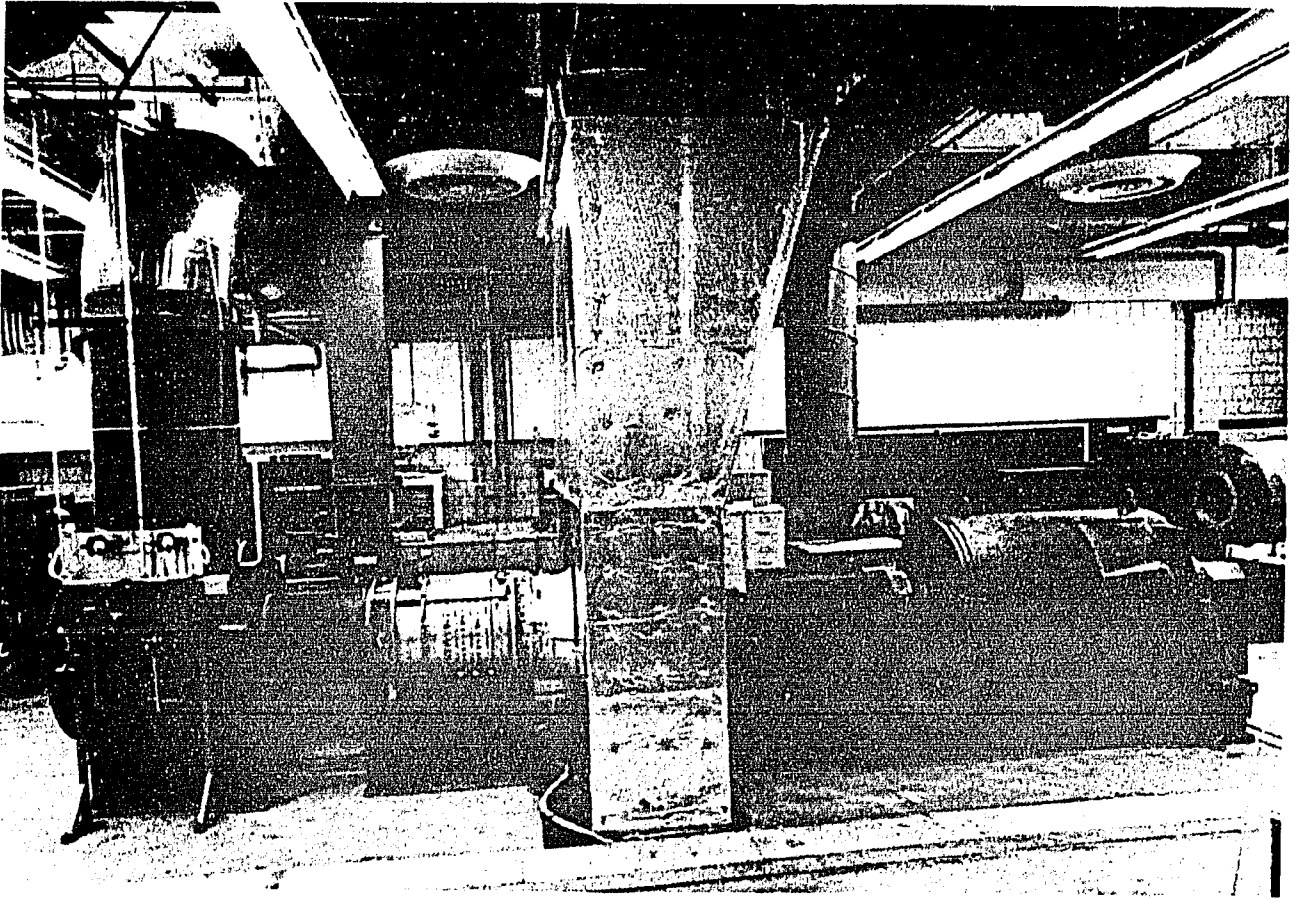


Figure 4.1: Pratt & Whitney research compressor test stand

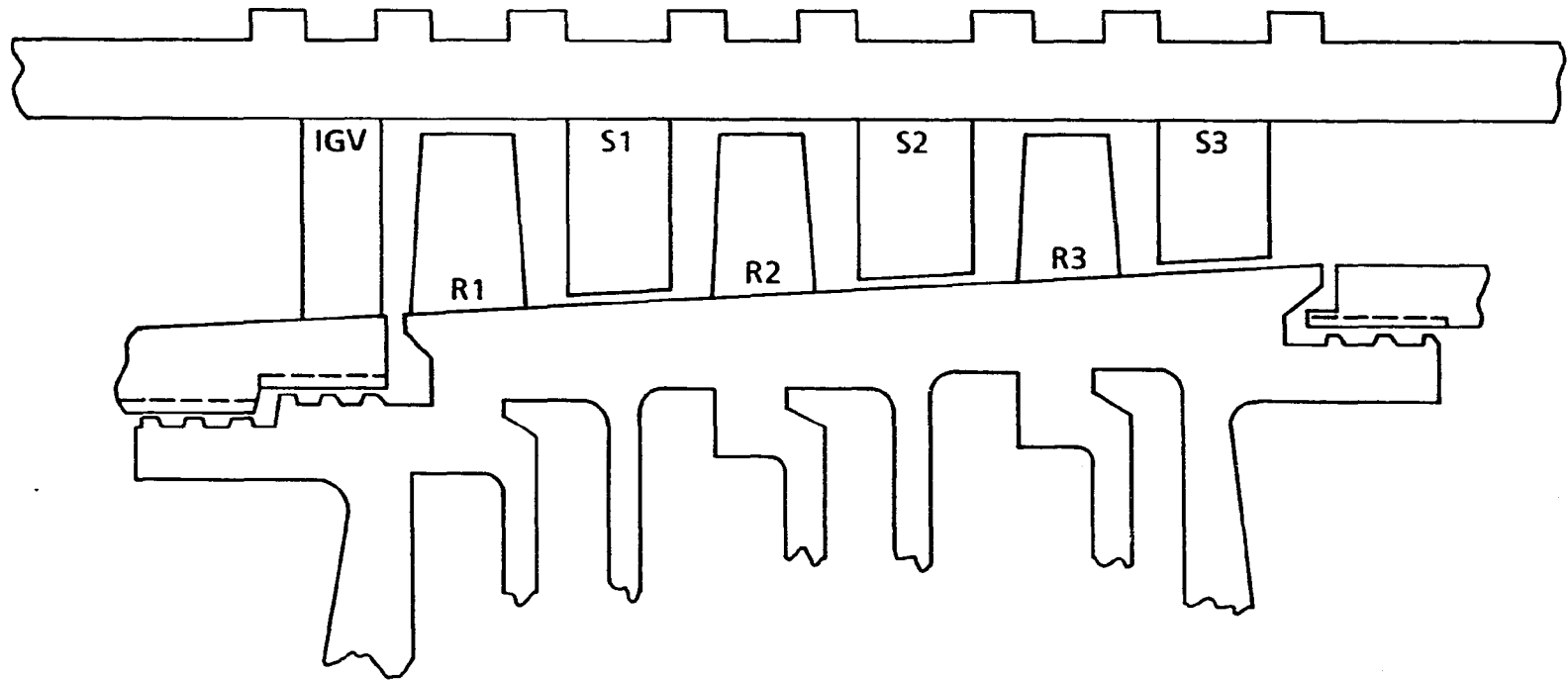


Figure 4.2: Pratt & Whitney compressor detail

Table 4.1: Pratt & Whitney compressor design specifications

Number of stages	3
Design corrected rotor speed, rpm	5700
Design corrected mass flow, lb/sec	15.40
Design overall pressure ratio	1.350
Tip Diameter, in.	24.0
Average hub-tip ratio	0.843
Average aspect ratio	1.0
Average gap to chord ratio	0.78
Average diffusion factor	0.468

The annulus hub diameter varied from 19.876 in. (0.505 *m*) at the inlet to 20.590 in. (0.523 *m*) at the exit resulting in an average hub/tip ratio of 0.843. Overall compressor design conditions and blade specifications are summarized in Tables 4.1 and 4.2. The inlet guide vanes were shrouded while the rotor and stator blades were cantilevered from the hub wheel and outer casing, respectively. The compressor blades were precision cast from high strength aluminum alloy. The blades had cylindrical trunions for rigid attachment to the stator blade row rings and rotor wheel carriers. These blades could be restaggered as needed.

The compressor utilized outside ambient air ducted to a large plenum surrounding the compressor inlet bellmouth. Air flowed through a cylindrical honeycomb flow straightener to provide compressor inlet flow with minimum swirl. A conical throttle was located downstream of the compressor exit. The throttle was used to vary the flowrate and could be immediately relieved in the event of compressor surge or stall. Further details about the compressor drive system, throttle and surge detection and relief system are discussed in the following subsections. Additional design and installation information was reported by Thompson [13].

Table 4.2: Pratt & Whitney compressor blading specifications

Item	No. of Blades	Chord (in.)	Span (in.)	Aspect Ratio	Setting Angle Radius (in.)	Setting Angle (°)
Inlet guide vane	100	0.700	2.100	3.000	10.963	102.2
Rotor Blades						
Stage 1	44	2.013	2.005	0.996	10.998	129.99
Stage 2	47	1.895	1.885	0.995	11.058	130.17
Stage 3	50	1.790	1.778	0.993	11.110	129.86
Stator Vanes						
Stage 1	46	1.932	1.943	1.006	11.029	120.09
Stage 2	49	1.823	1.828	1.003	11.086	122.02
Stage 3	52	1.725	1.705	0.988	11.222	123.49

4.1.1 D.C. drive motor and gearbox

The motor drive for the compressor test rig was a Westinghouse 500 HP cradled D.C. dynamometer which had a speed range of 800 rpm to 3000 rpm. The drive motor was powered by a Reliance Electric Maxplus electronic drive. Additional specifications for the D.C. drive motor are listed in Table 4.3.

A gearbox was used to increase the compressor shaft speed by a ratio of 2.51 to 1 above the compressor drive motor speed. The gearbox had a maximum output rotational speed of 6026, at a thermal rating of 450 HP. The gearbox oil was cooled by pumping DTE-26 oil through the tube side of a closed loop shell and tube heat exchanger. A chilled water supply was used for cooling the oil on the shell side of the exchanger. The gearbox was also instrumented with a thermocouple and a pressure switch to monitor maximum oil temperature and pressure. If either a set pressure or temperature was exceeded, a shutdown of the compressor drive was electronically initiated. The shutdown consisted of interrupting the power applied to the D.C. drive motor with the compressor subsequently coasting to a complete stop.

4.1.2 Throttle

A sketch of the throttle assembly for the research compressor is shown in Figure 4.3. Compressor exit air entered the flowrate measurement section and left through a cylindrical duct before reaching the throttle cone. The cylindrical duct extending upstream out of the throttle housing was mounted on rollers enabling the cylindrical duct and throttle cone to move relative to the compressor exit allowing access to the flowrate measurement section. The rate of airflow was varied by axial movement of the throttle cone. A threaded rod attached to a low speed A.C. drive motor and the

Table 4.3: D.C. drive motor specifications

Manufacturer:	Westinghouse
Serial Number:	2S20P219
Instruction Book Number:	5107
Horsepower:	500
Armature Volts:	500
Armature Amps:	830
Field Volts:	250
Field Amps (max.):	5
Field Resistance (D.C.):	28 ohms
RPM:	800/3000

throttle cone provided the throttle movement. The throttle cone was also equipped with an air cylinder for rapid flow area increase in the event of compressor surge or stall. The surge detection system is discussed in the following subsection.

4.1.3 Surge detection and relief system

The compressor throttle was provided with a built in mechanism for detecting and relieving compressor surge or stall. In Figure 4.4 is shown the compressor surge/stall detection and relief system. The compressor throttle cone used an air cylinder with high pressure air applied to allow steady as well as rapid movement of the throttle cone. The throttle was opened rapidly by venting the high pressure air applied to the air cylinder through a three-way solenoid valve (see Figure 4.4). The solenoid was activated at the operator station manually or automatically by the surge/stall detection system. Activating the solenoid resulted in the cylinder air being vented and the supply air being cut-off. The force of the flowing compressor exit air on the throttle cone moved it backward allowing the compressor to recover.

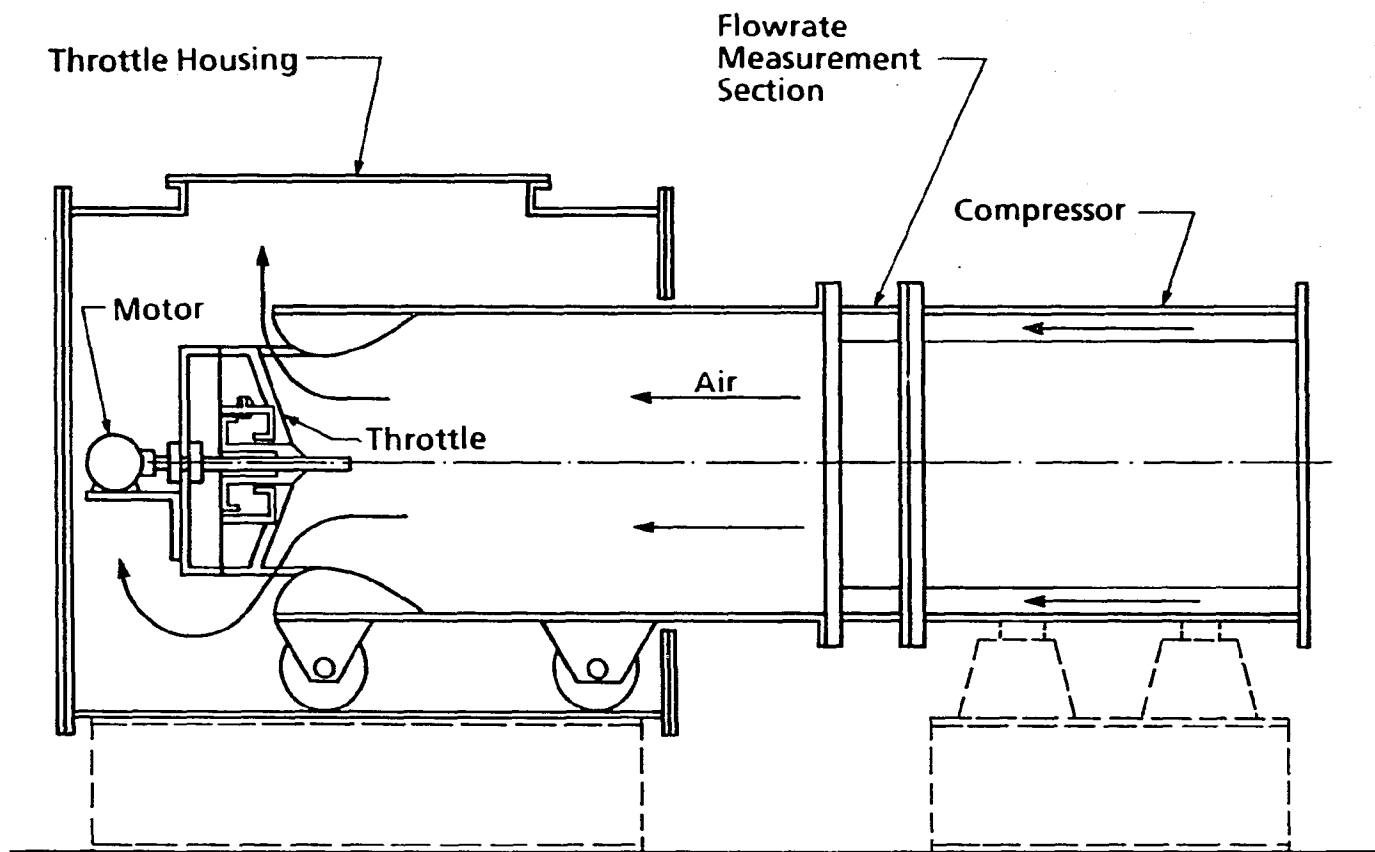


Figure 4.3: Pratt & Whitney throttle section detail

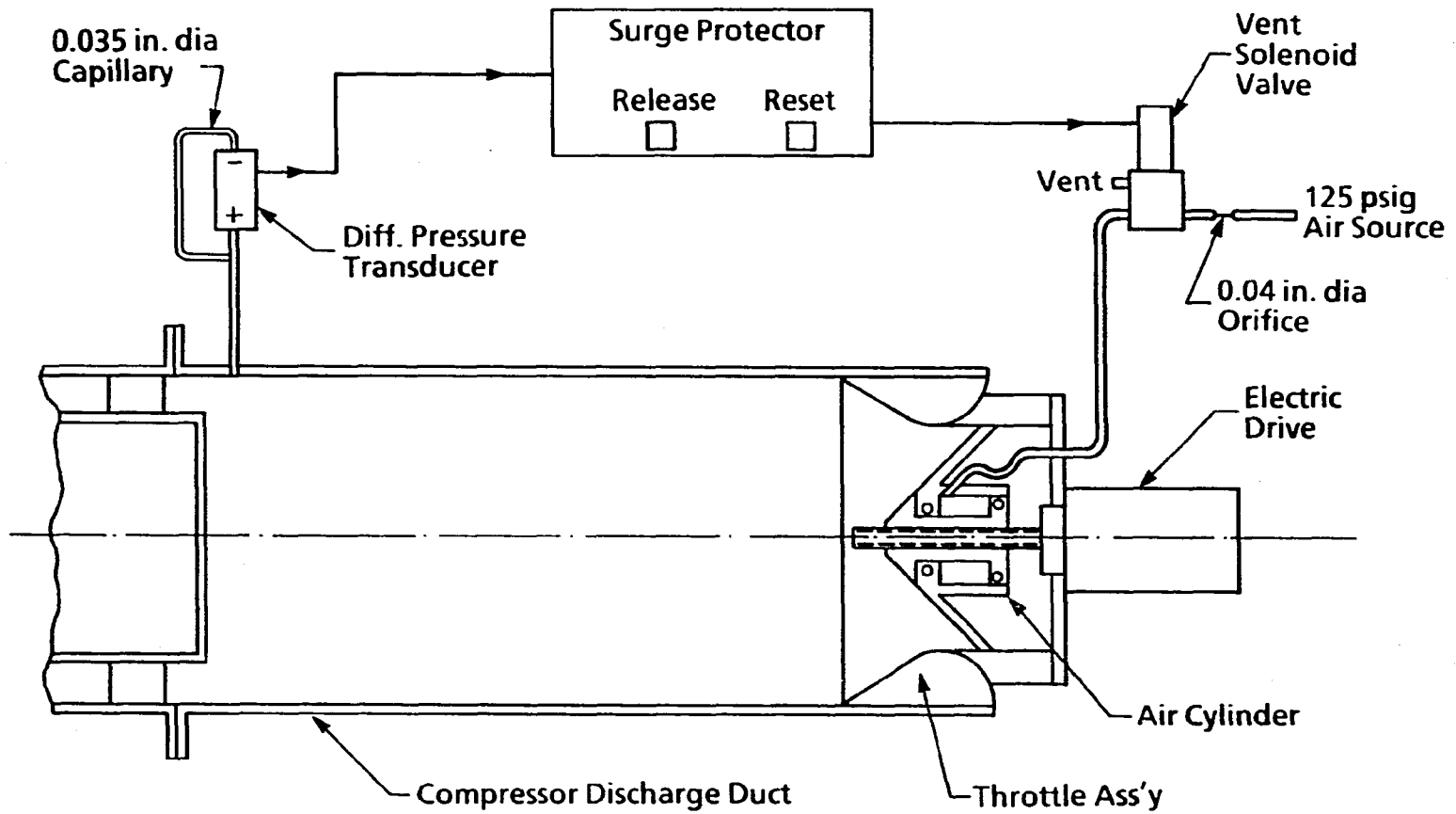


Figure 4.4: Pratt & Whitney automatic surge detection and relief system

The automatic surge/stall detection system used a high frequency differential pressure transducer to detect static pressure transients downstream of the final stator blade row. The pressure transducer monitored the pressure difference between a static tap in the compressor outer casing and a small capillary tube that tees into the static tap tube. This setup resulted in a fast response pressure signal at the positive port and a very slow response pressure signal at the negative pressure port. The output signal from the differential pressure transducer was monitored by a digital, peak and hold, differential pressure signal conditioner and readout. The readout meter had a "set point" function that determined the maximum allowable differential pressure. In the event of compressor surge or stall, the pressure signal conditioner was "tripped" and the air cylinder solenoid was activated with subsequent relief of the compressor from the related compressor instability. Both the manual and automatic methods for relieving the compressor from surge or stall were used in the present investigation.

4.2 Pratt & Whitney Compressor Data Acquisition System

The Pratt & Whitney compressor data acquisition system was designed and implemented during the course of this investigation and is described in detail in the following subsections. The two major areas of data acquisition, namely, pressure and temperature scanning are discussed. The selection of appropriate data acquisition equipment for the testing environment is described.

4.2.1 Pressure system

Most of the pressure measurements in the intermediate-speed, three-stage, axial-flow compressor were made with the system shown in Figure 4.5. The system involved a Scanivalve ZOC14 electronic pressure scanning module specifically designed for turbine engine testing applications. This state-of-the-art pressure scanner was chosen for its compact size, high scanning rate, accuracy and flexibility when used for aerodynamic testing. In addition, the Scanivalve ZOC14 along with support equipment from Scanivalve could be easily incorporated into existing data acquisition equipment already available in the research laboratory. The methods of installation and operation of the Scanivalve pressure system are discussed in further detail.

The Scanivalve ZOC14 is an electronic pressure scanner which accepts 32 pneumatic pressure inputs and converts them to computer compatible electrical signals. The ZOC14 module (see Figure 4.6) contained 32 individual silicon pressure sensors, each with a nominal differential pressure range of 10 psi. The 10 psi differential range was selected because it enveloped the maximum anticipated pressure levels in the compressor and still allowed good full scale accuracy. The maximum scanning rate of the scanner is 100kHz when used with a photo-optical Darlington switch. Ac-

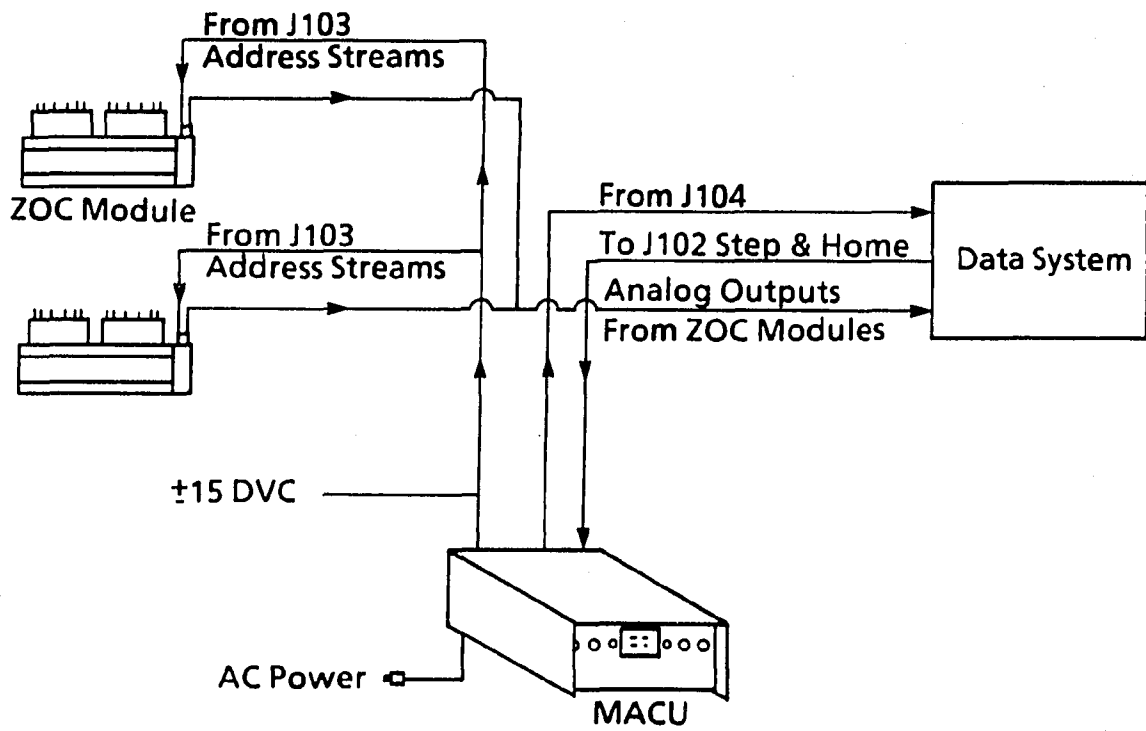


Figure 4.5: Scanivalve pressure system diagram

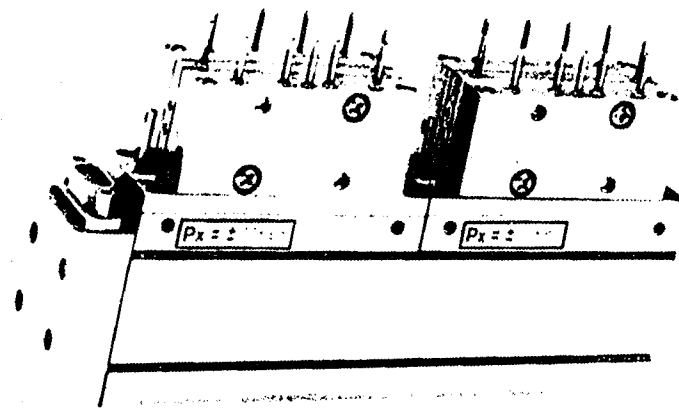


Figure 4.6: Scanivalve ZOC14 pressure scanning module

tual test scanning rates, however, were significantly lower because of the limitations imposed by the Hewlett-Packard 3495A scanner that was used.

The ZOC14 is capable of four modes of operation: operate, calibrate, purge and isolate. Each of these modes can be activated by applying an appropriate pneumatic control pressure (≈ 90 psi) to the ZOC14 module. The normal operating mode of the ZOC14 is the "operate" mode. The 32 individual pneumatic pressures are sensed and converted to voltage signals in this mode. The "calibrate" mode allows for the calibration of each individual sensor with some known calibration pressure. This mode allows the ZOC14 sensors to be automatically calibrated on-line without interrupting the test run. The last two modes of operation of the ZOC14 are the "purge" and "isolate" modes. These modes purge impurities which may be introduced through the pneumatic pressure lines and isolate the ZOC from any pneumatic pressures.

For the ZOC14 module to operate consistently and accurately, the entire unit was installed in a Scanivalve Thermal Control Unit (TCU, see Figure 4.7). The TCU was designed to provide a constant temperature environment for the ZOC14 scanning module. The ZOC TCU minimizes the need to frequently recalibrate the silicon pressure sensors because of exposure to varying ambient temperatures. By use of a thermostatically controlled heater housed in a well insulated enclosure, temperature changes within the Thermal Control Unit were less than 0.1°C from a nominal factory setpoint temperature of 40°C .

The final piece of support equipment for the Scanivalve ZOC14 pressure scanning module was a Scanivalve Mux Address Control Unit (MACU, see Figure 4.8). The ZOC MACU is a compact address control unit that is capable of generating an address stream based on commands from the data acquisition system. The MACU displays

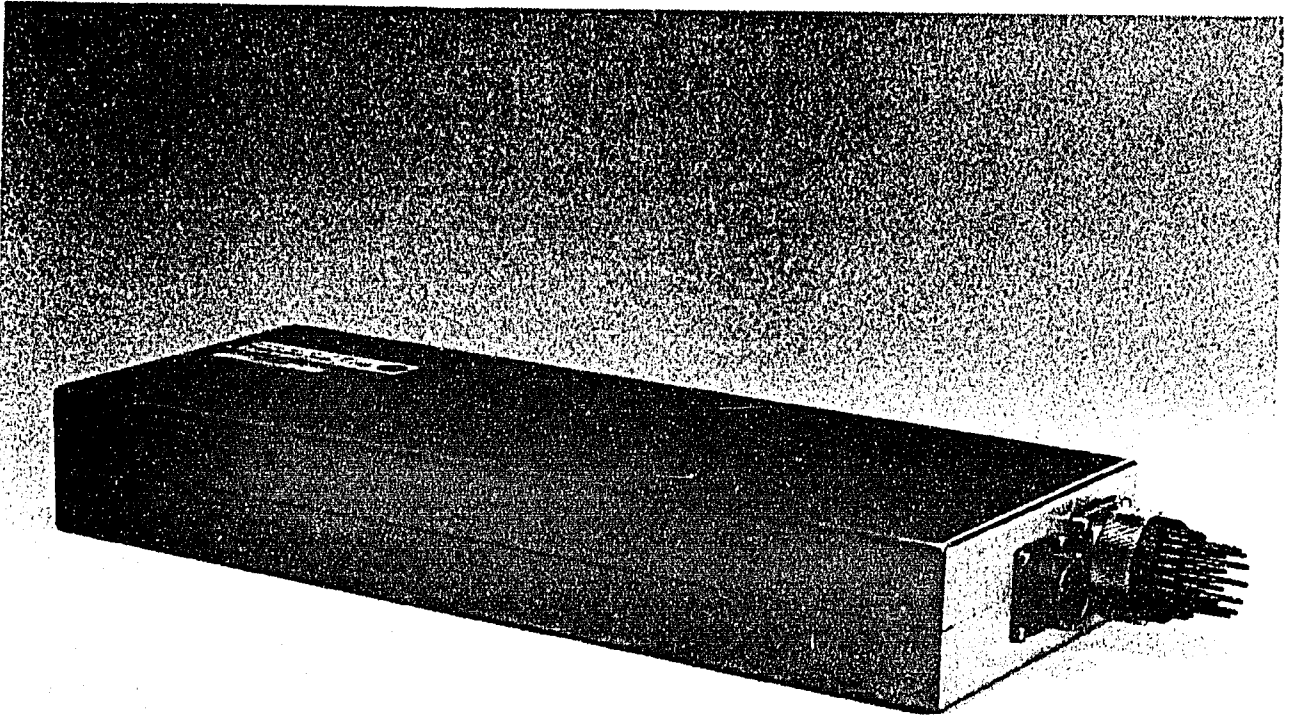


Figure 4.7: Scanivalve Thermal Control Unit (TCU)

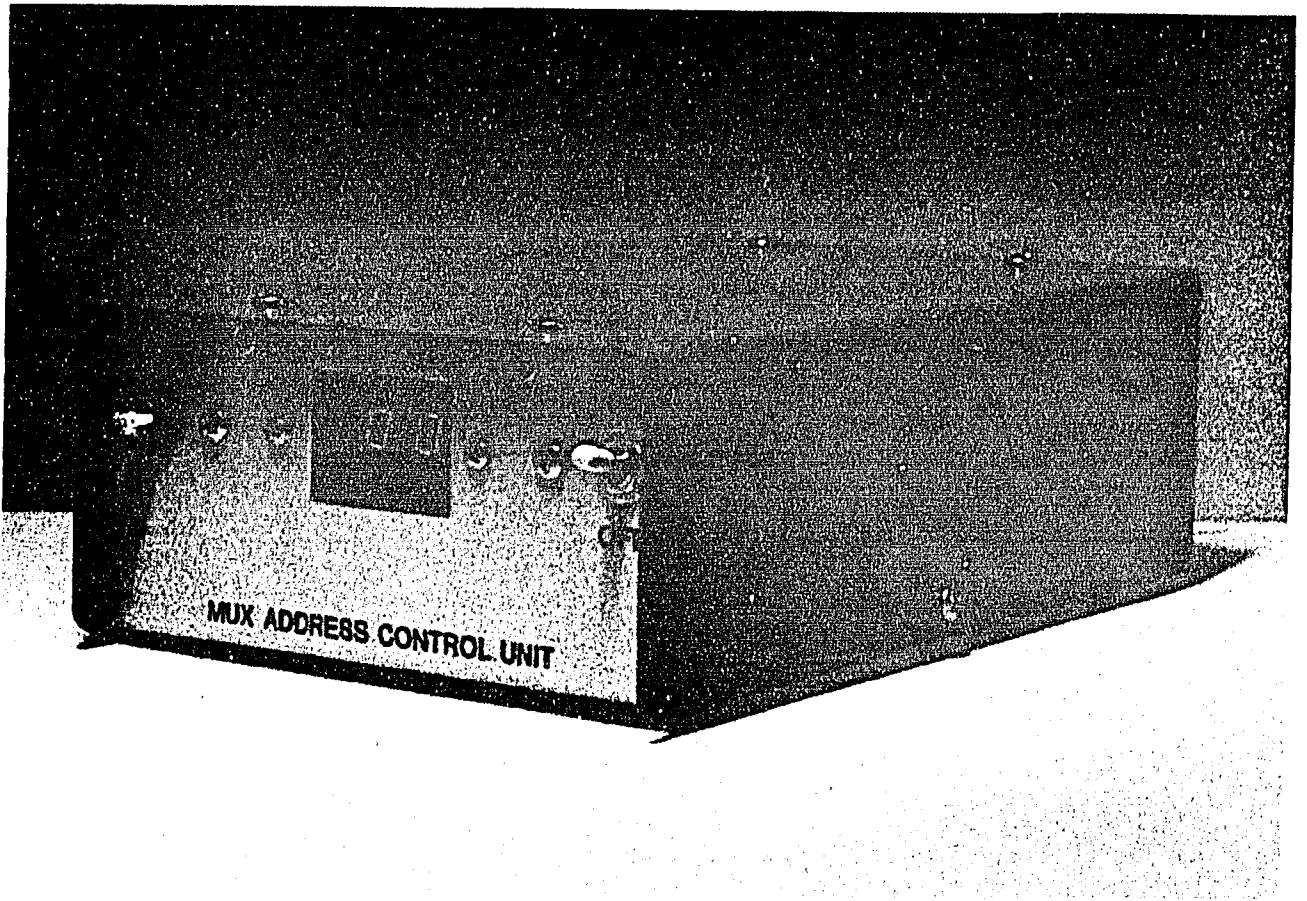


Figure 4.8: Scanivalve Mux Address Control Unit (MACU)

the current pressure channel being monitored and sends back a binary string code to the data acquisition system for channel verification.

4.2.1.1 Pressure system setup and electrical diagram The system setup and electrical diagram for the entire pressure scanning system are described in this subsection. The three Scanivalve ZOC components, namely, pressure sensor module, thermal control unit and mux address control unit, were supplied with required voltage sources and wired into existing laboratory data acquisition equipment.

The identification of required power supplies was the first step in the design of the pressure system control logic. Each component of the Scanivalve pressure scanning system required a different power supply as listed in Table 4.4. The power supplies were mounted on a steel plate attached to a 19 in. rack mounted panel for use in a portable rack enclosure. In addition to the power supplies, the control panel also contained the electronics and hardware for operating in the four different pressure scanning modes (operate, calibrate, purge and isolate). To operate in each of these four modes, a 90 psi pneumatic control pressure was applied to two different control pressure connections as indicated in Table 4.5.

The control panel housed two Asco 120 volt A. C., 2-way red-hat solenoid valves for applying the control pressure as needed. Control logic for the four different modes of operation was designed so that a red light was illuminated indicating which mode of operation was in effect. A series of +24 VDC relays and indicator lights were used to accomplish this result. The schematic for the control pressure solenoid activation and corresponding indicator lights is shown in Figure 4.9. The four different modes of operation could be activated by the appropriate switching (on-off) of two 24 volt

Table 4.4: Scanivalve pressure system power supplies

<u>Scanivalve Component</u>	<u>Power Supply Specification</u>
ZOC14 pressure scanner	± 15 volts dc at 1.2 amp
Thermal control unit	+24 volts dc 120 Watts
Mux address control unit	+24 volts dc and 120 volts ac

Table 4.5: Control pressure logic

<u>Mode</u>	<u>Control Pressure</u>	
	<u>CTL 1</u>	<u>CTL 2</u>
operate	none	none
calibrate	90 psi	none
purge	none	90 psi
isolate	90 psi	90 psi

relays.

Designing the data acquisition system also involved developing a complete electrical circuit wiring diagram and specifying hook-up instructions for the electronics to a digital voltmeter and a scanner for ultimate control of the pressure scanning system. In Figure 4.10 is shown the electrical wiring diagram for the pressure scanning system. The diagram contains electrical wiring information for the ZOC connector, the MACU (J102, J103 and J104) connectors and the power supply connections. The ZOC14 module contains the pressure scanning sensors as well as the thermal control unit (TCU) circuitry. The MACU J102 connector accepts "step" and "home" commands from the scanner and actuates the switching of pressure channels on the mux address control unit (MACU). The J103 connector sends a signal from the MACU to the ZOC module to switch the channel being scanned or to return the pressure scanner to the home position. The J104 connector outputs a binary code indicating the channel being scanned that has to be deciphered by the data acquisition system. Further description of the implementation of this system into the existing laboratory data system is presented in the following subsection.

4.2.1.2 Pressure system implementation into existing data system

The implementation of the pressure system electrical design into the existing data system is discussed in this subsection. The available data system consisted of a Hewlett-Packard 3455A digital voltmeter, a Hewlett-Packard 3495A scanner and a Zenith data systems computer. The Zenith computer controlled the operations of the digital voltmeter and scanner through a National Instruments IEEE-48 computer interface utilizing GPIB-PC function commands. Zenith computer programs to control

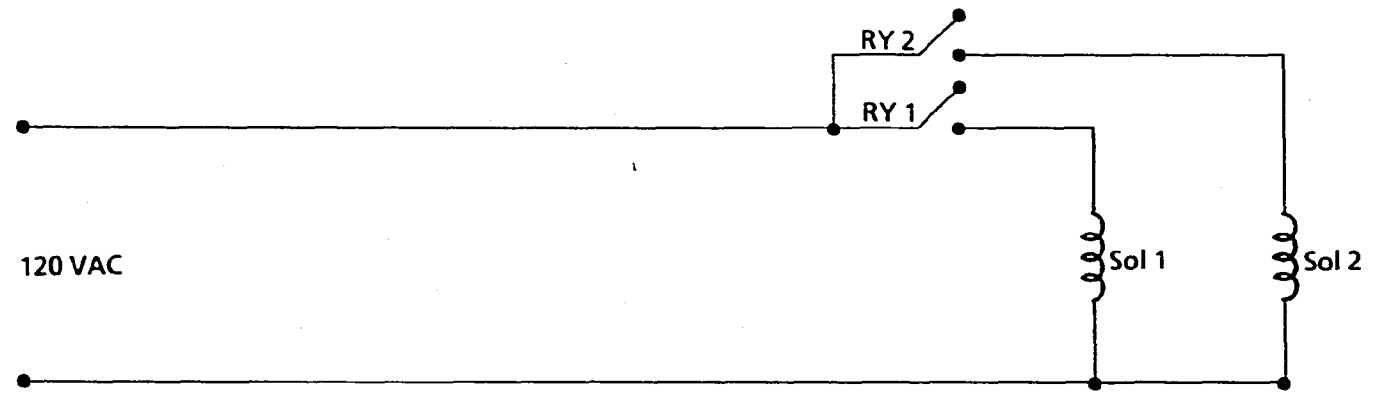
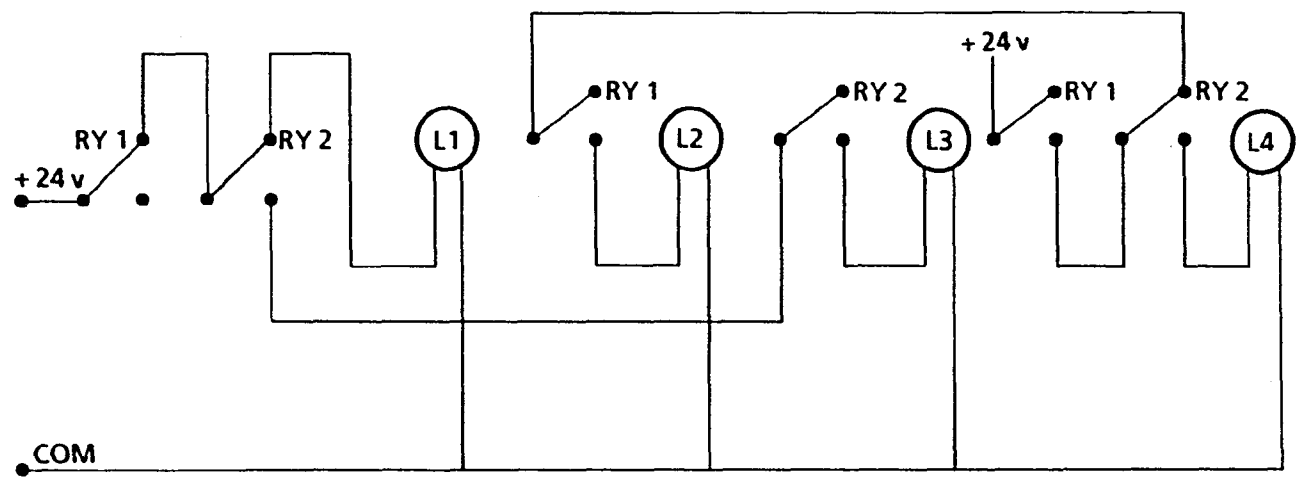


Figure 4.9: Control pressure electrical circuit diagram

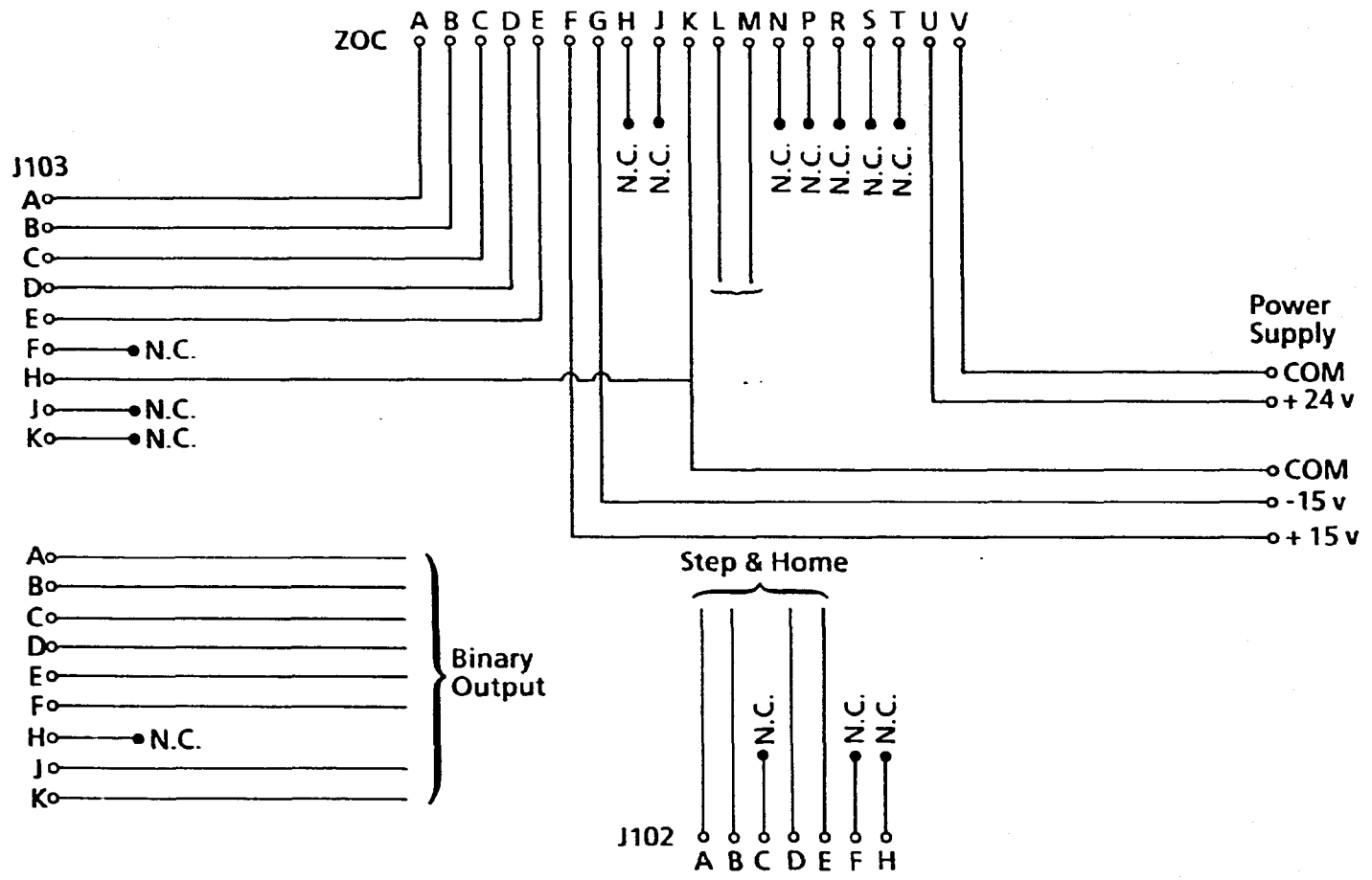


Figure 4.10: Electrical wiring diagram for ZOC pressure scanning

the function of the data acquisition system were written in Quick Basic language.

Two major operations were used to implement the Scanivalve pressure system into the available data system, namely, reading and logging dc voltages from the digital voltmeter and controlling relay switches on the scanner. By using these operations, the ZOC14 pressure scanner could be stepped and homed, the ZOC output voltage could be read, and the binary code produced by the MACU could be deciphered. These important pressure system operations will be discussed briefly.

First of all, the "step" and "home" commands were created by the sequential opening and closing of two scanner relays. The "step" operation caused the ZOC channel being scanned to be incremented by one channel (or pneumatic pressure input). The "home" operation caused the ZOC scanner to return to its initial scanning position (Channel 0). The scanning rate of the system was limited by the speed at which the scanner relays could be opened and closed. The maximum scanning speed used for data acquisition purposes was about eight channels per second (≈ 8 Hz). A simple sketch of the scanner electrical hook-up for the step and home operations is shown in Figure 4.11. A step is accomplished by opening and closing switch 1 (SW 1) followed by closing switch 2 (SW 2). A home command is accomplished by closing switch 3 (SW 3). The scanner automatically reopens a switch when a new command is given to open or close an alternate switch.

The second important operation for the data system was the reading of the ZOC14 output voltage. The dc voltage was read by the digital voltmeter (wires L and M in Figure 4.10). This dc voltage was directly proportional to the pressure being applied to the individual silicon sensor. Each sensor, however, had a different proportionality constant associated with it. The method of calibration of these silicon

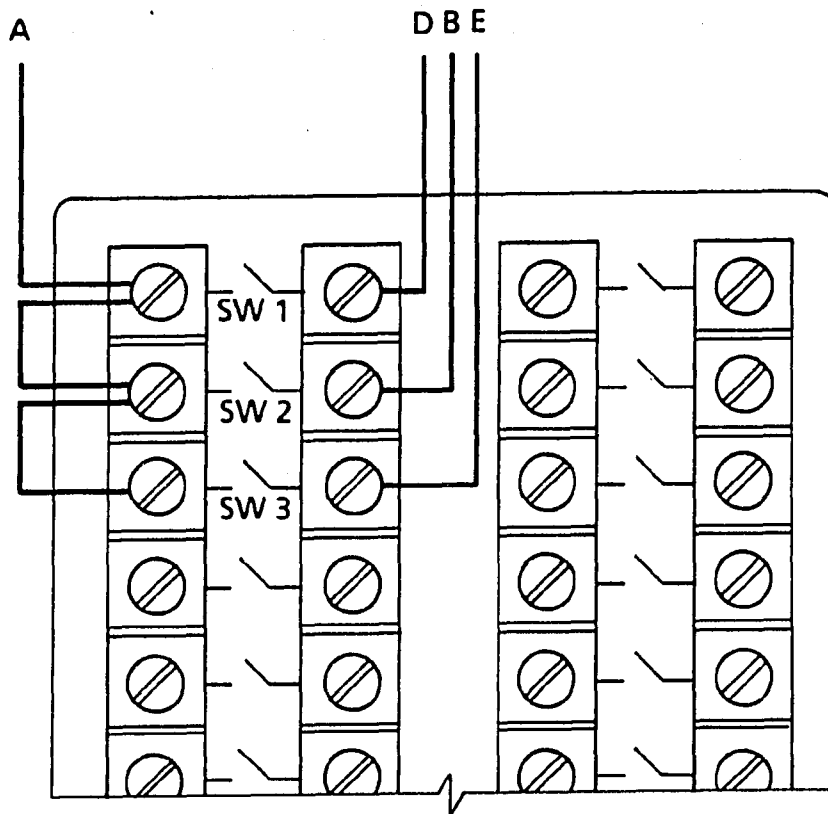


Figure 4.11: Using "Step" and "Home" commands on HP scanner

pressure sensors is discussed in the pressure system calibration subsection.

The deciphering of the binary code produced by the ZOC MACU was the final pressure system operation. The deciphering of this code enabled the data system to verify the channel being scanned. The binary code string flowed from connector J104 on the MACU. The connector contained six open collector NPN transistors with a maximum saturation voltage of 0.5 volts when "on". An external 24 volt dc power supply was required for the deciphering operation. In Figure 4.12 is shown the six NPN transistor connectors labeled A through F. Each connector has a different binary number associated with it and they are indicated in the diagram.

The diagram shows a parallel arrangement of pull-up resistors and a voltmeter which must be examined for deciphering purposes. Each circuit voltage (A through F) must be read and recorded. The resulting voltage values reflect either an "on" or "off" condition for the NPN transistors. The channel being scanned is calculated by adding the binary numbers of the NPN transistors which indicate an "off" condition.

4.2.1.3 Pressure system calibration The calibration procedure for the Scanivalve ZOC14 pressure scanner is discussed in this subsection. The ZOC14 pressure module contained 32 individual silicon sensors each having a different calibration constant. Each sensor had a nominal differential pressure range of 10 psi, and was therefore calibrated in this range. A seven point calibration for each of the 32 individual sensors was performed.

The calibration involved a small air compressor and a 30 inch mercury manometer. The air compressor provided a variable pressure source in the 0 to 10 psi range.

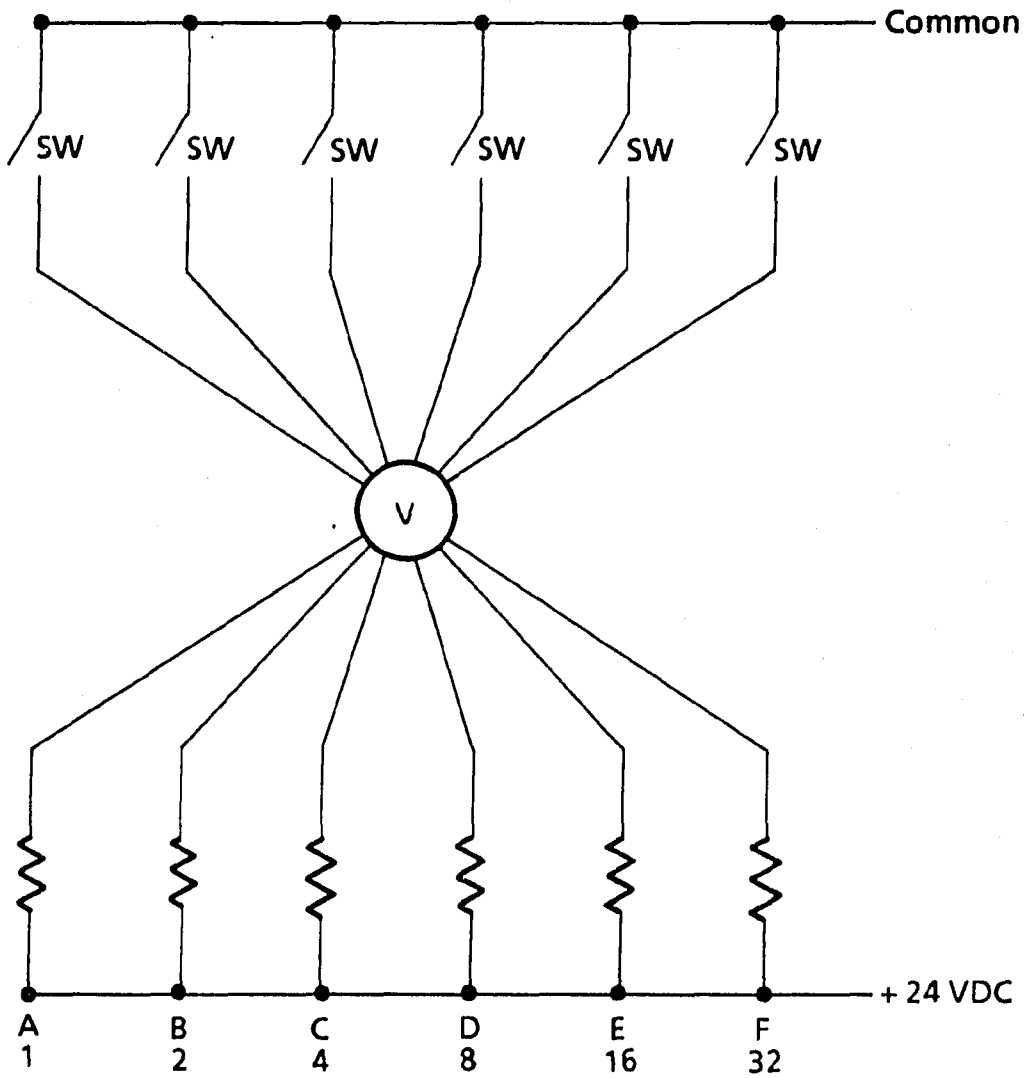


Figure 4.12: NPN transistor connectors for binary code deciphering

The mercury manometer was used to measure precisely the pressure of the variable source.

The calibration procedure began by switching on the pressure system electronics. A two hour warm-up time was required for the thermal control unit (TCU) to reach thermal equilibrium. Because the silicon sensors were sensitive to thermal gradients, a calibration performed before the system was stable yielded erroneous results. When the pressure measuring system was in equilibrium, a scan of the 32 individual sensors indicated a non-zero initial voltage for each. This initial voltage was most likely due to stresses applied to each silicon sensor during manufacturing and it remained constant throughout the calibration and during subsequent testing.

Seven nominal pressure source values were chosen for calibration, namely, 0.0, 2.0, 4.0, 5.0, 6.0, 8.0 and 10.0 psi. The calibration pressure was applied to each of the silicon pressure sensors and voltage readings were taken. This process was repeated with the remaining calibration pressures to arrive at calibration curves for each of the 32 sensors. This calibration procedure was then repeated immediately to verify that the calibration curves remained constant. In Figure 4.13 is shown the calibration curve for channel number 24 of the ZOC14. Other calibration curves for the remaining ZOC channels were similar with different slopes, however. The slope of the calibration curve of voltage versus pressure gives the calibration constant. Table 4.6 lists the calibration constants calculated for the 32 individual silicon pressure sensors. During the Pratt & Whitney compressor tests, calibration constants were checked periodically and did not vary.

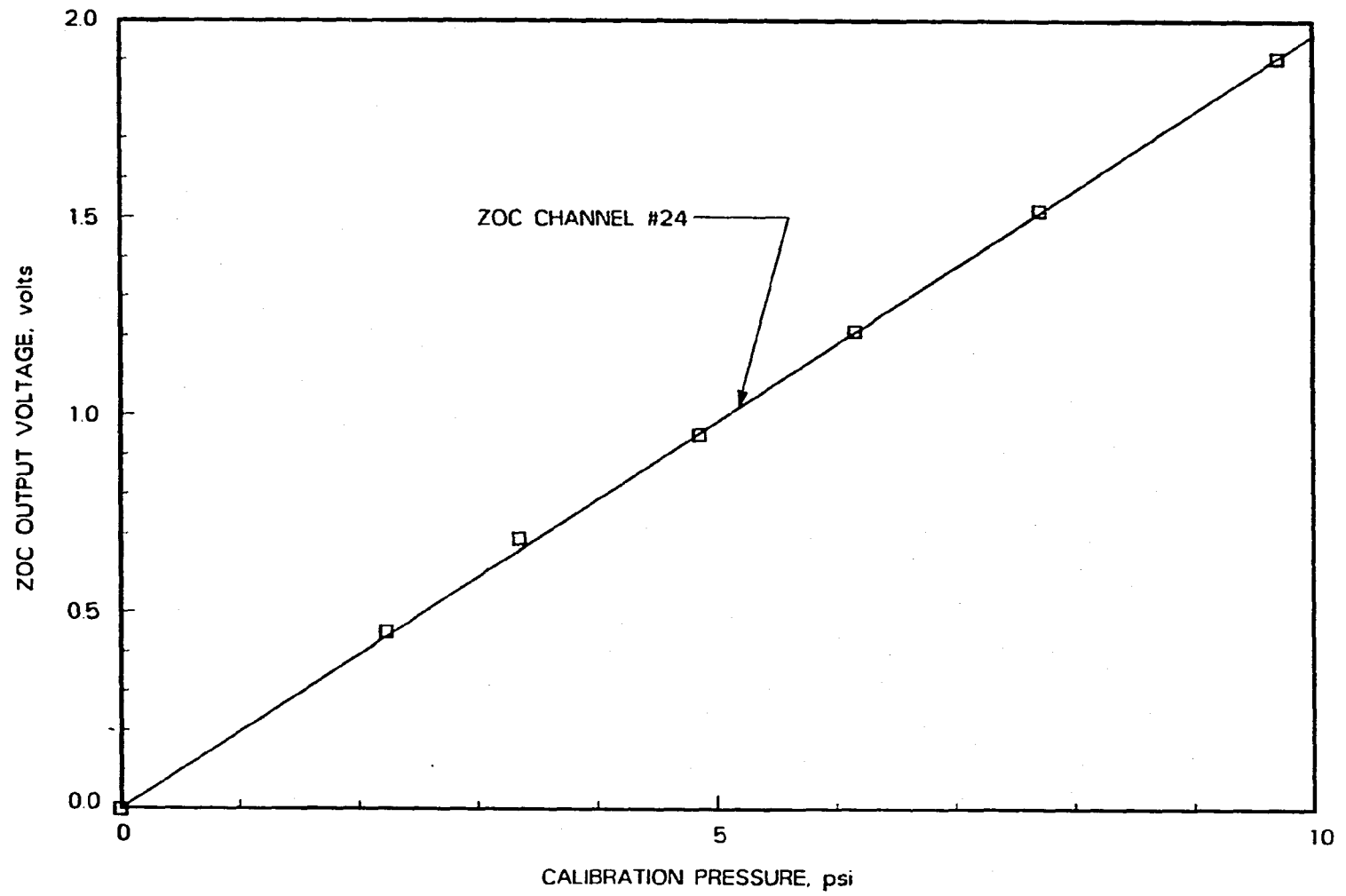


Figure 4.13: Calibration curve for ZOC channel #24

Table 4.6: Calibration constants for the ZOC14 pressure sensor

Channel #	Calib. Con.	Channel #	Calib. Con.
1	5.226	17	3.797
2	4.986	18	4.011
3	4.857	19	3.678
4	4.125	20	4.416
5	4.089	21	4.147
6	4.067	22	4.208
7	4.056	23	4.259
8	4.161	24	4.734
9	4.140	25	4.622
10	4.732	26	4.782
11	3.835	27	4.915
12	4.045	28	5.059
13	3.861	29	4.769
14	3.736	30	5.053
15	4.102	31	5.045
16	4.200	32	5.269

4.2.2 Temperature system

The temperature data acquisition system used with the intermediate-speed, three-stage, axial-flow compressor is described in this subsection. The temperature measurement system consisted of chromel-alumel thermocouples attached to total-temperature probes. Individual thermocouples were hooked-up to the Hewlett-Packard 3495A scanner in a parallel arrangement. The scanning of up to 40 different thermocouples was performed by the Zenith computer. An Omega-CJ cold junction compensator was used to provide a reference point from which to base the thermocouple emf. The emf voltage was read by the Hewlett-Packard 3455A digital voltmeter. Using the following equation provided by Omega, the thermocouple temperature was calculated.

$$T = a_0 + a_1x + a_2x^2 + a_3x^3 + \dots + a_mx^m \quad (4.1)$$

where

T = thermocouple absolute temperature

x = thermocouple emf voltage

a = polynomial coefficient for chromel-alumel thermocouple

m = maximum order of the polynomial

In this case, an 8th order polynomial was used to calculate the thermocouple temperature. The polynomial coefficients for a Type K, chromel-alumel thermocouple are tabulated below. This 8th order polynomial resulted in a thermocouple temperature accuracy of $\pm 0.7^\circ$. The values of polynomial coefficients used are:

$$a_0 = 0.226584602$$

$$a_1 = 24152.10900$$

$$a_2 = 67233.4248$$

$$a_3 = 2210340.682$$

$$a_4 = -860963914.9$$

$$a_5 = 4.83506 \times 10^{10}$$

$$a_6 = -1.18452 \times 10^{12}$$

$$a_7 = 1.38690 \times 10^{13}$$

$$a_8 = -6.33708 \times 10^{13}$$

4.3 Pratt & Whitney Three-Stage Compressor Performance Tests

The Pratt & Whitney, intermediate-speed, three-stage compressor was used for the purpose of identifying the effects of compressibility on the proposed method for improving the stall margin of multistage, axial-flow compressors. The results previously obtained with the two-stage fan and the three-stage compressor were used to guide the Pratt & Whitney compressor tests. Because the Pratt & Whitney compressor was a significantly more complex turbomachine than the two-stage fan and three-stage compressor, the test procedures are explained in detail.

The overall performance characteristics for the Pratt & Whitney, intermediate-speed, three-stage, axial-flow compressor were determined by the measurement of inlet corrected mass flow, compressor total-pressure rise and inlet corrected rotational speed. These performance parameters were carefully measured throughout the test program to assure accurate and consistent results. The methods used to determine these performance parameters are discussed in the following sections.

4.3.1 Inlet corrected mass flow

The flowrate for the Pratt & Whitney compressor was measured in an instrumented annulus section located downstream of the compressor exit (see Figure 4.3). The measurement section could be easily separated from the compressor assembly without dismantling the entire compressor. The flowrate measurement section had an inside diameter of 20.59 inches and an outside diameter of 24.00 inches, resulting in a 1.70 inch passage height. Four specially designed probe holders were manufactured and installed at four locations around the measurement section circumference. The probe holders were designed to hold total-pressure and total-temperature probes

directed radially inward from the outer wall of the annulus. In addition, surface static pressure taps were installed in the measurement section outer casing. The total-pressure and total-temperature probes measured values at 5, 15, 30, 50, 70, 85 and 95 percent immersion depths. A sketch of a typical total-pressure rake probe is shown in Figure 4.14. Before the flowrate measurement section was instrumented and installed, both inner and outer annulus walls were sanded and smoothed with emory cloth.

Because flowrate was such an important parameter in the present study, great care was taken to arrive at a consistent and accurate flow measurement. Appropriate averaging of the total-pressure, static pressure and total-temperature data was necessary due to the high response equipment being used. The collection of pressure and temperature data was accomplished with the data acquisition equipment described in the previous chapter. Through the use of simple compressible flow relations and raw data, the flowrate through the flow measurement section was determined as described below.

The flowpath cross-section of the flow measurement section was divided into seven areas. For each of these areas, the total to static pressure ratio, $\frac{P_t}{P_s}$, was calculated from data. Using the following compressible flow equation,

$$\frac{P_t}{P_s} = \left(1 + \frac{k-1}{2} M^2 \right)^{\frac{k}{k-1}} \quad (4.2)$$

where

P_t = total-pressure

P_s = static pressure

k = ideal gas specific heat ratio

M = Mach number

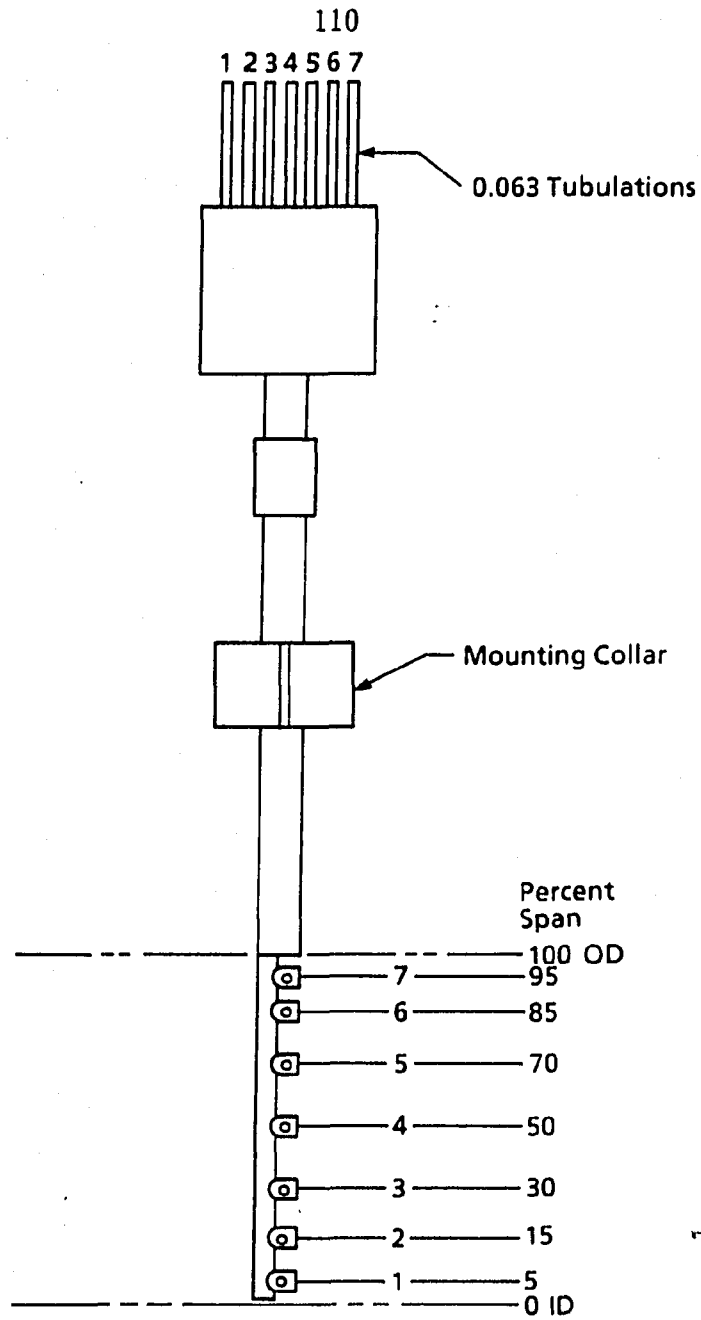


Figure 4.14: Total-pressure probe and measuring locations

We can obtain the following relationship for the Mach number, M ,

$$M = \sqrt{\frac{2}{k-1} \left(\frac{P_t}{P_s} \right)^{\frac{k-1}{k}} - 1} \quad (4.3)$$

With the total to static pressure ratio known, the Mach number can be calculated with Equation (4.3). From the following compressible flow equation,

$$\frac{T_t}{T} = 1 + \frac{k-1}{2} M^2 \quad (4.4)$$

where

T_t = total-temperature

T = static temperature

the static temperature, T , can be evaluated with

$$T = \frac{T_t}{1 + \frac{k-1}{2} M^2} \quad (4.5)$$

The velocity, V , of the air can be calculated using the definition of Mach number,

$$V = M\sqrt{kRT} \quad (4.6)$$

where

V = absolute fluid velocity

R = molecular weight

The flowrate, \dot{m} , can be calculated using the following equation

$$\dot{m} = \rho AV \quad (4.7)$$

and the ideal gas relation

$$P = \rho RT \quad (4.8)$$

Then the flowrate is given by

$$\dot{m} = \frac{PVA}{RT} \quad (4.9)$$

Using the above stated equations, the flowrates for each of the seven areas and for data from each of the four circumferential locations were evaluated. The final overall flowrate was calculated by averaging the four different circumferential position flowrates for each of the seven different flow passage areas.

The data acquisition program was written to scan total-pressures, static pressures and total-temperatures five times and average them before calculating the individual passage flowrates. The program calculated the total compressor flowrate every minute. To arrive at a final measurement for the flowrate, the results of five individual mass flowrate runs were averaged.

Having obtained the mass flowrate, the equation for inlet corrected mass flow is given by

$$\frac{\dot{m} \sqrt{\theta_{t,inlet}}}{\delta_{t,inlet}} \quad (4.10)$$

where

\dot{m} = mass flowrate

$\theta_t = \frac{\text{total temperature at compressor inlet}}{\text{sea level standard temperature}}$

$\delta_t = \frac{\text{total pressure at compressor inlet}}{\text{sea level standard pressure}}$

The quantities θ_t and δ_t were calculated by using measured values of total temperature and pressure at the compressor inlet. This was accomplished by using a midspan total-temperature and total-pressure probe positioned upstream of the compressor inlet.

4.3.2 Compressor pressure rise ratio

The second overall performance parameter measured on the Pratt & Whitney compressor test rig was compressor total-pressure rise ratio. The compressor total-pressure rise ratio is given by

$$\frac{P_{t,outlet}}{P_{t,inlet}} \quad (4.11)$$

where

$P_{t,outlet}$ = compressor outlet total-pressure

$P_{t,inlet}$ = compressor inlet total-pressure

In addition to this total pressure parameter, the compressor static pressure rise ratio was also evaluated. The method for collecting the data for these ratios is explained briefly in this subsection.

The total-pressure rise across the compressor was measured using two total-pressure probes located at the inlet and exit of the compressor. The probes were total-pressure rakes which measured the total-pressure from 15 percent to 85 percent immersion depths. Five total-pressure measurements at 15, 30, 50, 70 and 85 percent immersion were averaged to arrive at the inlet or exit total-pressure measurement. A Meriam 30 inch column of mercury was used to measure the total-pressure readings. The barometric pressure was measured with a Fisher Scientific Model #0284 barometer.

Compressor static pressure rise was measured with static pressure tap holes located at the inlet and exit of the compressor. The mercury manometer was used to measure the static pressure readings.

4.3.3 Inlet corrected rotational speed

The final overall compressor performance parameter measured on the Pratt & Whitney compressor was inlet corrected rotational speed. The equation for inlet corrected rotational speed is

$$\frac{RPM}{\sqrt{\theta_{t,inlet}}} \quad (4.12)$$

where

RPM = rotor rotational speed

$\theta_{t,inlet} = \frac{\text{total-temperature at compressor inlet}}{\text{sea level standard temperature}}$

This equation indicates that a changing compressor inlet condition will affect the inlet corrected rotational speed. Because ambient air from the outside flowed through the compressor, it was important to closely monitor the inlet total-temperature and make any necessary adjustments in the rotor rotational speed to keep the inlet corrected rotational speed constant. Over the course of a data run, these adjustments had to be made fairly frequently. The total-temperature probe positioned at the compressor inlet was used to monitor the compressor inlet total-temperature. The compressor rotor rotational speed was measured with a tachometer mounted on the compressor drive motor.

4.3.4 Detection of stall in the Pratt & Whitney compressor

The method for detection of stall in the Pratt & Whitney compressor is discussed in this subsection. A careful and systematic approach was used to establish a consistent and accurate representation for operating points on the compressor surge/stall limit line.

Stall tests were performed by slowly reducing the inlet corrected mass flow along a constant inlet corrected rotational speed line. The mass flow reduction was accomplished by moving the cone shaped compressor throttle axially. Each movement of the throttle was indicated by a digital readout located on the compressor control panel. When the compressor operated near stall, measurements were taken for determining the overall compressor performance parameters. These measurements were recorded and the throttle was moved to further reduce the mass flowrate. This process continued until the sound of operation of the compressor changed distinctly because of stall. The measurements of flowrate and total-pressure rise taken just before the compressor became unstable were considered to be for the stall point operating conditions. This process for detecting stall along a constant inlet corrected rotational speed line was repeated four to five times in a data run. The stall tests were also repeated on subsequent days to verify the consistency and repeatability of the results. Data for several constant speed lines were obtained. Because stall point data were consistent throughout a data run and did not vary significantly from run to run or from day to day, it was felt that the error band for these measurements was within the symbol used.

5. ESTIMATION OF REDUCED FREQUENCY AND ROTOR INLET FLOW ANGLE VARIATION FOR PRATT & WHITNEY COMPRESSOR

In the absence of detailed flow measurements (velocity magnitude and flow angle) for the flow entering a rotor row, an estimate of the reduced frequency at stall, K_{stall} , and an estimate of the rotor inlet flow angle variation must be made. For a given number upstream stationary blade of setting angle variation cycles per rotor revolution, n , and a given amplitude of setting angle variation, $\Delta\phi$, these estimates are required to choose baseline compressor modifications which may show benefit in terms of stall margin improvement. A thorough analysis of this estimation process for the two-stage axial-flow fan and the three-stage axial-flow compressor was presented in reference [12]. The estimation process for the Pratt & Whitney, intermediate-speed, three-stage, axial-flow compressor for each of the six inlet corrected rotational speeds tested is outlined in detail below.

Flow conditions at the exit of the inlet guide vane (IGV) row give the magnitude of the absolute velocity approaching the rotor. This velocity is necessary to calculate the fluid relative velocity at the rotor inlet used in estimating the reduced frequency at stall, K_{stall} . The technique for calculating the reduced frequency involves using global flow parameters, simple blade row geometry, and a well accepted correlation

of blade deviation angle to arrive at a reasonable estimate of the reduced frequency at stall. The steps used in calculating the reduced frequency at stall for the Pratt & Whitney compressor are summarized below:

1. Determine the midspan average axial velocity at stall using the mass flowrate at stall.
2. Estimate the midspan flow deviation angle behind the inlet guide vane (IGV) row.
3. Draw velocity triangles at midspan using simple blade row geometries.
4. Calculate the magnitude of the midspan fluid relative velocity at rotor inlet.
5. Use Equation (3.5) to calculate K_{stall} .

The material in references [12] and [14] suggests that the magnitude of the rotor inlet flow angle variation may be significantly different from the magnitude of the blade setting angle variation prescribed for the stationary row upstream of the rotor. An estimate of this difference is necessary to completely describe the effect of the inlet guide vane setting angle variation. A detailed analysis of the first stage rotor inlet flow angle variation for the Pratt & Whitney compressor is described in the following sections. A portion of the analysis for the three types of inlet guide vane row blade setting angle patterns used in the low-speed, three-stage, axial-flow compressor taken from reference [12] is also summarized. Those three inlet guide vane row setting angle patterns were sinusoidal (Equation 3.1), rectified sine-wave (Equation 3.2) and asymmetric (Equation 3.3) variations.

The following two sections outline the procedure for calculating the reduced frequency at stall, K_{stall} , and the extent of rotor inlet flow angle variation for the Pratt & Whitney compressor.

5.1 Calculation of Reduced Frequency at Stall, K_{stall} , for the Pratt & Whitney Compressor

The estimation of the reduced frequency at stall, K_{stall} , for the Pratt & Whitney compressor involved an evaluation of the stalling mass flowrate. Performance tests were conducted at each of the six inlet corrected rotational speeds, namely, 50, 60, 70, 80, 90 and 100 percent of design speed. Repetition of tests at the stall condition for each of these speeds resulted in the stall point overall mass flowrate conditions. These performance points are the actual stall/surge point limits shown in Figure 6.1. Using the following equation, the axial velocity at the stall condition for each speed was calculated.

$$\dot{m} = \rho_{inlet} A_{inlet} V_{inlet} \quad (5.1)$$

where

\dot{m} = compressor stalling mass flowrate

ρ_{inlet} = fluid density at compressor inlet

A_{inlet} = annulus area at compressor inlet

V_{inlet} = axial velocity at compressor inlet

In Table 5.1 are summarized values of the stalling mass flowrate and the axial velocity at stall for each of the six inlet corrected rotational speeds.

Before the blade velocity diagrams can be constructed, a reasonable estimate of the inlet flow angle involved must be made. This estimate is made by using simple blade row geometry and a correlation for blade deviation angle given by Carter [15]. Summarized below are some important inlet guide vane midspan blade row angles

Table 5.1: Stalling mass flowrates and axial velocity at stall for the baseline compressor configuration

% Design Speed	\dot{m}_{stall} (lb/s)	$V_{x,stall}$ (ft/s)
100	16.45	235.0
90	14.45	206.0
80	12.75	182.0
70	10.50	150.0
60	8.70	124.0
50	6.60	94.5

which were used to estimate the fluid turning angle and the blade deviation angle for the Pratt & Whitney research compressor.

$$\kappa_1 = \text{blade inlet metal angle} = 0.0^\circ$$

$$\kappa_2 = \text{blade outlet metal angle} = 21.0^\circ$$

$$\theta = \text{blade camber angle} = 21.0^\circ$$

$$i = \text{blade incidence angle} = 0.0^\circ$$

For the accelerating row of inlet guide vanes of the Pratt & Whitney compressor, Carter's correlation is

$$\delta = m\theta(S/c)_{IGV} \quad (5.2)$$

where

$$\delta = \text{deviation angle, (}^\circ\text{)}$$

$$m = \text{factor for accelerating blade rows} = 0.2$$

$$\theta = \text{blade camber angle} = 21.0^\circ$$

$$S = \text{blade spacing} = \frac{\pi D_m}{N} = 0.68 \text{ in.}$$

$$c = \text{blade chord length} = 0.70 \text{ in.}$$

With Equation (5.2) and these quantities, the midspan, inlet guide vane deviation angle was estimated to be

$$\delta \cong 4.0^\circ \quad (5.3)$$

Using this blade deviation angle and the following equations, the rotor inlet flow velocity diagrams at stall for the Pratt & Whitney compressor at each of the six inlet corrected rotational speeds were constructed.

$$\alpha_2 = \beta_2 - \delta \quad (5.4)$$

$$U_{mean} = \frac{\pi r_{mean}(RPM)}{30.0} \quad (5.5)$$

$$V_{2\theta} = V_z \tan \alpha_2 \quad (5.6)$$

$$w_{2\theta} = U_{mean} - V_{2\theta} \quad (5.7)$$

$$w_2 = \sqrt{w_{2\theta}^2 + V_z^2} \quad (5.8)$$

$$\beta_2 = \arctan \left(\frac{w_{2\theta}}{V_z} \right) \quad (5.9)$$

These calculations are all based on the mean radius of the research compressor, which is calculated as

$$r_m = \frac{1}{2} (r_{tip} + r_{hub}) \quad (5.10)$$

In Table 5.2 are summarized some of the results of the velocity diagram calculations for the Pratt & Whitney baseline compressor configuration at stall. Summarized are the absolute tangential velocity, $V_{2\theta}$, the mean blade velocity, U_{mean} , the relative tangential velocity, $w_{2\theta}$, the relative velocity, w_2 and the relative flow angle, β_2 .

In Figures 5.1 through 5.6 are illustrated the first stage rotor inlet flow velocity triangles for the Pratt & Whitney compressor at the stall point for each of the inlet

Table 5.2: Velocity diagram calculations for the baseline stalling condition

% Design Speed	$V_{2,\theta}$ (ft/s)	U_{mean} (ft/s)	$w_{2\theta}$ (ft/s)	w_2 (ft/s)	β_2 (°)
100	71.8	505.9	434.1	493.6	61.6
90	63.0	455.3	392.3	443.1	62.3
80	55.6	404.7	349.1	393.7	62.5
70	45.9	354.1	308.2	342.8	64.0
60	37.9	303.5	265.6	293.1	65.0
50	28.9	252.9	224.0	243.1	67.1

corrected rotational speeds, namely, 50, 60, 70, 80, 90 and 100 percent design speeds.

Figures 5.1 through 5.6 are drawn to scale with unit of velocities given in ft/s.

From Table 5.2 values of the rotor relative velocity, w_2 , the estimated reduced frequency at stall, K_{stall} , was calculated from Equation (3.5), with $V = w_2 =$ representative midspan fluid relative velocity at rotor inlet, or

$$K = \frac{\pi f c}{V} \quad (5.11)$$

where

K = reduced frequency

f = frequency of periodic disturbance, $f = \frac{n(RPM)}{60.0}$, 1/sec

c = rotor blade chord length, in.

$V = w_2$ = fluid relative velocity at rotor inlet, ft/s

In Table 5.3 is shown the reduced frequency estimates at the stall condition, K_{stall} , for the six different inlet corrected rotational speeds as a function of n , the number of setting angle variation cycles per rotor revolution. An appropriate range of values for n was determined in a earlier study (references [12] and [14]). Values

Table 5.3: Reduced frequency at stall, K_{stall} , for the Pratt & Whitney three-stage axial-flow compressor

Percent Speed	Reduced frequency at Stall, K_{stall}
100	$0.094n$
90	$0.094n$
80	$0.094n$
70	$0.095n$
60	$0.095n$
50	$0.096n$

for K_{stall} considered to have likelihood of benefit were in the range from 0.19 to 0.20. Therefore, a 2/rev variation ($n = 2$) in setting angle was considered appropriate for the Pratt & Whitney compressor.

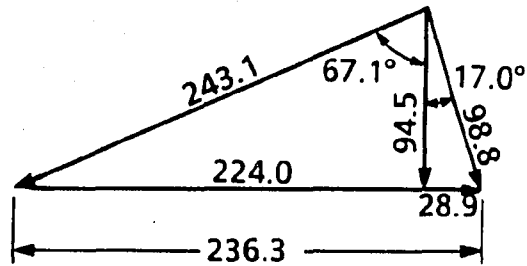


Figure 5.1: Pratt & Whitney blade velocity diagram at stall for 50 percent speed

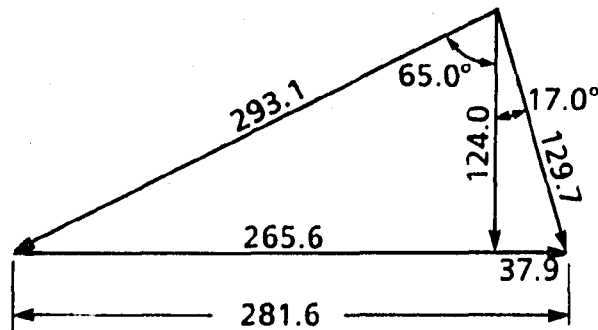


Figure 5.2: Pratt & Whitney blade velocity diagram at stall for 60 percent speed

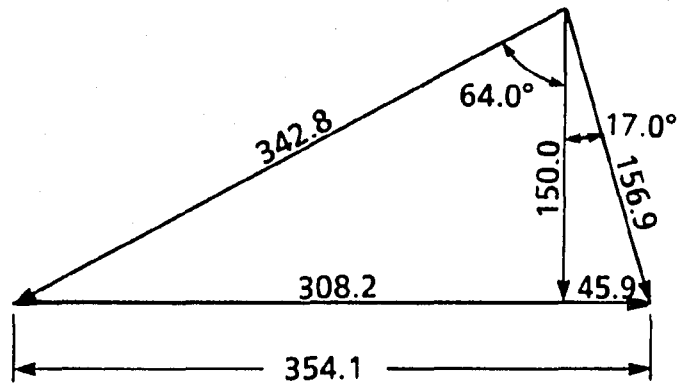


Figure 5.3: Pratt & Whitney blade velocity diagram at stall for 70 percent speed

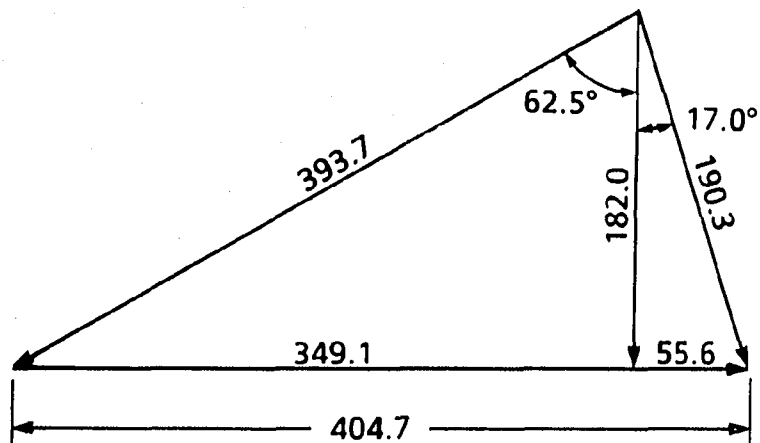


Figure 5.4: Pratt & Whitney blade velocity diagram at stall for 80 percent speed

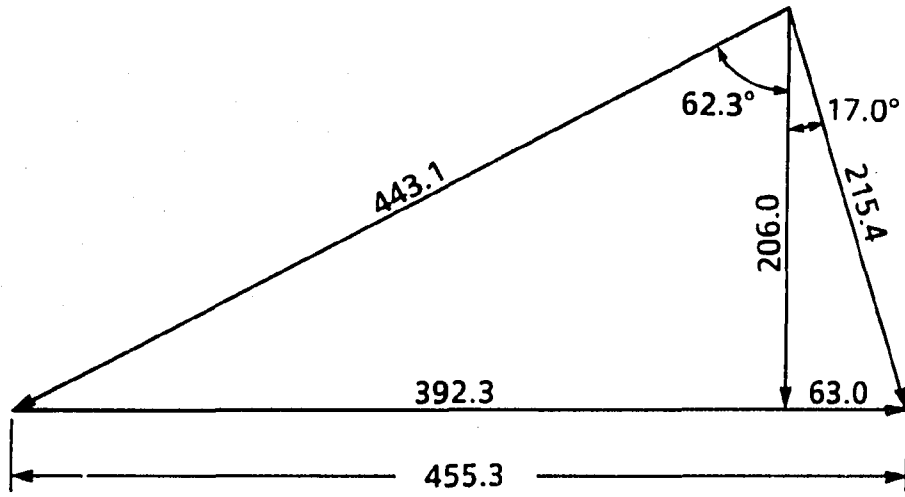


Figure 5.5: Pratt & Whitney blade velocity diagram at stall for 90 percent speed

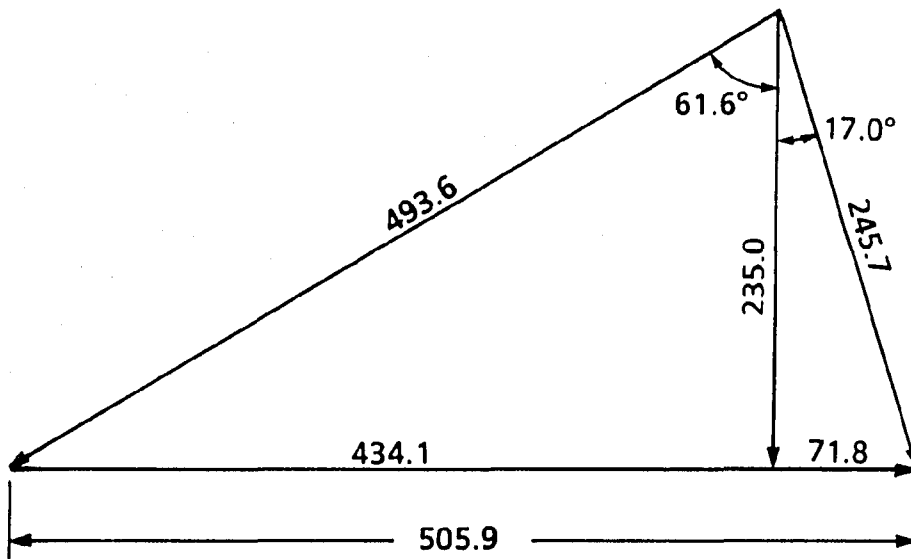


Figure 5.6: Pratt & Whitney blade velocity diagram at stall for 100 percent speed

5.2 Rotor Inlet Flow Angle Analysis for Pratt & Whitney Three-Stage Compressor

The procedure for estimating the rotor inlet flow angle variation caused by the circumferential variation in inlet guide vane setting angles for the Pratt & Whitney compressor is very similar to the one used for the low-speed, three-stage compressor as outlined in reference [12]. This analysis is important because it gives the rotor blade loading and unloading schedule for a given setting angle variation in the inlet guide vane row of the compressor. In the absence of detailed flow measurements, this analysis is an estimate of the actual rotor flow angle variation which occurs. The extent of rotor inlet flow angle variation is directly related to dynamic stall studies in that the flowfield for the rotor is made purposely similar to that of an oscillating airfoil.

The complete analysis of rotor inlet flow angle variation for the Pratt & Whitney compressor is presented in this section. Some of the results from the rotor inlet flow angle analysis for the low-speed, three-stage, axial-flow compressor are also summarized. The reason for this is that the rotor inlet flow angle analysis for the low-speed compressor was used to help identify a candidate modified inlet guide vane setting angle variation for the higher-speed compressor. The most productive results observed with the low-speed compressor inlet guide vane setting angle modifications were evaluated to justify a particular inlet guide vane setting angle variation for the intermediate-speed compressor which would show benefits in term of stall margin improvement.

In Figure 5.7 is shown a typical first stage rotor inlet flow velocity diagram for the low-speed, three-stage compressor at the stall point. The important angles

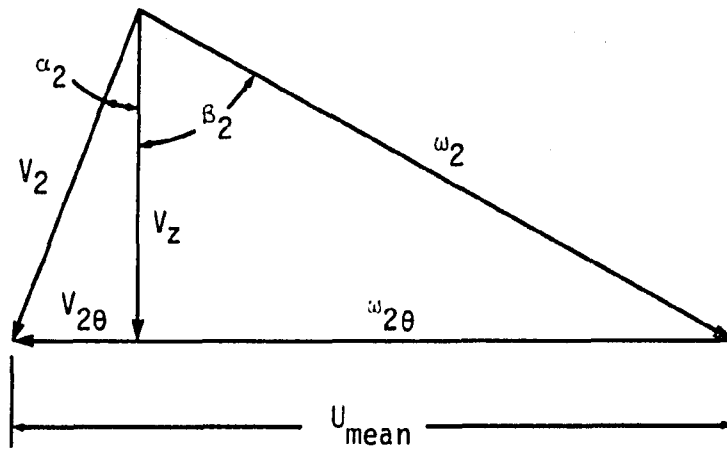


Figure 5.7: Typical first stage rotor inlet flow velocity diagram at the stall point of the three-stage compressor

illustrated in the figure are, α_2 , the flow angle at the inlet guide vane row exit, and β_2 , the relative inlet flow angle perceived by the rotor blade. It is evident that as the inlet guide vane row exit flow angle, α_2 , changes, due to changes in IGV row setting angle, the relative inlet flow angle perceived by the rotor, β_2 , also changes. With the shape of the velocity triangle involved, the change in β_2 is generally smaller than the change in α_2 .

To estimate the change in relative flow angle, β_2 , it is assumed that the change in inlet guide vane row exit flow angle is identical to the blade setting angle increment from baseline, $\Delta\phi_i$. Earlier conclusions from low-speed compressor detailed measurement data suggest that this is a valid assumption. The corresponding change in relative rotor inlet flow angle, β_2 , may then be estimated by constructing a new velocity triangle where the axial velocity remains constant and is the baseline value. The rotor inlet flow velocity diagrams of the baseline compressor (Figures 5.1 through 5.6 and Table 5.2) at the stall point defines the baseline values of, α_2 , the IGV row exit flow angle and β_2 , the relative rotor inlet flow angle. The quantity, $\Delta\beta_2$, represents the difference between the baseline rotor inlet relative flow angle and the modified rotor inlet relative flow angle and is given by the following relation.

$$\Delta\beta_2 = \beta_{2,baseline} - \beta_{2,modified} \quad (5.12)$$

where

$\beta_{2,baseline}$ = rotor inlet relative flow angle for the baseline stalling condition

$\beta_{2,modified}$ = rotor inlet relative flow angle for the modified stalling condition

In Figures 5.8 and 5.9 are illustrated some of the results of the rotor inlet flow angle analysis from the low-speed, three-stage compressor. Shown in Figure 5.8 is an

Table 5.4: Amplitude of blade setting angle variation, $\Delta\phi$, and corresponding rotor inlet flow angle variation for the low-speed, three-stage compressor

Absolute flow angle difference from baseline	$\Delta\beta_2$ ($^\circ$)
+6 $^\circ$	-1.4
+8 $^\circ$	-1.9
+10 $^\circ$	-2.5
-6 $^\circ$	+1.2
-16 $^\circ$	+2.9
-20 $^\circ$	+3.4

asymmetric blade setting angle pattern established by Equation (4.3), where $\Delta\phi_1 = 16^\circ$, $\Delta\phi_2 = 8^\circ$ and $n = 2$ cycles per rotor revolution. This setting angle variation was tested on the low-speed compressor and the resulting estimation for rotor inlet flow angle variation is shown in Figure 5.9.

It is evident that the change in rotor inlet flow angle is significantly less than the change in the inlet guide vane exit flow angle (or setting angle). This is due to the shape of the velocity triangle at the stalling condition. More specifically, a negative change of 16° in the inlet guide vane exit flow angle results in a rotor loading of only 2.9° and a positive change of 8° in IGV row exit flow angle results in a rotor unloading of only 1.9° . In Table 5.4 are summarized additional low-speed rotor inlet flow angle variation results. The table values indicate the absolute flow angle difference from baseline and the estimated change in rotor inlet flow angle, $\Delta\beta_2$, from velocity diagram calculations. These tabulated values suggest again that the change in rotor flow angle is less than the change in IGV exit flow angle and also that a symmetric variation in IGV setting angle may result in a non-symmetric variation in rotor inlet flow angle.

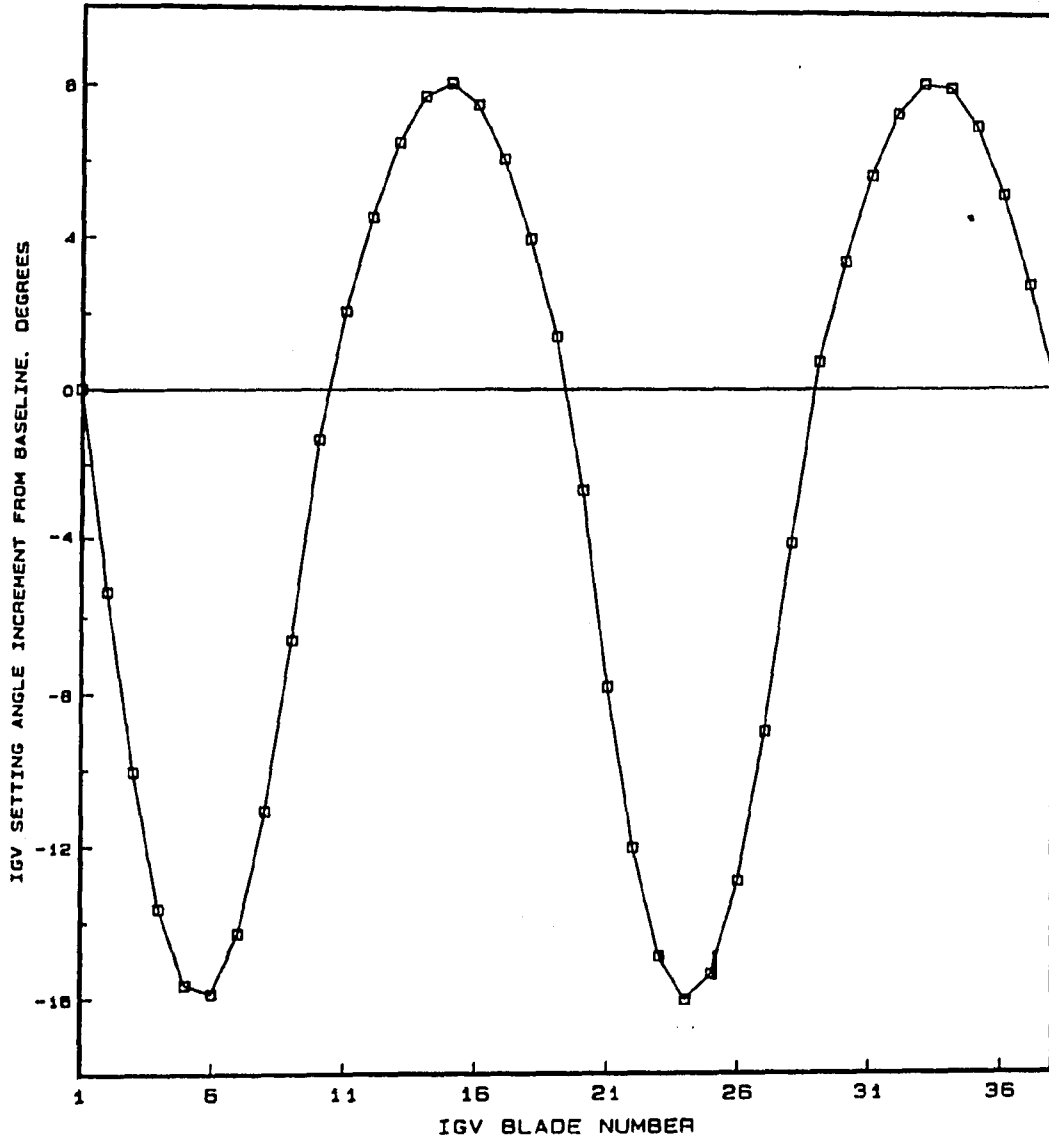


Figure 5.8: IGV row blade setting angle pattern - Equation (3.3), $\Delta\phi_1 = -16^\circ$, $\Delta\phi_2 = -8^\circ$, $n = 2$ cycles/rev

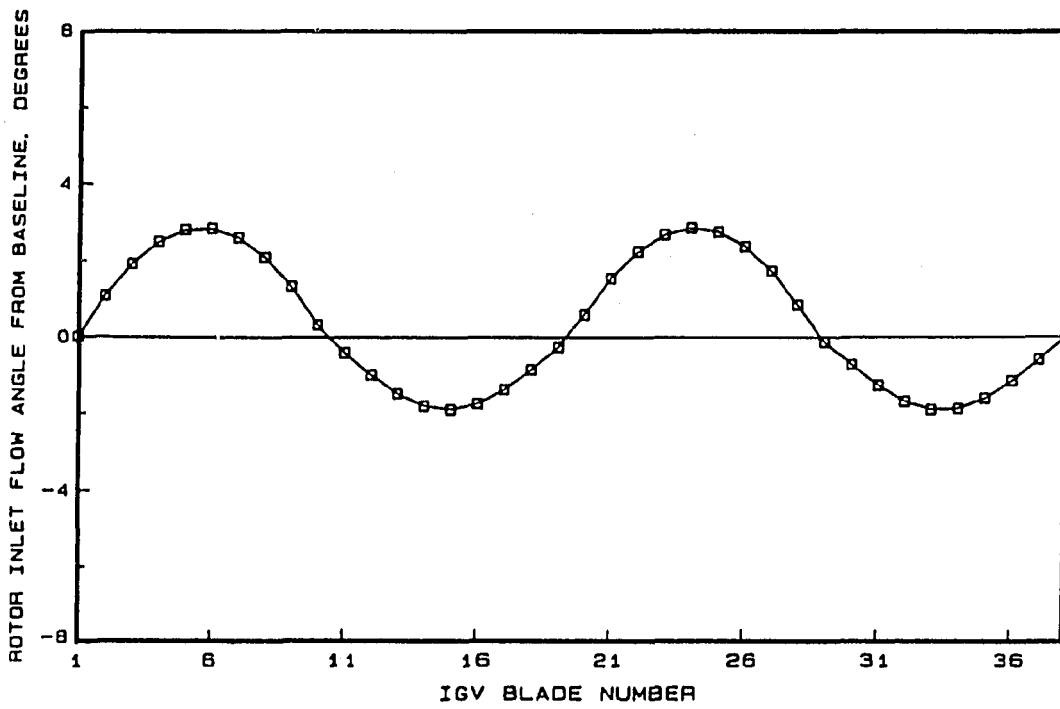


Figure 5.9: Estimated rotor inlet flow angle for Equation (3.3), $\Delta\phi_1 = -16^\circ$, $\Delta\phi_2 = -8^\circ$, $n = 2$ cycles/rev

The results from the rotor inlet flow angle analysis for the low-speed, three-stage compressor guided the selection of the loading schedule for the Pratt & Whitney, intermediate-speed, three-stage compressor. The tests performed with the low-speed, three-stage, axial-flow compressor suggested that the most productive (in terms of stall margin improvement) inlet guide vane setting angle variations were a sinusoidal and an asymmetric variation. More specifically, the sinusoidal variation was one in which the number of setting angle variation cycles per rotor revolution, n , was 2, and the amplitude of setting angle variation, $\Delta\phi$, was 6° . The estimated reduced frequency at stall was 0.19 and the estimated rotor inlet flow angle loading and unloading from baseline was $+1.2^\circ$ and -1.4° , respectively (see Table 5.4). The other productive variation was an asymmetric variation in which the number of setting angle variations, n was 2, and the amplitudes of setting angle variation, $\Delta\phi_1 = 16^\circ$ and $\Delta\phi_2 = 8^\circ$ (see Figure 5.8). The estimated reduced frequency for this variation was 0.19 and the estimated rotor inlet flow angle loading was $+2.9^\circ$ and -1.9° , respectively (see Figure 5.9 and Table 5.4). Because both of these variations resulted in stall margin improvements compared to baseline behavior, the candidate modification to the inlet guide vanes of the Pratt & Whitney, intermediate-speed compressor was chosen to lie somewhere between the two productive variations in terms of rotor inlet flow angle variation. In particular, the rotor inlet flow angle variation for the Pratt & Whitney compressor was $+2.4^\circ$ of rotor loading and -1.5° of rotor unloading. To achieve this desired schedule of rotor loading and unloading, an analysis of rotor inlet flow angle variation for the Pratt & Whitney compressor was performed. Using the analysis outlined in this section, the rotor loading schedule was estimated for any amplitude of setting angle variation. In Table 5.5 are summarized some inlet guide

Table 5.5: Amplitude of blade setting angle variation, $\Delta\phi$, and corresponding rotor inlet flow angle variation the Pratt & Whitney, three-stage compressor

% Design Speed	+10° (°)	+8° (°)	+6° (°)	-16° (°)	-12° (°)	-10° (°)
100	-2.9	-2.3	-1.7	+3.3	+2.6	+2.2
90	-2.8	-2.1	-1.5	+3.2	+2.5	+2.1
80	-2.8	-2.1	-1.6	+3.1	+2.4	+2.1
70	-2.4	-1.8	-1.3	+2.9	+2.3	+1.9
60	-2.3	-1.8	-1.3	+2.6	+2.0	+1.7
50	-1.9	-1.5	-1.0	+2.3	+1.8	+1.5
Ave.	-2.5	-1.9	-1.4	+2.9	+2.3	+1.9

vane row setting angle amplitudes and the resulting rotor loadings or unloadings which they produced.

Table 5.5 suggests that the rotor inlet flow angle magnitude varies with inlet corrected rotational speed. Because of this, an average loading and unloading schedule must be selected so that the desired loading schedule is met. Table 5.5 indicates six different inlet guide vane setting angle amplitudes, namely, +10°, +8°, +6°, -16°, -12° and -10°. The average values of the resulting rotor loadings are also indicated. From this table, a -12° amplitude of IGV setting angle would result in an average loading of +2.3° and a +6° amplitude of IGV setting angle would result in an average unloading of -1.4°. This asymmetric setting angle variation (-12° and +6°) results in the approximate desired rotor loading schedule of +2.4° and -1.5°, respectively.

To summarize the results of the two previous sections, the candidate inlet guide vane setting angle pattern chosen was one involving an asymmetric variation where the number of setting angle variations per rotor revolution was 2, and the amplitudes of setting angle variation, $\Delta\phi_1 = 6^\circ$ and $\Delta\phi_2 = 12^\circ$. The estimated reduced frequency

for this variation was 0.19 and the estimated rotor inlet flow angle loading was $+2.3^\circ$ and -1.4° .

6. PRATT & WHITNEY RESULTS AND DISCUSSIONS

6.1 Pratt and Whitney Baseline and Modified Compressor Performance

The effect of compressibility on the proposed method for improving the stall margin of multistage axial-flow compressors was tested with a Pratt & Whitney, three-stage, intermediate-speed, axial-flow compressor. Overall performance tests were performed on the baseline compressor configuration as well as one modified compressor configuration in which an asymmetric variation in stationary blade setting angle where $\Delta\phi_1 = 12^\circ$, $\Delta\phi_2 = 6^\circ$ and $n = 2$ cycles per rotor revolution was the setting angle schedule. Recall that the modified Pratt & Whitney compressor inlet guide vane setting angle variation was selected from results of beneficial blade setting angle variations in the low-speed, three-stage compressor. Particular attention was focused on the reduced frequency at stall, K_{stall} , and the resulting rotor inlet flow angle variation. In this case, the estimated reduced frequency at stall, K_{stall} , was 0.19 and the rotor inlet flow angle variation maximum and minimum values were $+2.3^\circ$ and -1.4° .

The overall performance parameters for the Pratt & Whitney compressor were corrected mass flow, total-pressure ratio and inlet corrected rotational speed and are given by Equations (4.10), (4.11) and (4.12). The performance tests involved identifying the overall performance characteristics of the compressor at six different

inlet corrected rotational speeds, namely 50, 60, 70, 80, 90 and 100 percent of design speed. Particular attention was focused on measuring the operating condition near stall. Repetitions of tests were performed to accurately and consistently arrive at a good representation of compressor stall point.

In Figure 6.1 is shown the overall performance characteristics for the baseline and modified (-12° and $+6^\circ$, 2/rev) compressor configurations. The data of Figure 6.1 suggest that the asymmetric inlet guide vane setting angle schedule, while modestly beneficial at lower speeds, did not change the compressor stall points at higher speeds. The largest benefit in stall margin occurs for the lowest inlet corrected rotational speed, namely 50 percent design speed. This improvement disappears with increasing rotational speed and at the highest rotational speeds (80, 90 and 100), no difference can be seen between the baseline and modified compressor stall points. Performance data while operating in rotating stall was not collected because of the possibility of damage to the compressor blading. Possible reasons why the improvements in stall margin were less than expected for the Pratt & Whitney compressor will be discussed in the conclusions chapter. Also, recommendations for further research using circumferential blade setting angle variations on high-speed compressors are presented.

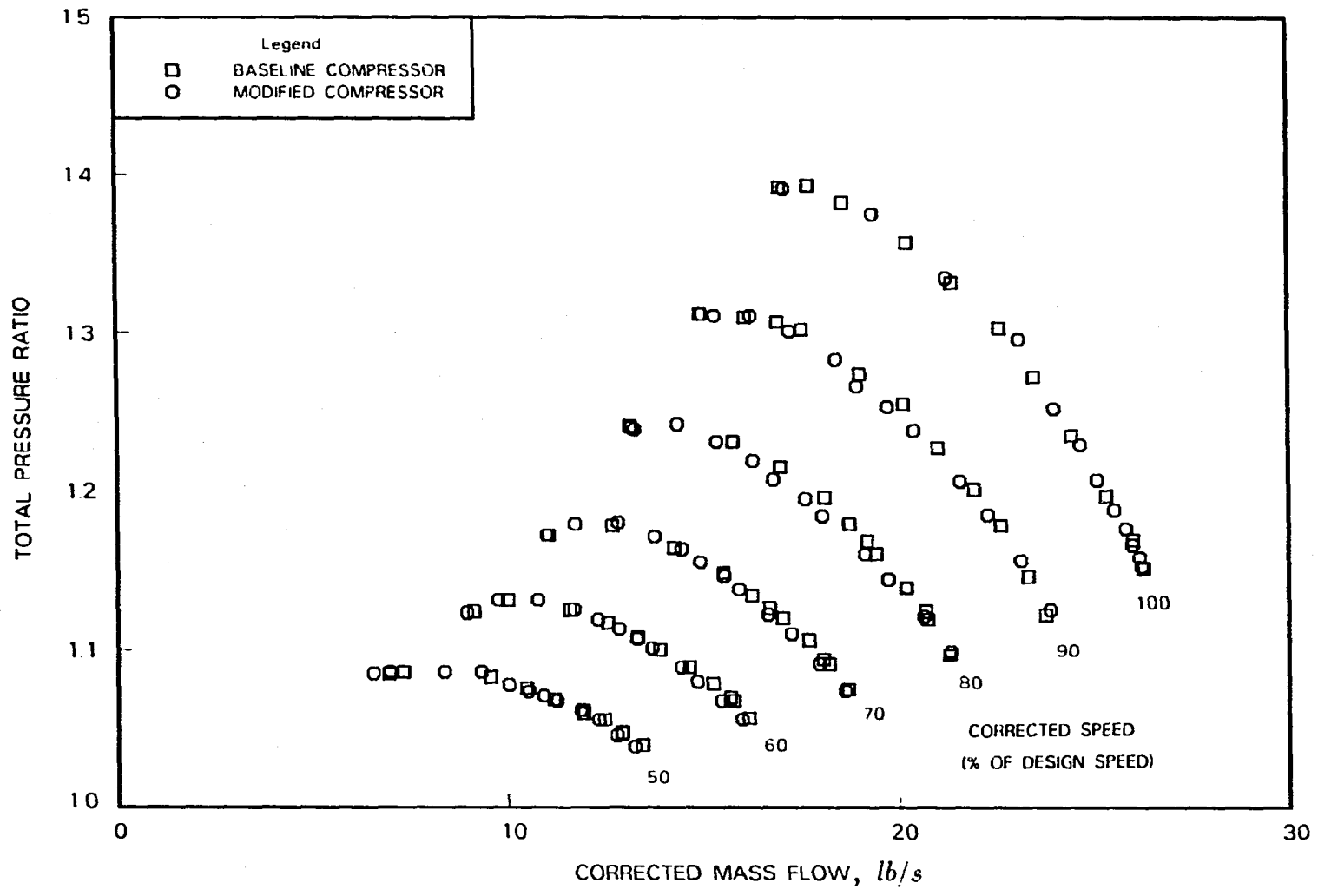


Figure 6.1: Pratt & Whitney baseline versus modified compressor configuration performance

6.1.1 Pratt & Whitney detailed flow measurements

In addition to overall performance data collected on the Pratt & Whitney, intermediate-speed, three-stage, axial-flow compressor, some detailed measurements of the flow at the inlet and exit of the compressor were performed. Detailed measurements were performed for both the baseline compressor as well as the modified compressor in which the inlet guide vanes were set in an asymmetric variation with $\Delta\phi_1 = 12^\circ$ and $\Delta\phi_2 = 6^\circ$ and $K_{stall} = 0.19$. Each compressor configuration was instrumented with total-pressure probe rakes at four circumferential locations around the compressor annulus upstream of the inlet guide vanes and downstream of the compressor exit at the flow measurement section.

These total-pressure and total-temperature measurements were collected at the six different percent inlet corrected rotational speeds of 50, 60, 70, 80, 90 and 100. For each of the different speeds, data were collected at an operating condition very near the actual stall point and at an operating condition closer to design conditions on the compressor characteristic. In Figures 6.2 and 6.3 are shown the detailed measurement operating conditions for the baseline compressor and modified compressor configurations, respectively. The velocity distributions were determined with Equations (4.2) through (4.6) discussed in Chapter 4.

In Figures 6.4 through 6.9 are shown the velocity profiles for the baseline compressor inlet flow for the six different inlet corrected rotational speeds, namely, 50, 60, 70, 80, 90 and 100, respectively. The figures show the velocity profiles near stall and at an operating point further along the operating line. The four different circumferential locations surveyed are shown in the figures by different dashed lines and are indicated in the legend. These data suggest that the inlet flow for the baseline com-

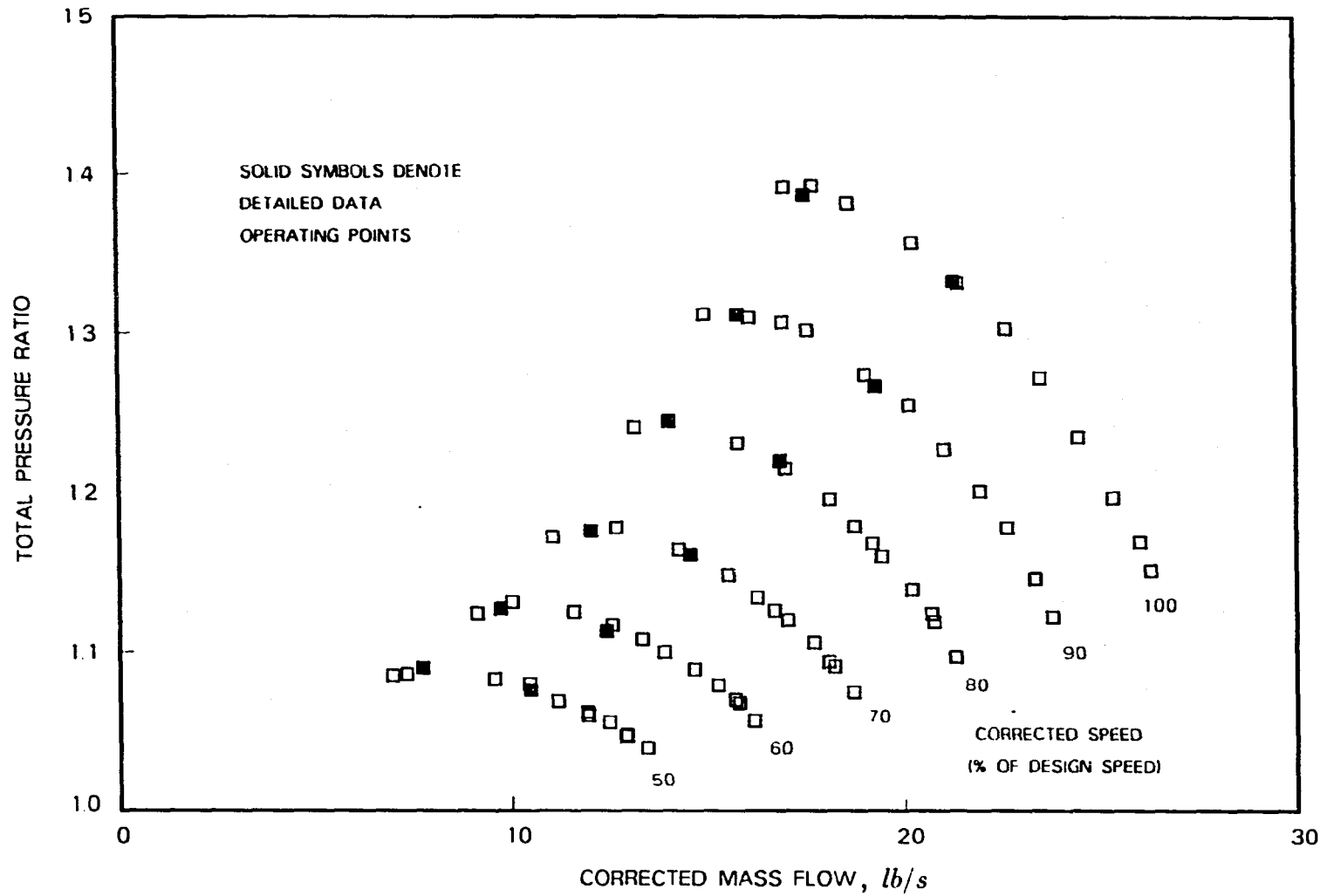


Figure 6.2: Pratt & Whitney detailed measurement operating points for baseline compressor configuration

pressor configuration involves a flat velocity profile and is reasonably symmetrical around the circumference. The data also suggest that as the inlet corrected rotational speed is increased, the end wall regions (especially near the tip) display higher velocity gradients and the flow in these regions is not as circumferentially symmetric as the core flow is.

In Figures 6.10 through 6.15 are shown the velocity profiles for the modified compressor configuration inlet flow for the six different inlet corrected rotational speeds. These data again suggest that the inlet velocity profile is mostly flat and symmetric around the compressor circumference. Again, with increasing inlet corrected rotational speed, the end wall regions exhibit more gradients in velocity especially near the tip. Also noteworthy in Figure 6.15 is the slight bump in the velocity profiles for the 100 percent inlet corrected rotational speed near stall and at the operating point further along the compressor characteristic.

The baseline compressor flowrate section velocity profiles are shown in Figures 6.16 through 6.21 for the six different inlet corrected rotational speeds. It is evident that this flow is not as symmetric around the compressor annulus as the inlet flow is. The reason for this is that the downstream velocity profiles are affected by the position of stationary blades, struts and probes upstream of the measurement section. Blade wakes and wakes from the positioning struts affect the total-pressure distribution downstream causing the variation in velocity profiles. Despite these reasons for the non-symmetry of the velocity profiles, flows corresponding to the operating point near stall and the operating point further along the compressor curve are clearly distinguishable. The data suggest that there may be more symmetry at the operating point further along the compressor characteristic than the operating point near stall.

Also, as the inlet corrected rotational speed increased, the velocity profiles exhibit much more variation.

In Figures 6.22 through 6.27 are shown the velocity profiles in the flowrate measurement section for the modified compressor configuration at six different rotational speeds. These figures are much like those for the baseline compressor flowrate measurement section. The data suggest that the velocity profiles exhibit more variation at higher rotational speed. In fact, the modified compressor velocity profiles in the flowrate measurement section show slightly more variation than did those for the baseline compressor. Perhaps the reason for this is that the effect of repositioning the inlet guide vanes in such an aggressive manner has an effect on the downstream flow conditions as well. Because the variation in setting angle was periodic in a two per rotor revolution, the downstream total-pressure probes each had an upstream flowfield that was different from the others. Due to this non-uniformity in the inlet guide vanes, the compressor was non-uniformly loaded around the compressor annulus and the result is shown in the downstream velocity profiles in the flowrate measurement section.

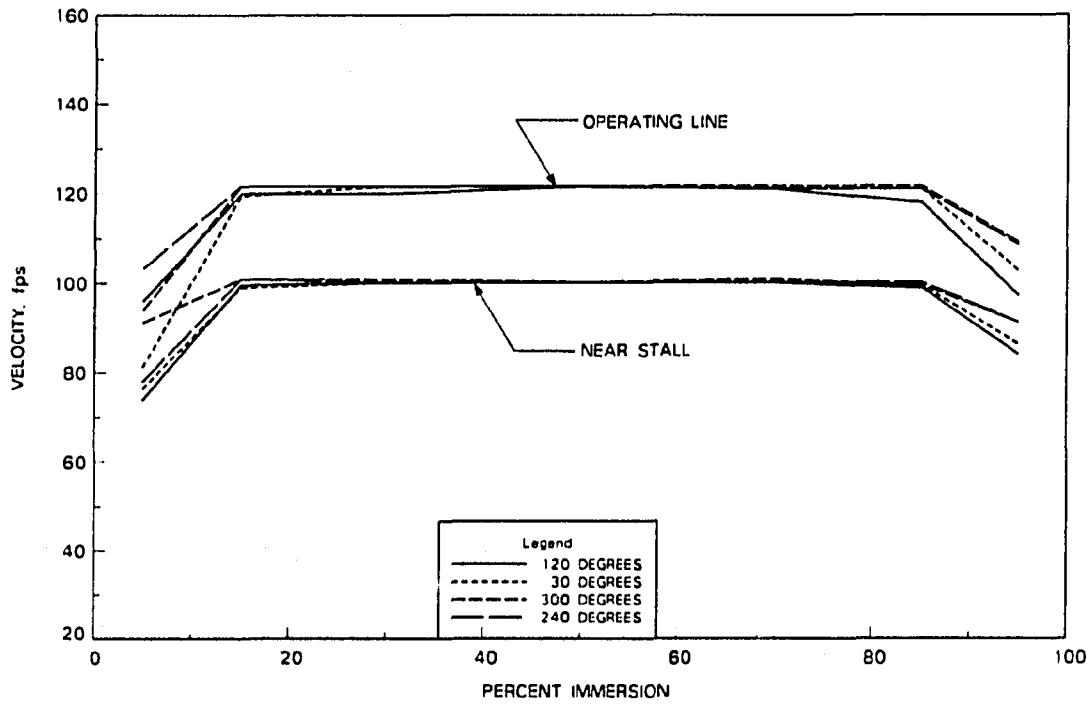


Figure 6.4: Pratt & Whitney detailed flow measurements at inlet, baseline, 50 percent speed

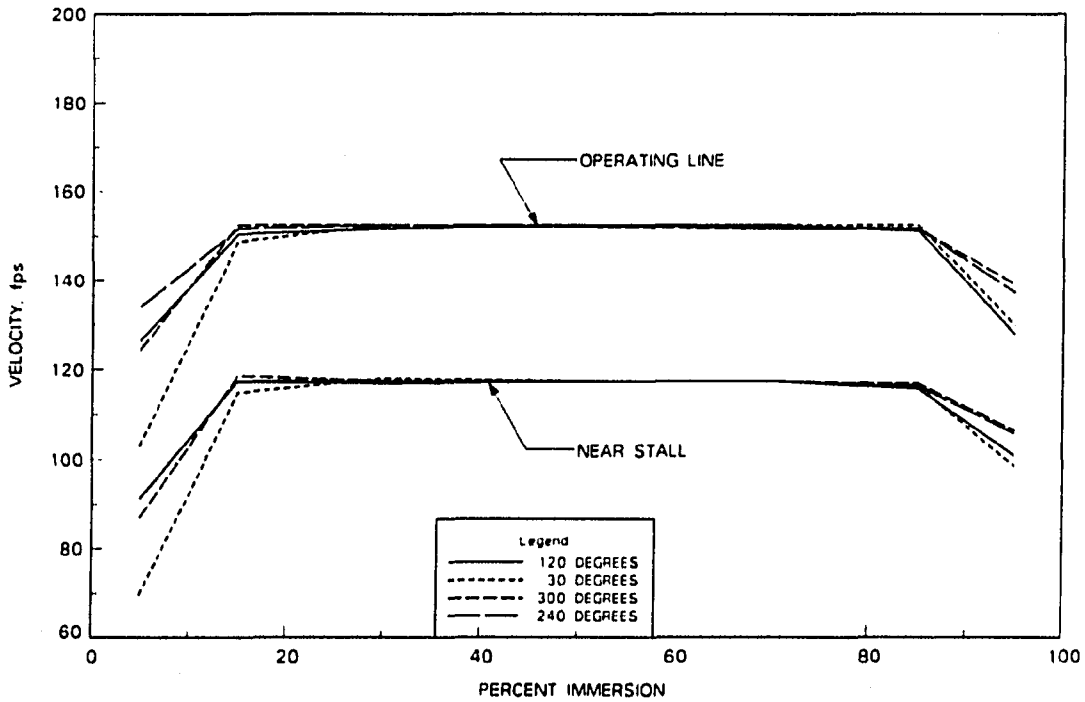


Figure 6.5: Pratt & Whitney detailed flow measurements at inlet, baseline, 60 percent speed

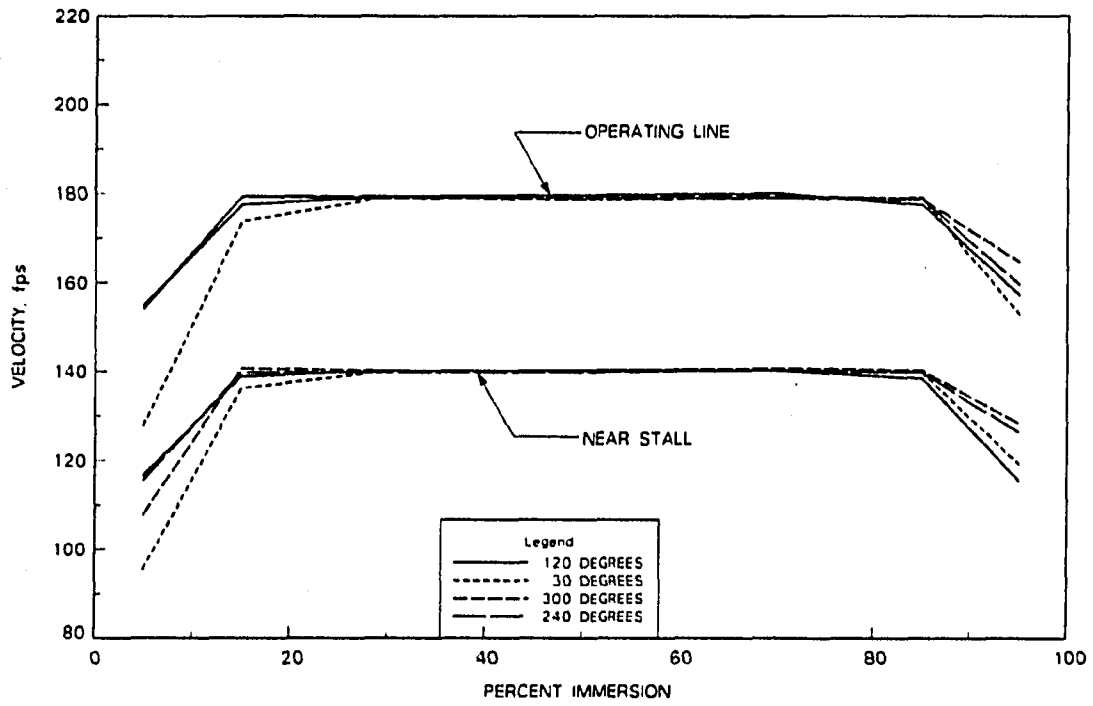


Figure 6.6: Pratt & Whitney detailed flow measurements at inlet, baseline, 70 percent speed

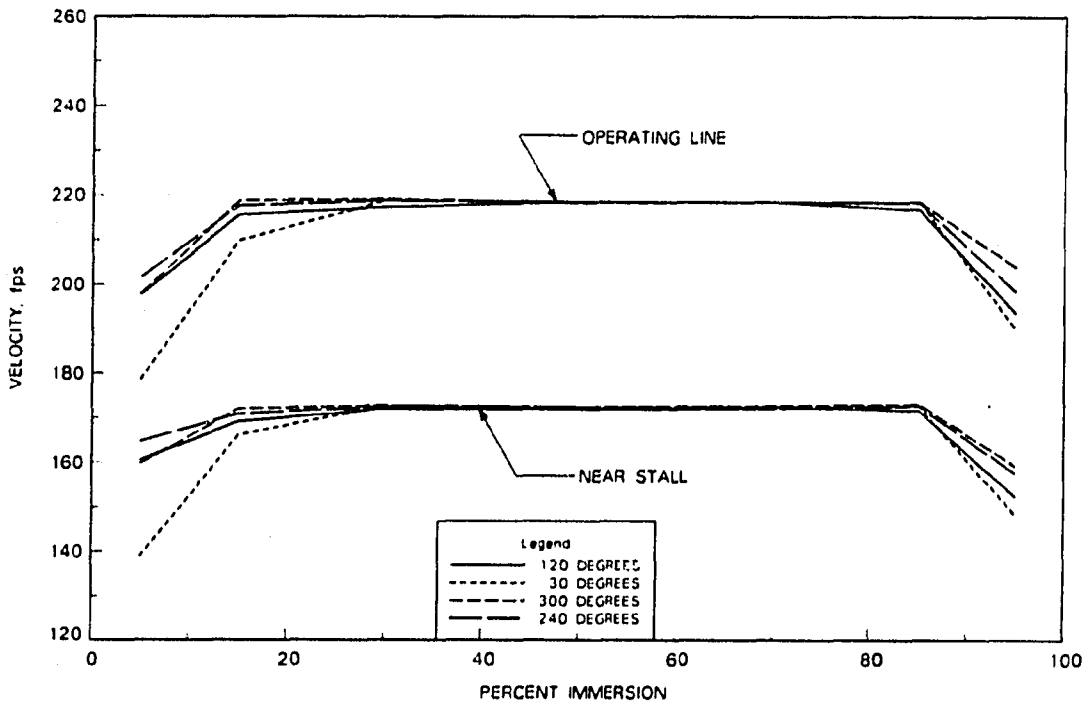


Figure 6.7: Pratt & Whitney detailed flow measurements at inlet, baseline, 80 percent speed

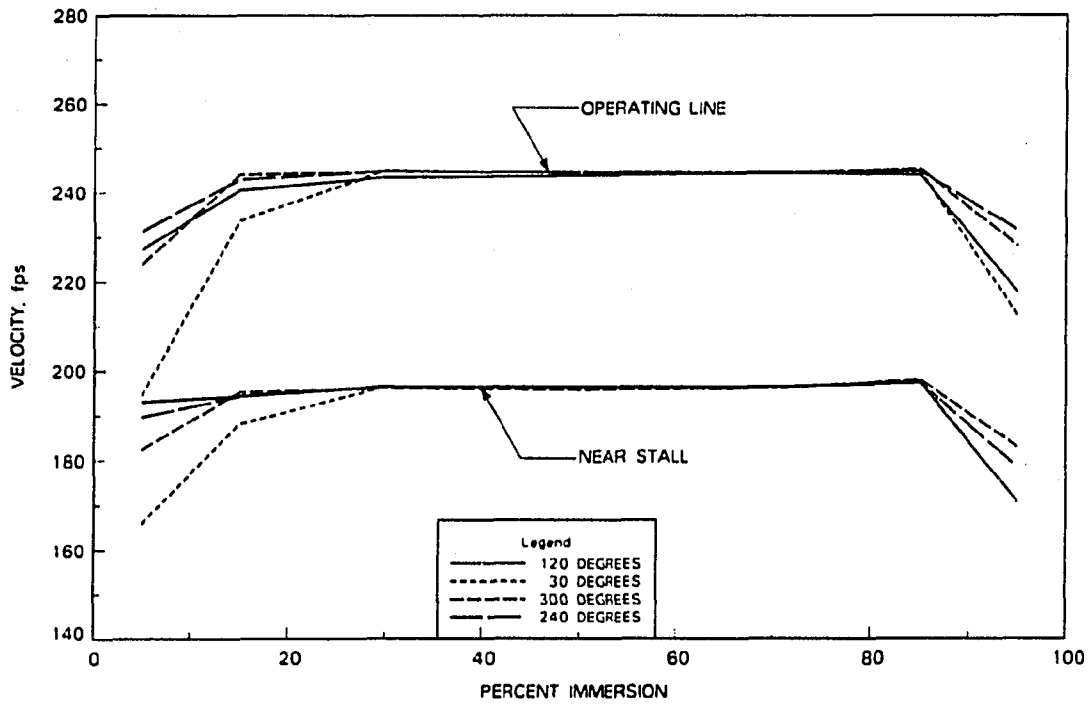


Figure 6.8: Pratt & Whitney detailed flow measurements at inlet, baseline, 90 percent speed

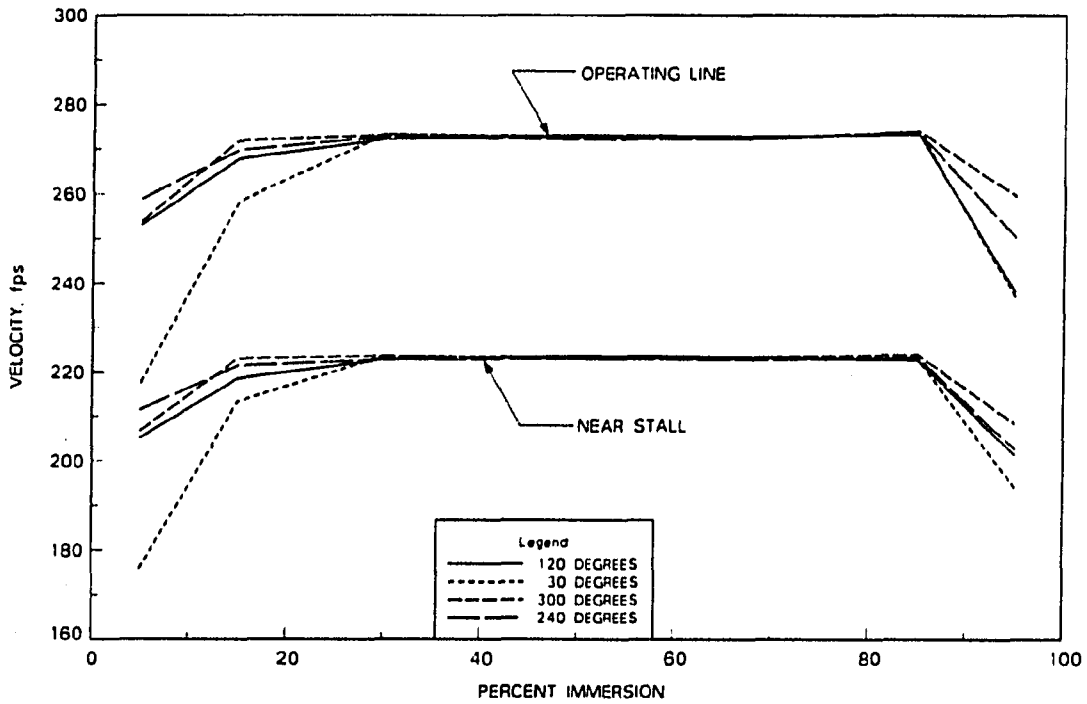


Figure 6.9: Pratt & Whitney detailed flow measurements at inlet, baseline, 100 percent speed

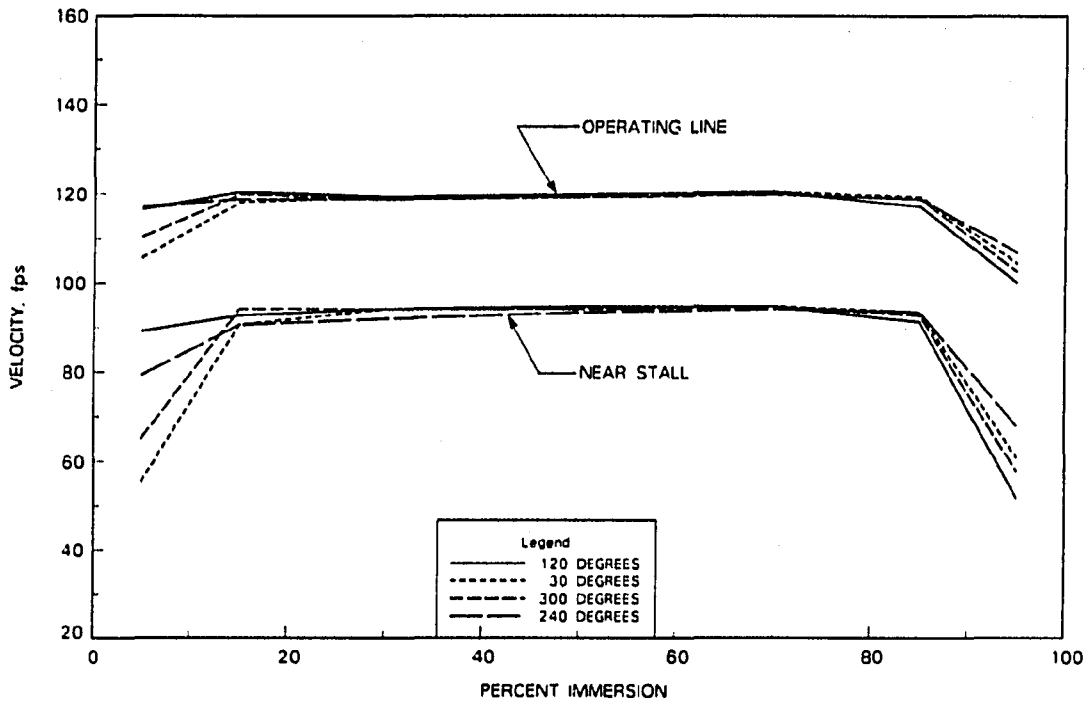


Figure 6.10: Pratt & Whitney detailed flow measurements at inlet, modified, 50 percent speed

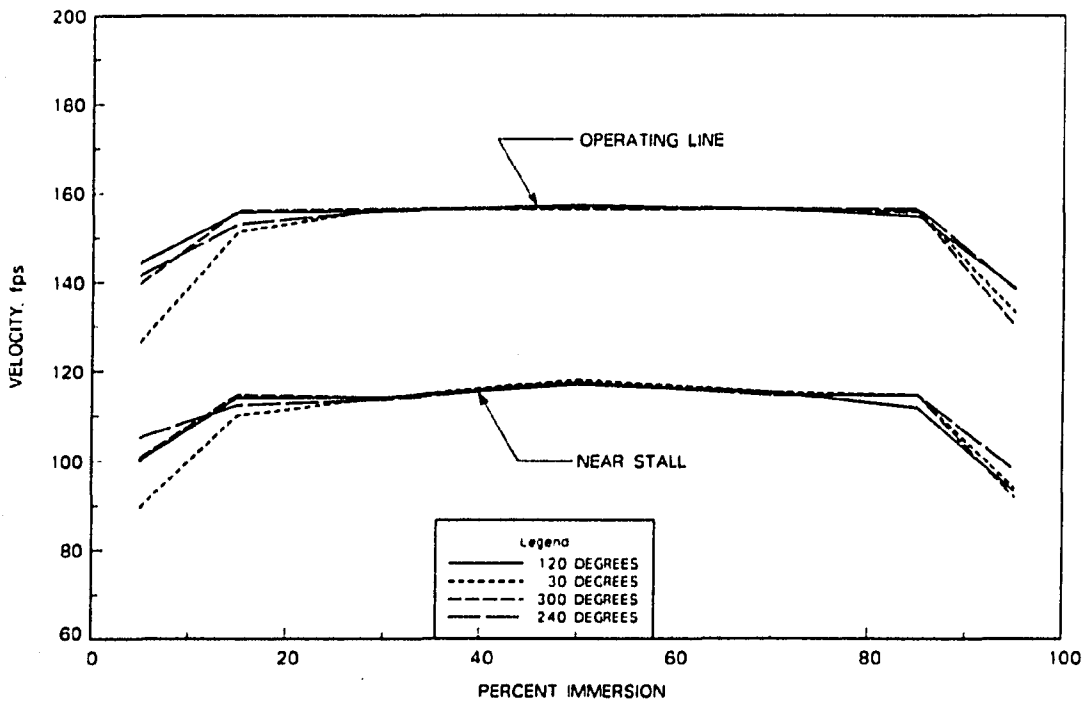


Figure 6.11: Pratt & Whitney detailed flow measurements at inlet, modified, 60 percent speed

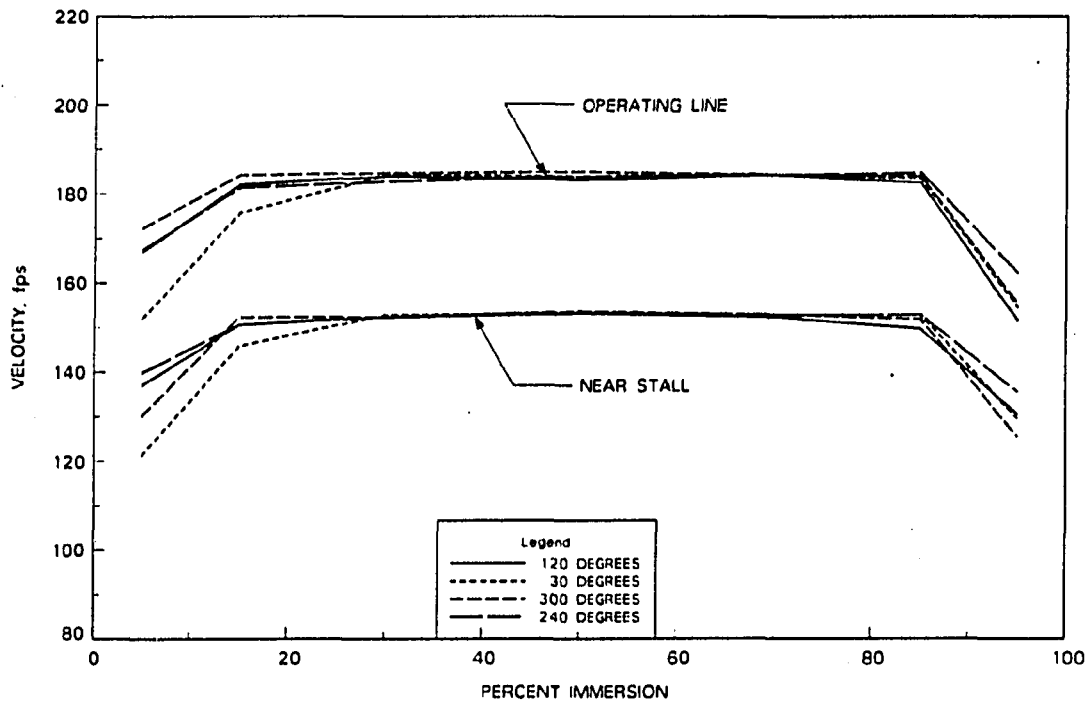


Figure 6.12: Pratt & Whitney detailed flow measurements at inlet, modified, 70 percent speed

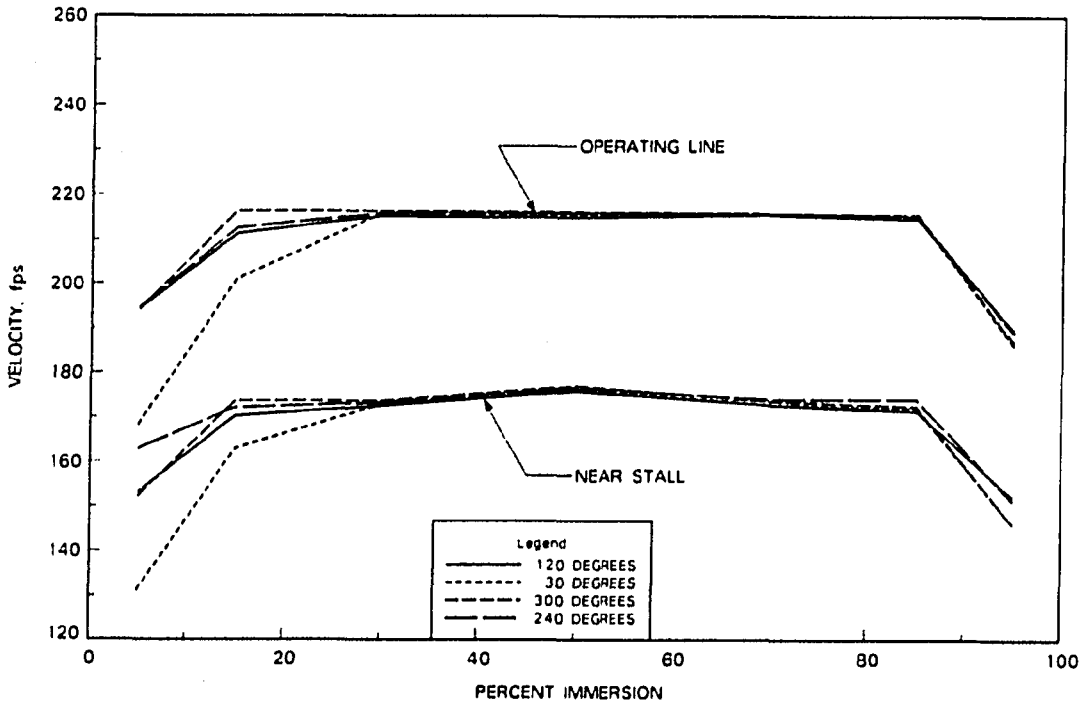


Figure 6.13: Pratt & Whitney detailed flow measurements at inlet, modified, 80 percent speed

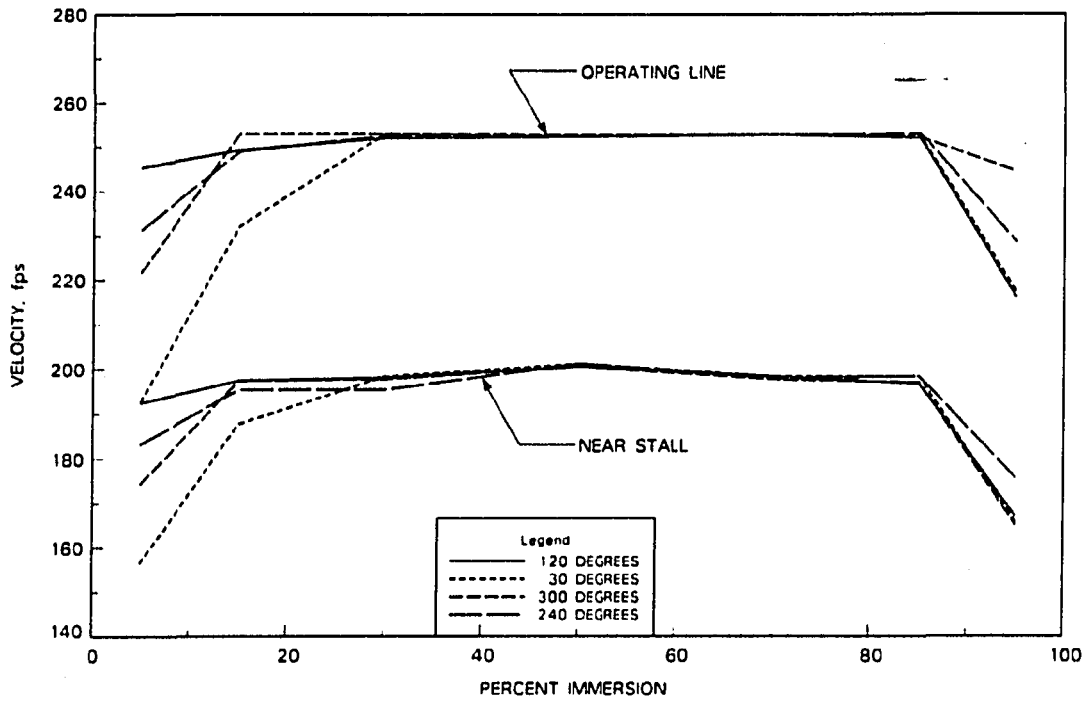


Figure 6.14: Pratt & Whitney detailed flow measurements at inlet, modified, 90 percent speed

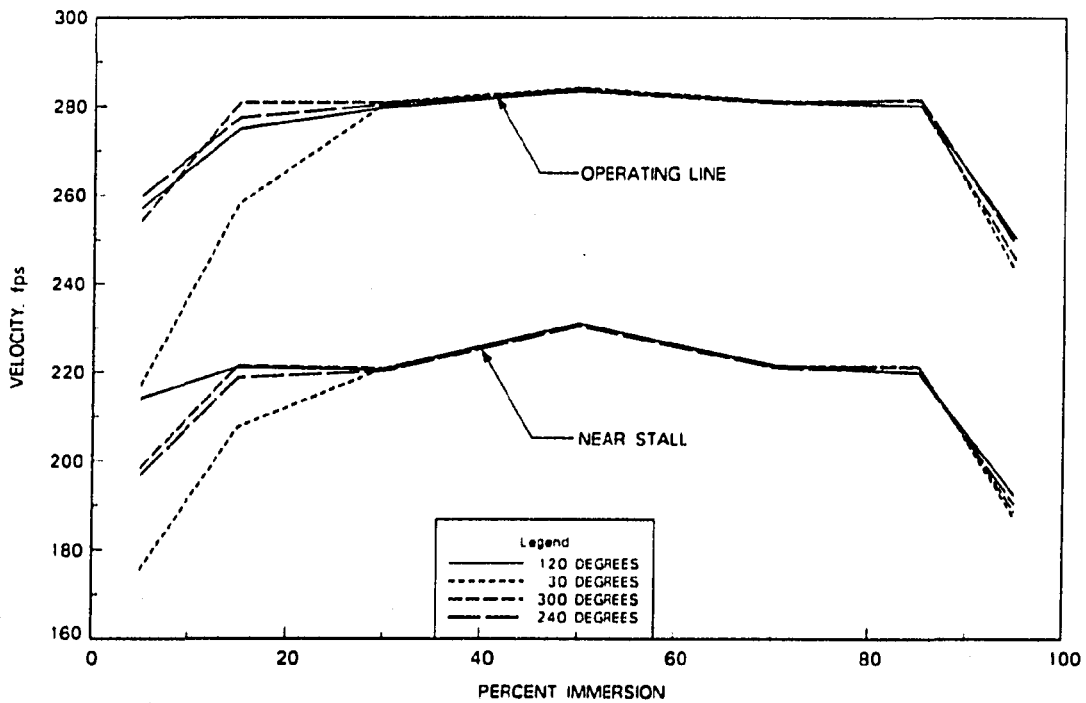


Figure 6.15: Pratt & Whitney detailed flow measurements at inlet, modified, 100 percent speed

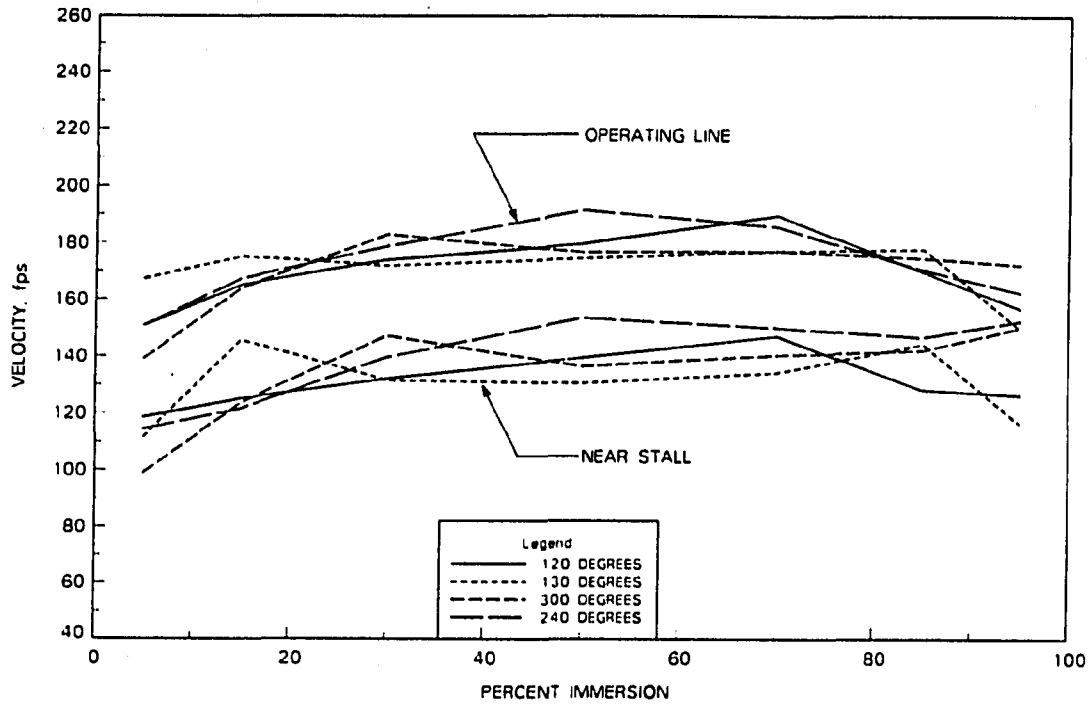


Figure 6.16: Pratt & Whitney detailed flow measurements at exit, baseline, 50 percent speed

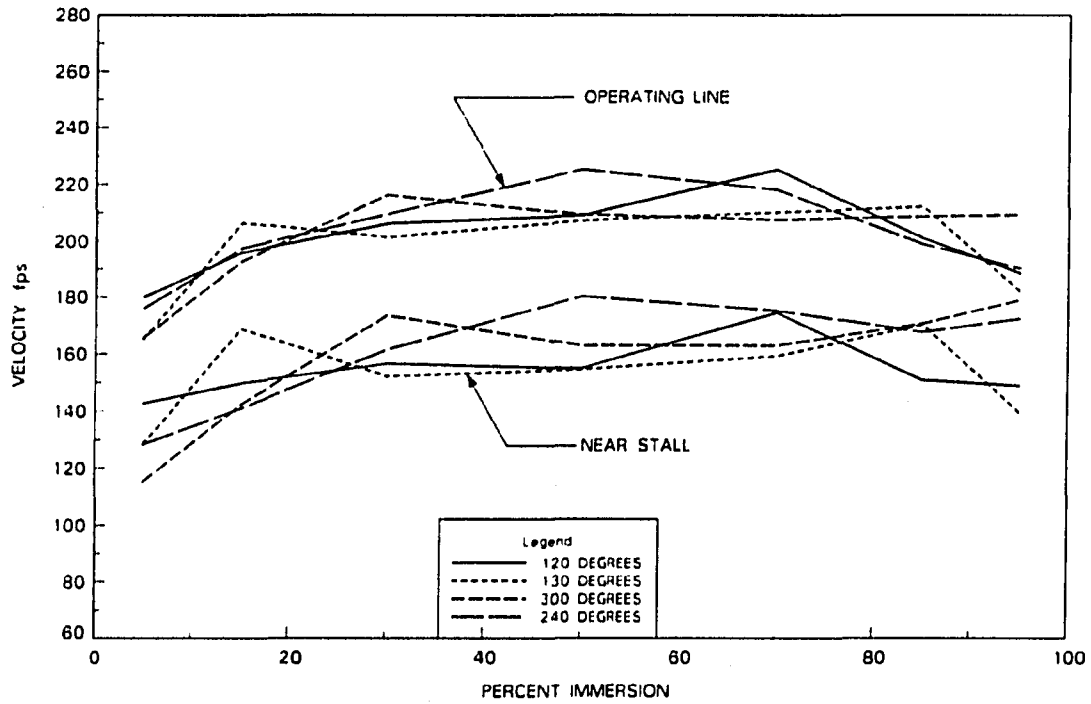


Figure 6.17: Pratt & Whitney detailed flow measurements at exit, baseline, 60 percent speed

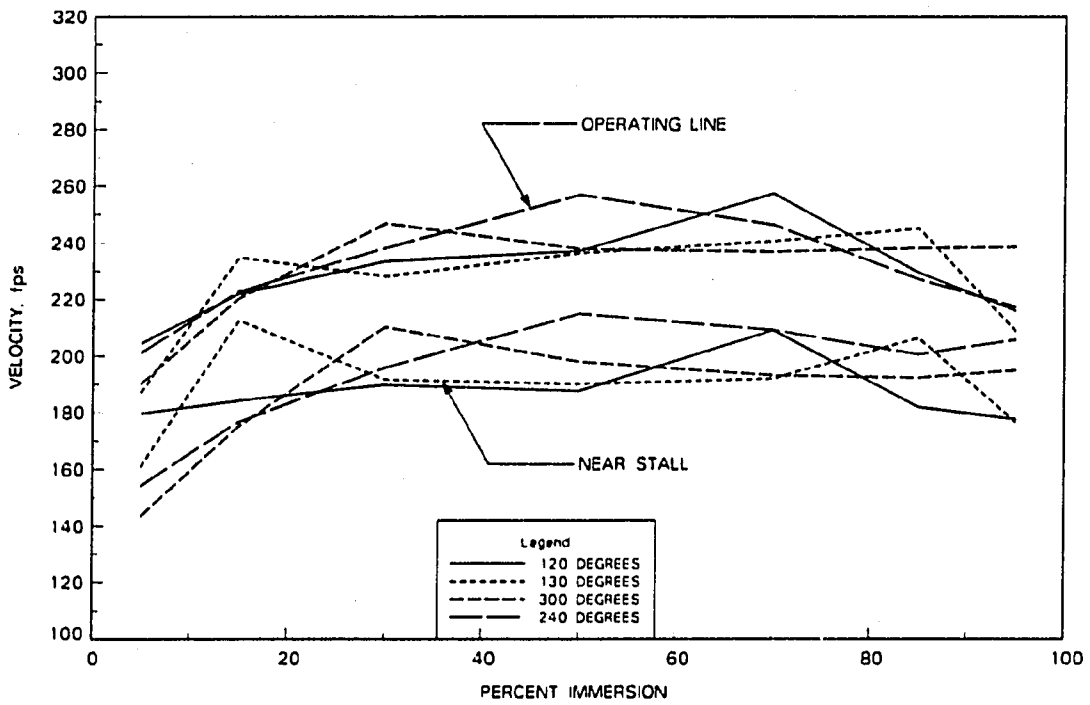


Figure 6.18: Pratt & Whitney detailed flow measurements at exit, baseline, 70 percent speed

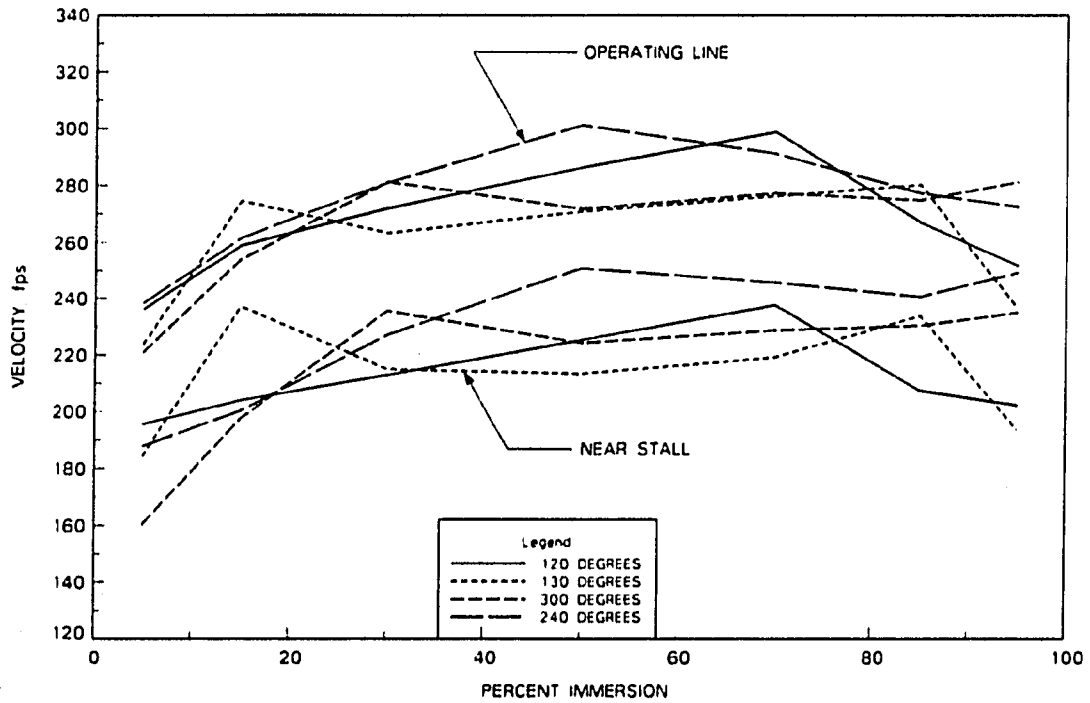


Figure 6.19: Pratt & Whitney detailed flow measurements at exit, baseline, 80 percent speed

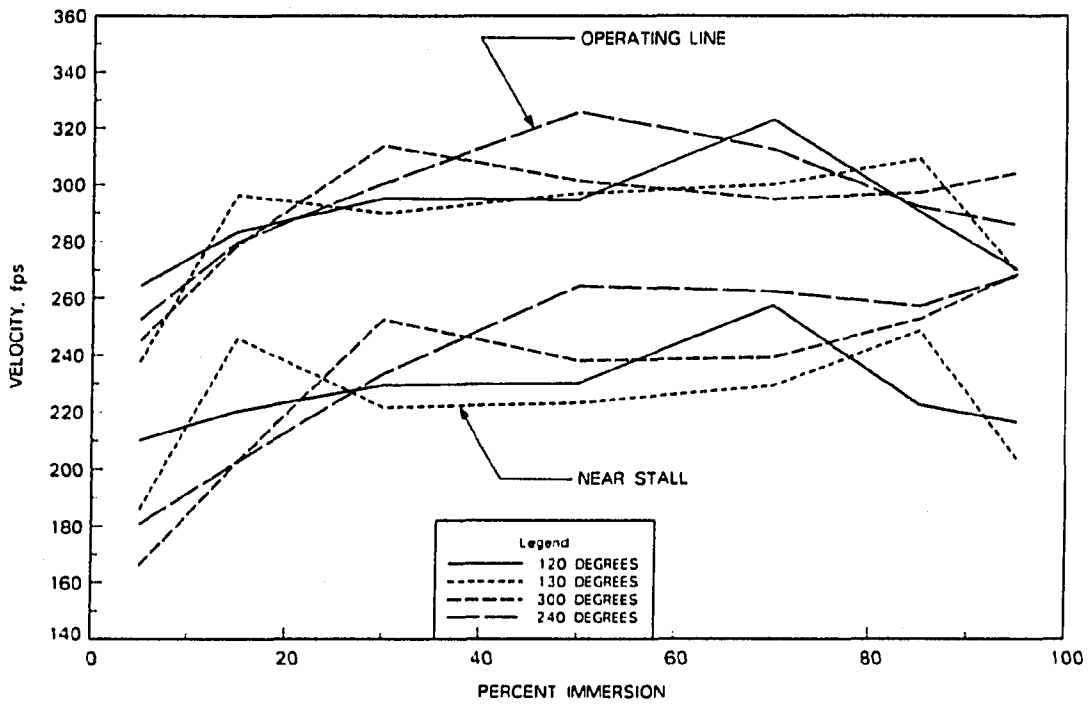


Figure 6.20: Pratt & Whitney detailed flow measurements at exit, baseline, 90 percent speed

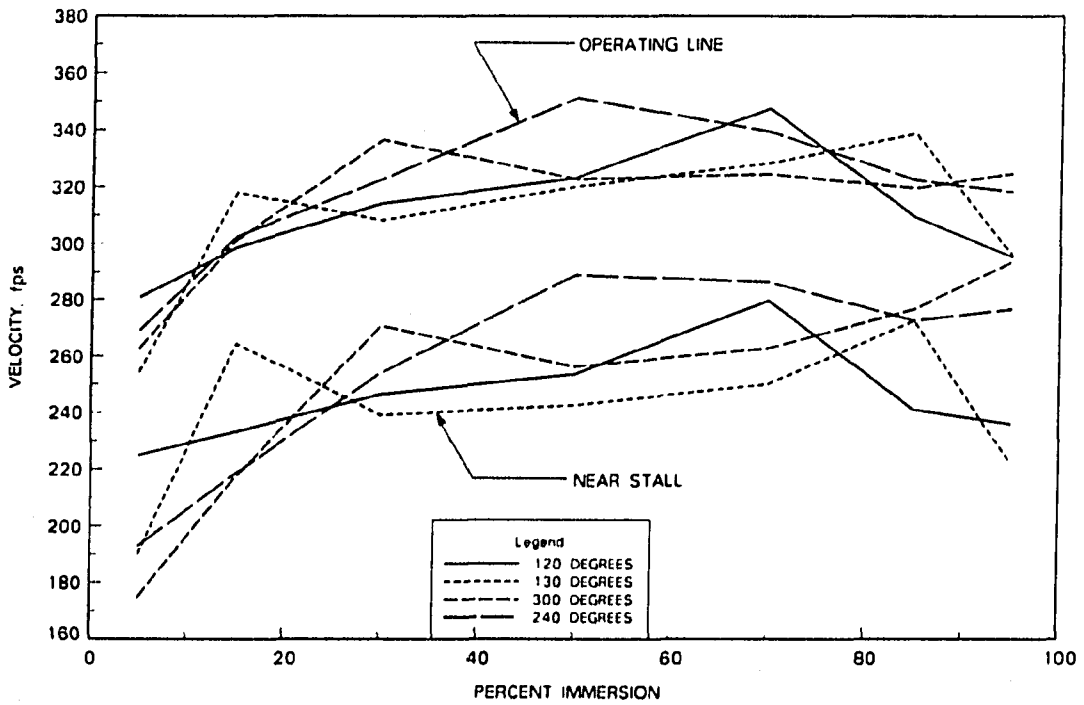


Figure 6.21: Pratt & Whitney detailed flow measurements at exit, baseline, 100 percent speed

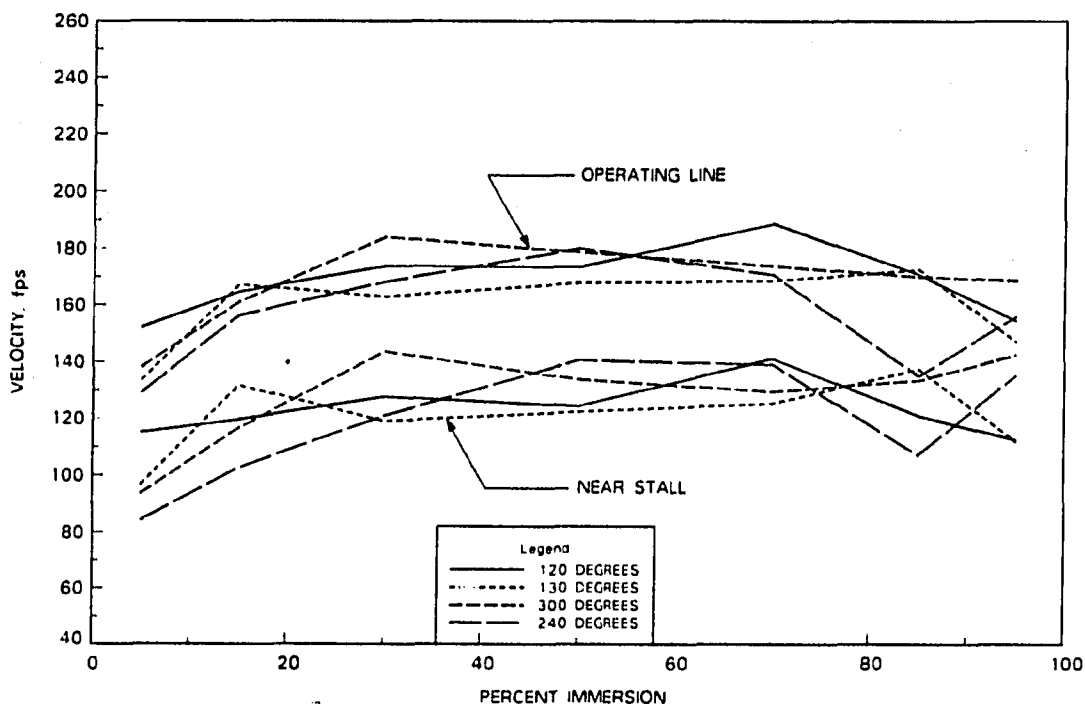


Figure 6.22: Pratt & Whitney detailed flow measurements at exit, modified, 50 percent speed

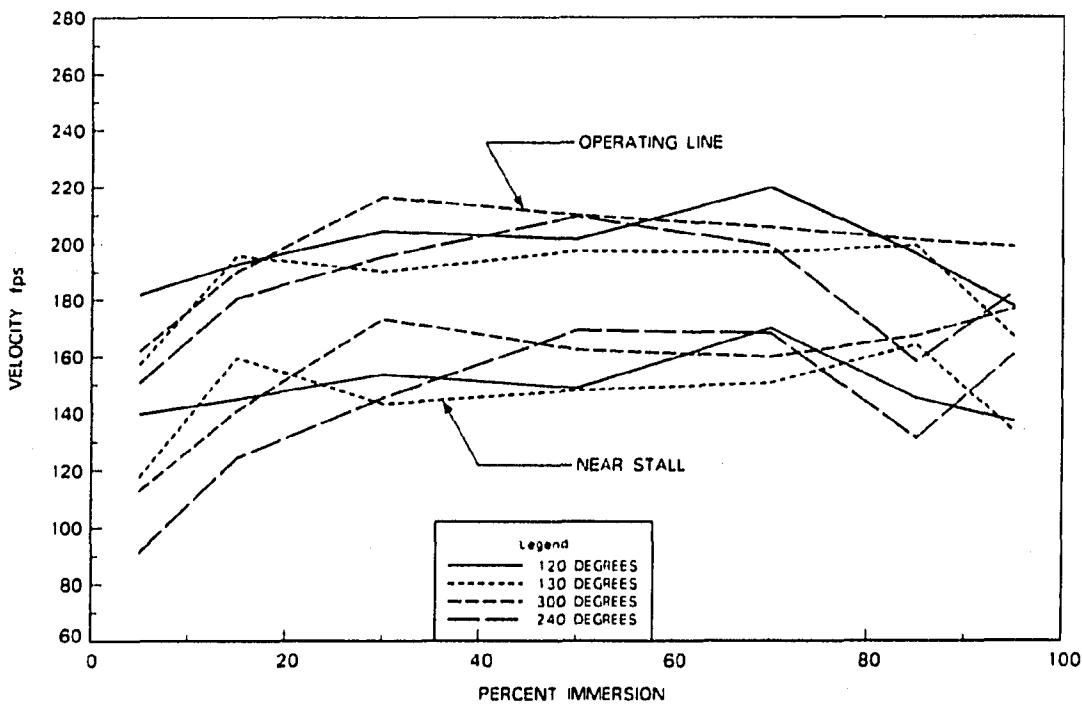


Figure 6.23: Pratt & Whitney detailed flow measurements at exit, modified, 60 percent speed

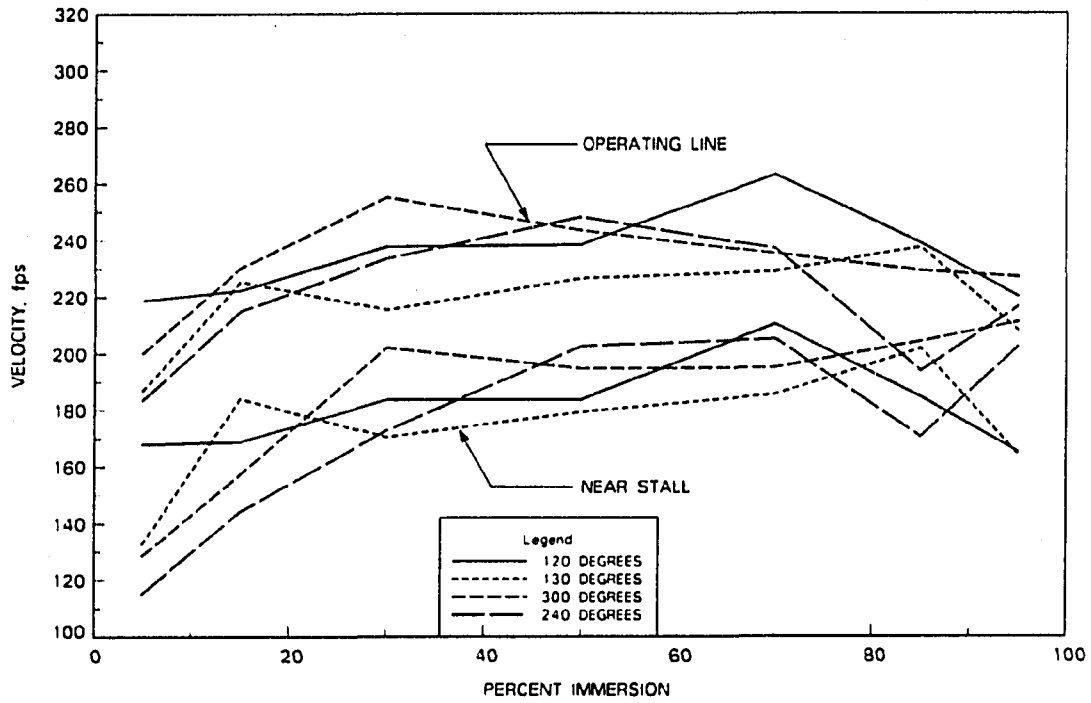


Figure 6.24: Pratt & Whitney detailed flow measurements at exit, modified, 70 percent speed

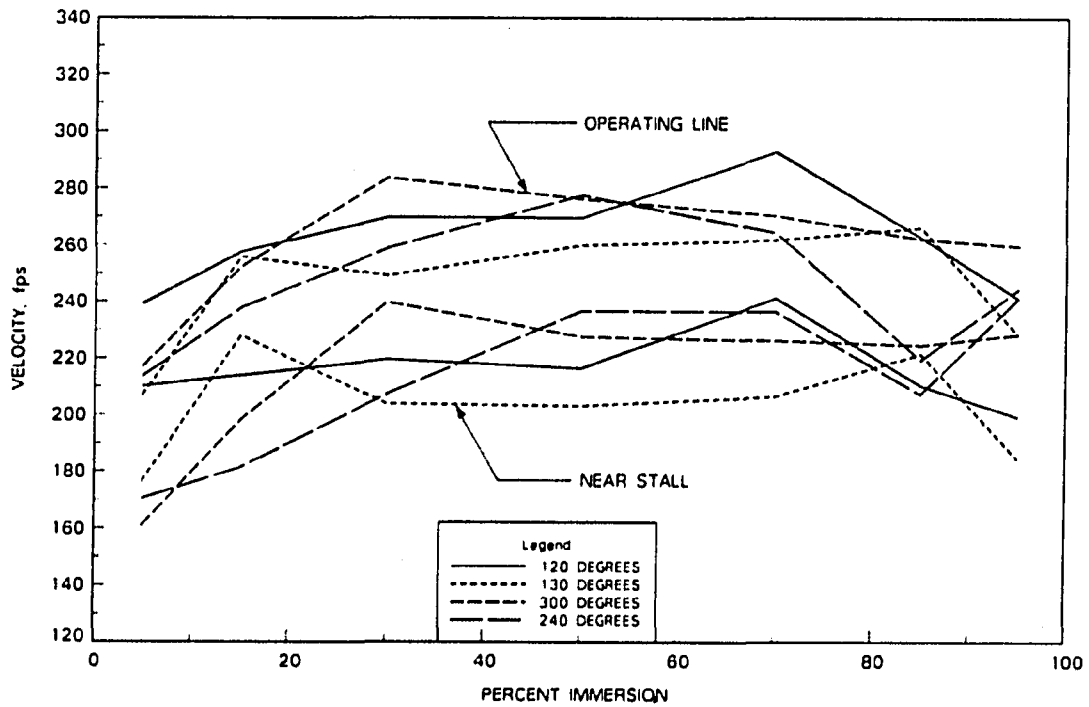


Figure 6.25: Pratt & Whitney detailed flow measurements at exit, modified, 80 percent speed

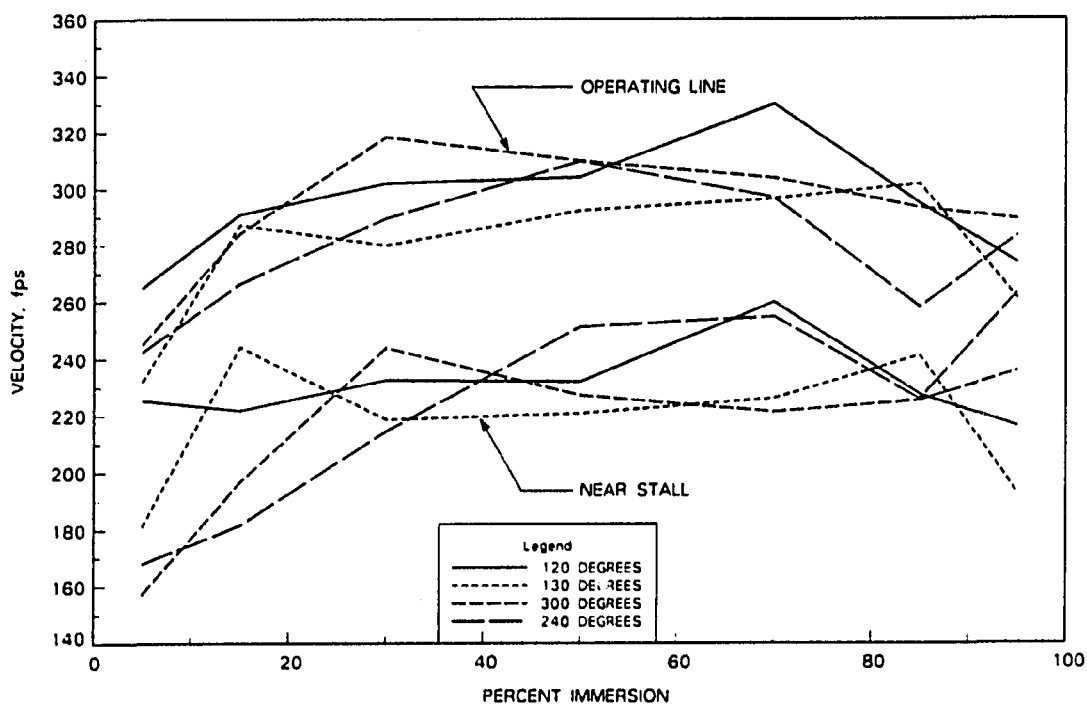


Figure 6.26: Pratt & Whitney detailed flow measurements at exit, modified, 90 percent speed

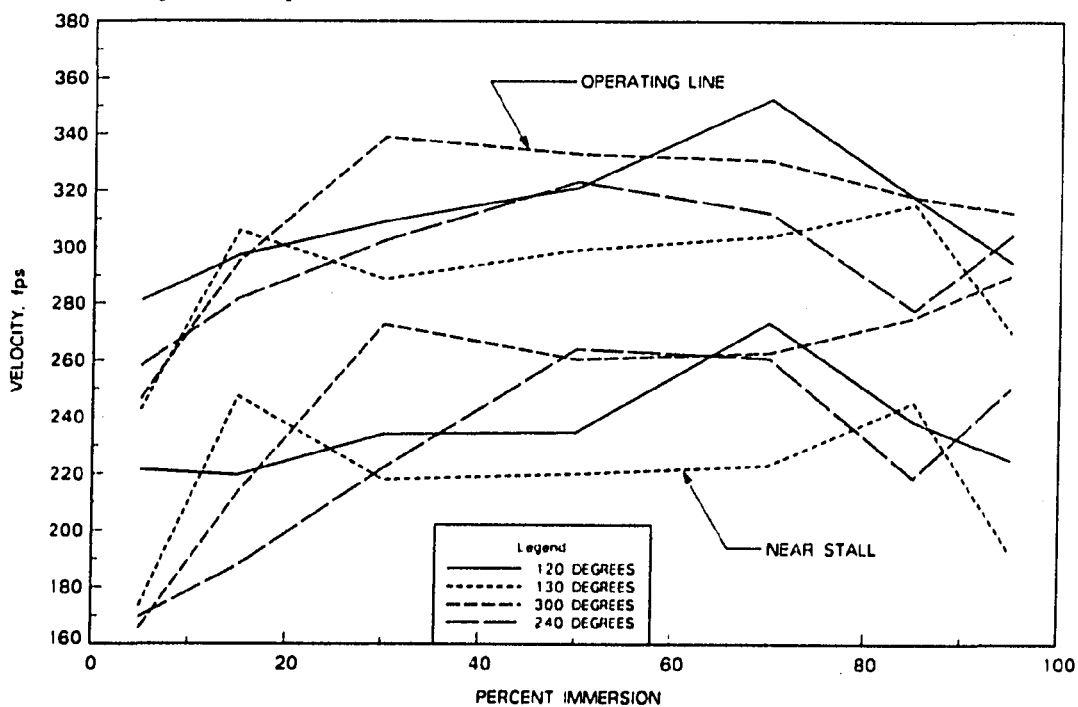


Figure 6.27: Pratt & Whitney detailed flow measurements at exit, modified, 100 percent speed

7. CONCLUSIONS

The results of the Pratt & Whitney compressor tests suggested that the stall margin, while only modestly increased at lower rotational speeds, did not improve at higher speeds. This result leads to the conclusion that although the proposed method for improving the stall margin worked modestly but consistently in a low-speed compressor, it did not significantly alter the stalling performance of the Pratt & Whitney compressor for all speeds tested. One important consolation, however, is that the aggressive approach used to increase the rotor loading (or diffusion) did not result in any significant stall margin degradation. Because only one inlet guide vane setting angle variation was evaluated for the intermediate-speed compressor in the course of this dissertation, a logical recommendation would be to evaluate additional setting angle variations. Having data for different amplitudes and frequencies of blade setting angle variations would further explore the possibility of the proposed method for improving the stall margin of compressors. Some other recommendations include acquiring detailed data for flow behind the inlet guide vanes as well as behind other stages. Some in-stall performance data may indicate some interesting observations as well.

Possible reasons why the stall margin of the higher-speed multistage compressor was not significantly improved at higher speeds may be linked to the influence of

three-dimensional flow and wake interaction effects. Also, because the aspect ratios involved presently are low, end-wall boundary layer, blade wake and tip and hub clearance effects are considerable. The dynamic stall results used to develop the present tests were largely for two-dimensional flows and were not encumbered by many complexities. It may well be that benefits associated with the present method are limited in low aspect ratio compressors by three-dimensional flow effects.

The approach of using stationary blade setting angle variations to increase the average loading of a downstream rotor and to increase the operating range of a compressor was both aggressive and risky. The object of the compressor designer, however, is to take this kind of risk hoping that it will improve compressor performance. Recently, much attention has been focused on methods for maximizing work per stage to reduce the overall weight of the compressor. To accomplish this end, methods for achieving higher loading levels in multistage compressors were investigated and reported on by Wennerstrom [16]. These methods include vortex generators, suction and blowing, and casing treatment. All of these methods are derived from successful attempts to control the boundary layer on external two-dimensional surfaces such as aircraft wings. These methods, however, have met with only limited success and the reasons for this may help explain why the presently proposed method for increasing the stall margin of a compressor was only partly successful.

First of all, it is important to point out the trends associated with reducing aspect ratio in axial-flow compressor blading as described by Wennerstrom [17]. By reducing the aspect ratio, which is defined as the ratio of blade height to chord, the three-dimensionality of the flow increases because of secondary flows and end-wall boundary-layers being more influential in the flow passage. Wennerstrom [17] defined

a low-aspect ratio to be about 2.0 and a high-aspect ratio to be greater than 4.0. The axial-flow compressors used in the present study have rotor aspect ratios which would be considered low. This would lead us to conclude that the two-dimensional dynamic stall results may indeed be diminished in the highly three-dimensional flowfields of the low aspect ratio compressors tested. Wennerstrom also suggests that low aspect ratio compressors have high tolerance levels to inlet distortions. This may indicate why there were not any significant degradations in stall margin noted for the compressors using circumferential variations in blade setting angle.

In tests performed on a high-throughflow transonic axial-flow compressor (Wennerstrom [18]), the use of casing vortex generators was evaluated in terms of compressor performance. The casing vortex generators resulted in virtually no benefit in terms of stall margin improvement despite their aggressive attempt to control the boundary-layer behavior near the tip. In contrast, tests performed with a supersonic axial compressor stage (Wennerstrom [19]) to evaluate the effects of boundary-layer control on flow induced separation, seemed to indicate otherwise. In this case, the use of casing vortex generators suggested that stall margin was improved slightly. In fact, a radial survey indicated that improvements occurred over full span and not just at the tip. This would suggest that the behavior near the end wall may determine the performance of the entire blade span.

The use of suction and blowing to control boundary layer behavior was summarized by Wennerstrom [19]. Tapered holes with specific geometry and orientation were drilled on the compressor outer casing near the rotor blade row. Results from these test suggest that suction and blowing have no effect on stall margin improvement unless stall is initiated near the outer casing, in which case there is some benefit

in terms of stall margin. In fact, when the suction or blowing was turned off, larger stall margins were noticed with distorted inlet flow. These results led to the use of casing treatments for improving the stall margins of axial-flow compressors.

All of these boundary layer control methods seem to indicate some important points. First, the end wall boundary layers seem to control the performance of the entire blade row to a certain degree. Wennerstrom [16] suggested that separation, and subsequent stall in a compressor is almost always initiated in a corner between an airfoil and endwall. Second, because only limited successes in improving the stall margins of compressor were accomplished using boundary layer control methods, it is reasonable to conclude that the proposed method can be expected to have only little beneficial effect as well.

Inasmuch as the proposed method for improving the stall margin of the compressor was only partly successful, its future may be as a component of an active control method. A number of investigators have successfully completed research programs which show significant improvements in compressor performance with the use of active control methods. In one experiment performed by Ludwig and Nenni [20], the active control of rotating stall could be accomplished on a low-speed research compressor as well as a J-85 engine. The active control was an electrical feed-back control system which used unsteady pressure signals from sensors mounted strategically throughout the machines. For the low-speed compressor tests, the variable geometry feature was the stagger angle of the stator rows. For the J-85 engine, bleed doors and flaps on the IGVs were the variable geometry feature. When the pressure sensor indicated stalling was imminent, the variable geometry feature was adjusted to avoid stall. In the case of the low-speed compressor tests, the stagger angle was

changed to reduce the rotor inlet flow angle of attack, thus avoiding stall. For the J-85 engine tests, the bleed doors and IGV flaps would open to relieve the compressor of the stalling condition. One important factor to be realized is that the control feature must adjust itself in a few milliseconds after the sensor indicates a possible stalling condition. Test results indicated that stall could be effectively eliminated in the J-85 engine. In the low-speed research tests, stall was nearly eliminated, and in the cases where stall did occur, only a few intermittent stall cells of small amplitude were observed.

Further literature on active controls includes the paper on active suppression of compressor instabilities by Epstein, Williams, and Greitzer [21]. Epstein, et al. present an analytical method of avoiding stall by using a small disturbance created by some variable geometry feature. They suggest that active flowfield control through the use of wiggly inlet guide vanes, downstream pressure perturbations, and loudspeakers can increase the operating range of a compressor by as much as 20%. In addition to these results, Epstein, et al. propose that similar active controls can be used in a compressor to quickly recover from in-stall operation. Finally, they add that the energy needed to actuate these variable geometry features would be orders of magnitude below the level of power produced by the machine.

8. BIBLIOGRAPHY

- [1] Copenhaver, W. W. "Stage Effects on Stalling and Recovery of a High-speed 10-stage Axial-flow Compressor." Ph.D. diss., Iowa State University, 1989.
- [2] "Aerodynamic Design of Axial-flow Compressors." National Aeronautics and Space Administration, NASA SP-36, 1965.
- [3] Greitzer, E. M. "Flow Instabilities in Turbomachines." Lecture Notes from ASME International Gas Turbine Institute Advanced Course on the Fluid Dynamics of Turbomachinery, July 1986.
- [4] Epstein, A. H. "Smart Engine Components: A Micro in Every Blade?" Aerospace America, January 1986.
- [5] McCroskey, W. J. "Inviscid Flowfield of an Unsteady Airfoil." AIAA Journal, Vol. 11, 1973.
- [6] Halfman, R. L., Johnson, H. C. and Haley, S. M. "Evaluation of High-Angle-of-Attack Aerodynamic-Derivative Data and Stall-Flutter Prediction Techniques." NACA TN 2533, November 1951.
- [7] McCroskey, W. J., Carr, L. W. and McAlister, K. W. "Dynamic Stall Experiments on Oscillating Airfoils." AIAA Journal, Vol. 14, 1976.
- [8] McCroskey, W. J. and Pucci, S. L. "Viscous-Inviscid Interaction on Oscillating Airfoils in Subsonic Flow." AIAA Journal, Vol. 20, 1982.
- [9] Liiva, J. "Unsteady Aerodynamic and Stall Effects on Helicopter Rotor Blade Airfoil Sections." Journal of Aircraft, Vol. 6, 1969.
- [10] General Electric Instruction Manual. "Model 5GDY34C1 Axial Flow Fan-Dynamometer Set with Speed Variator Power Unit."
- [11] Instruction Manual. "Three-stage, Low-speed, Axial-flow Compressor Operation."

- [12] Rukavina, J. P. "Stall Margin Improvement in Multistage, Axial-flow Compressors by Stationary Blade Setting Angle Modification." M.S. thesis, Iowa State University, 1989.
- [13] Thompson, K. E. "The Design and Installation of a Three-stage, Medium Speed, Axial-flow Research Compressor Test Rig." M.S. thesis, Iowa State University, 1987.
- [14] Rukavina, J. P., Okiishi, T. H. and Wennerstrom A. J. "Stall Margin Improvement in Axial-flow Compressors by Circumferential Variation of Stationary Blade Setting Angles." AIAA Paper No. 90-1912, July 1990.
- [15] Carter, A. D. S. "The Low Speed Performance of Related Aerofoils in Cascades." Aeronautical Research Council Technical Note, Report No. R. 55, September 1949.
- [16] Wennerstrom, A. J. "Highly Loaded Axial Flow Compressors: History and Current Developments." ASME Journal of Turbomachinery, Vol. 112, October 1990.
- [17] Wennerstrom, A. J. "Low Aspect Ratio Axial Flow Compressors: Why and What it Means." ASME Journal of Turbomachinery, Vol. 111, October 1989.
- [18] Wennerstrom, A. J. "Experimental Study of a High-Throughflow Transonic Axial Compressor Stage." ASME Journal of Engineering for Gas Turbines and Power, Vol. 106, July 1984.
- [19] Wennerstrom, A. J. "Some Experiments with a Supersonic Axial Compressor Stage." ASME Journal of Turbomachinery, Vol. 109, July 1987.
- [20] Ludwig, G. R. and Nenni, J. P. "A Rotating Stall Control System for Turbojet Engines." ASME Journal of Engineering for Power, Vol. 101, 1979.
- [21] Epstein, A. H., Williams, J. E., and Greitzer, E. M. "Active Suppression of Compressor Instabilities." AIAA Paper No. 86-1994, 1986.

9. ACKNOWLEDGEMENTS

I wish to express my appreciation to my colleagues of the Iowa State University Engineering Research Institute/Mechanical Engineering Department Turbomachinery Components Research Laboratory for their helpful comments and assistance. I wish to thank the staff of the Iowa State University Engineering Institute Office of Editorial Services for preparing the figures of this dissertation. Also deep thanks should go to my major professor and now department chairman, Theodore H. Okiishi, for his infinite wisdom and guidance. Thanks to my parents Dr. Daniel M. Rukavina and Patricia A. Rukavina, for spiritual support. Also to my brothers, sisters and extended family for their support, especially Mara L. Moline, my fiance, for her patience and continued support throughout this writing. Finally, I am grateful to the U. S. Air Force for their support of this project through contract F33615-87-C-2739 (Project Engineer: Dr. C. Herbert Law) and to Dr. Arthur J. Wennerstrom of the U. S. Air Force Aeropropulsion Laboratory for his helpful suggestions.

**10. APPENDIX A: DETAILED FLOW MEASUREMENTS FOR
THREE-STAGE COMPRESSOR**

Table 10.1: Absolute flow angle (°), baseline, $\Phi = 0.353$

Circumferential Position	% Imm.				
	10	30	50	70	90
1	-	-	-	-	-
2	-	-	20.6	19.1	16.0
3	22.1	22.5	20.8	19.8	16.5
4	25.4	23.7	21.8	20.1	17.4
5	26.3	24.6	22.8	20.7	18.1
6	26.7	25.1	23.7	21.6	18.7
7	27.7	25.8	25.3	22.7	19.6
8	29.5	27.1	26.0	23.8	20.5
9	-	28.5	-	27.0	-
10	-	-	-	-	-
Ave.	26.3	25.3	23.0	21.8	18.1

Table 10.2: Absolute flow angle (°), baseline, $\Phi = 0.420$

Circumferential Position	% Imm.				
	10	30	50	70	90
1	-	-	-	-	-
2	-	19.6	19.5	17.8	-
3	24.0	22.1	20.8	18.6	17.3
4	25.4	23.2	21.2	19.4	17.9
5	26.6	23.4	22.2	20.3	17.9
6	26.6	24.4	22.5	20.5	18.1
7	27.8	25.4	24.6	22.1	19.2
8	28.8	27.1	27.3	23.2	20.7
9	-	-	-	24.8	22.2
10	-	-	-	-	-
Ave.	26.5	23.6	22.6	20.8	19.0

Table 10.3: Absolute flow angle (°), $+6^\circ$ 2/rev, $\Phi = 0.353$

Circumferential Position	% Imm.				
	10	30	50	70	90
1	-	-	-	-	-
2	-	-	26.3	24.5	21.2
3	29.9	28.7	27.1	24.9	21.8
4	32.1	29.1	28.1	25.4	22.3
5	32.7	29.9	28.8	25.9	23.1
6	33.2	30.5	29.6	26.2	23.3
7	34.0	31.0	30.6	27.1	24.3
8	34.7	31.3	32.1	29.2	24.9
9	38.0	-	-	-	-
10	-	-	-	-	-
Ave.	33.5	30.1	28.9	26.2	23.0

Table 10.4: Absolute flow angle (°) variation from baseline, $+6^\circ$ 2/rev, $\Phi = 0.353$

Circumferential Position	% Imm.				
	10	30	50	70	90
1	-	-	-	-	-
2	-	-	+5.7	+5.4	+5.2
3	+7.8	+6.2	+6.3	+5.1	+5.2
4	+6.7	+5.4	+6.3	+5.3	+4.9
5	+6.4	+5.3	+6.0	+5.2	+5.0
6	+6.5	+5.4	+5.9	+4.6	+4.6
7	+6.2	+5.2	+5.3	+4.4	+4.7
8	+5.2	+4.2	+6.1	+5.4	+4.4
9	-	-	-	-	-
10	-	-	-	-	-
Ave.	+6.5	+5.3	+5.9	+5.1	+4.9

Table 10.5: Absolute flow angle (°), +6° 2/rev, $\Phi = 0.420$

Circumferential Position	% Imm.				
	10	30	50	70	90
1	-	-	-	-	-
2	-	-	-	24.5	-
3	28.8	27.5	26.3	24.9	21.6
4	31.2	29.2	27.2	25.4	22.1
5	32.0	30.0	28.1	25.6	22.6
6	32.5	30.5	28.8	26.3	23.3
7	33.3	31.2	29.2	27.6	23.9
8	34.5	31.7	30.1	28.8	24.6
9	-	32.8	30.5	30.2	-
10	-	-	-	-	-
Ave.	32.0	30.4	28.6	26.7	23.0

Table 10.6: Absolute flow angle (°) variation from baseline, +6° 2/rev, $\Phi = 0.420$

Circumferential Position	% Imm.				
	10	30	50	70	90
1	-	-	-	-	-
2	-	-	-	+6.7	-
3	+4.8	+5.4	+5.5	+6.3	+4.3
4	+5.8	+6.0	+6.0	+6.0	+4.2
5	+5.4	+6.6	+5.9	+5.3	+4.7
6	+5.9	+6.1	+6.3	+5.8	+5.2
7	+5.5	+5.8	+4.6	+5.5	+4.7
8	+5.7	+4.6	+2.8	+5.6	+3.9
9	-	-	-	+5.4	-
10	-	-	-	-	-
Ave.	+5.5	+5.8	+5.2	+5.8	+4.5

Table 10.7: Absolute flow angle (°), -6° 2/rev, $\Phi = 0.353$

Circumferential Position	% Imm.				
	10	30	50	70	90
1	-	-	-	-	-
2	-	16.3	15.0	12.8	10.5
3	19.8	17.4	16.0	13.6	10.5
4	20.2	18.0	16.2	14.2	11.6
5	20.9	18.5	16.9	14.7	12.3
6	21.4	19.2	18.1	15.4	12.8
7	22.4	20.0	19.1	16.0	14.0
8	23.8	20.9	20.3	17.5	15.0
9	-	-	-	-	15.4
10	-	-	-	-	-
Ave.	21.4	18.6	17.4	14.9	12.8

Table 10.8: Absolute flow angle (°) variation from baseline, -6° 2/rev, $\Phi = 0.353$

Circumferential Position	% Imm.				
	10	30	50	70	90
1	-	-	-	-	-
2	-	-	-5.6	-6.3	-5.5
3	-2.3	-5.1	-4.8	-6.2	-6.0
4	-5.2	-5.7	-5.6	-5.9	-5.8
5	-5.4	-6.1	-5.9	-6.0	-5.8
6	-5.3	-5.9	-5.6	-6.2	-5.9
7	-5.4	-5.8	-6.2	-6.7	-5.6
8	-5.7	-6.2	-5.7	-6.3	-5.5
9	-	-	-	-	-
10	-	-	-	-	-
Ave.	-4.9	-5.8	-5.6	-6.2	-5.7

Table 10.9: Absolute flow angle (°), -6° 2/rev, $\Phi = 0.420$

Circumferential Position	% Imm.				
	10	30	50	70	90
1	-	-	-	-	-
2	-	-	14.2	13.0	10.6
3	18.3	16.9	15.3	13.6	11.3
4	19.1	17.6	15.9	14.3	11.9
5	20.2	18.1	16.7	14.9	12.7
6	20.5	19.0	17.8	15.6	12.8
7	21.3	19.8	18.9	16.3	13.9
8	22.2	20.7	20.2	17.4	16.7
9	-	-	-	-	-
10	-	-	-	-	-
Ave.	20.3	18.7	17.0	15.0	12.8

Table 10.10: Absolute flow angle (°) variation from baseline, -6° 2/rev, $\Phi = 0.420$

Circumferential Position	% Imm.				
	10	30	50	70	90
1	-	-	-	-	-
2	-	-	-5.3	-4.8	-
3	-5.7	-5.2	-5.5	-5.0	-6.0
4	-6.3	-5.6	-5.3	-5.1	-6.0
5	-6.4	-5.3	-5.5	-5.4	-5.2
6	-6.1	-5.4	-4.7	-4.9	-5.3
7	-6.5	-5.6	-5.7	-5.8	-5.3
8	-6.6	-6.4	-7.1	-5.8	-4.0
9	-	-	-	-	-
10	-	-	-	-	-
Ave.	-6.3	-5.6	-5.6	-5.3	-5.3

Table 10.11: Absolute flow angle (°), -16° 2/rev, $\Phi = 0.420$

Circumferential Position	% Imm.				
	10	30	50	70	90
1	-	-	-	-	-
2	-	-	-	-	-0.6
3	6.1	4.3	2.7	2.1	0.9
4	7.4	5.6	3.7	3.5	1.8
5	8.1	6.7	4.9	4.2	3.2
6	9.1	7.4	5.9	5.1	3.6
7	9.4	8.9	7.1	6.0	5.2
8	11.4	11.4	8.7	8.8	6.6
9	13.7	-	-	-	-
10	-	-	-	-	-
Ave.	9.3	7.4	5.5	5.0	3.0

Table 10.12: Absolute flow angle (°) variation from baseline, -16° 2/rev, $\Phi = 0.420$

Circumferential Position	% Imm.				
	10	30	50	70	90
1	-	-	-	-	-
2	-	-	-	-	-
3	-16.0	-19.4	-18.1	-17.7	-15.4
4	-18.0	-19.0	-18.1	-16.6	-16.1
5	-18.2	-18.4	-17.9	-16.5	-14.7
6	-17.6	-18.4	-17.8	-16.5	-14.5
7	-18.4	-18.2	-18.2	-16.7	-14.0
8	-18.1	-17.1	-17.3	-15.0	-14.1
9	-	-	-	-	-
10	-	-	-	-	-
Ave.	-17.7	-18.4	-17.9	-16.5	-14.8

Table 10.13: Absolute flow angle (°), -16° 2/rev, $\Phi = 0.353$

Circumferential Position	% Imm.				
	10	30	50	70	90
1	-	-	-	-	-
2	-	1.2	-	-1.9	-1.1
3	5.7	4.0	3.0	1.1	1.1
4	7.6	5.5	4.0	3.1	2.5
5	7.8	6.6	5.2	4.7	4.0
6	8.8	7.7	6.9	5.6	5.0
7	9.8	8.5	8.0	6.9	7.0
8	12.0	10.0	10.1	8.1	9.1
9	-	-	-	-	-
10	-	-	-	-	-
Ave.	8.6	6.2	6.2	3.9	3.9

Table 10.14: Absolute flow angle (°) variation from baseline, -16° 2/rev, $\Phi = 0.353$

Circumferential Position	% Imm.				
	10	30	50	70	90
1	-	-	-	-	-
2	-	-	-	-21.0	-17.1
3	-16.4	-18.5	-17.8	-18.7	-15.4
4	-17.8	-18.2	-17.8	-17.0	-14.9
5	-18.5	-18.0	-17.6	-16.0	-14.1
6	-17.9	-17.4	-16.8	-16.0	-13.7
7	-18.0	-17.3	-17.3	-15.8	-12.6
8	-17.5	-17.1	-15.9	-15.7	-11.4
9	-	-	-	-	-
10	-	-	-	-	-
Ave.	-17.7	-17.8	-17.2	-17.2	-14.2

**11. APPENDIX B: VELOCITY DIAGRAM CALCULATIONS FROM
DETAILED MEASUREMENT DATA**

Table 11.1: Detailed flow measurement data, baseline, $\Phi = 0.353$

% Imm.	P_{st} lb/in^2	β_1 ($^\circ$)	V_1 ft/s	V_{θ_1} ft/s	U_1 ft/s	w_{θ_1} ft/s	V_{x_1} ft/s	w_1 ft/s	β'_1 ($^\circ$)	K_{RF}
10	-0.0103	18.1	36.60	11.37	94.81	83.44	34.79	90.40	67.4	0.23
30	-0.0105	21.8	36.92	13.71	88.94	75.23	34.28	82.67	65.5	0.25
50	-0.0107	23.0	37.30	14.57	83.08	68.51	34.33	76.63	63.4	0.27
70	-0.0110	25.3	37.74	16.13	77.21	61.08	34.12	69.96	60.8	0.30
90	-0.0113	26.3	38.35	16.99	71.35	54.36	34.38	64.32	57.7	0.32

Table 11.2: Detailed flow measurement data, baseline, $\Phi = 0.420$

% Imm.	P_{st} lb/in^2	β_1 ($^\circ$)	V_1 ft/s	V_{θ_1} ft/s	U_1 ft/s	w_{θ_1} ft/s	V_{x_1} ft/s	w_1 ft/s	β'_1 ($^\circ$)
10	-0.0156	19.0	45.04	14.66	94.81	80.15	42.59	90.76	62.0
30	-0.0158	20.8	45.35	16.10	88.94	72.84	42.39	84.28	59.8
50	-0.0161	22.6	45.76	17.58	83.08	65.50	42.25	77.94	57.2
70	-0.0165	23.6	46.32	18.54	77.21	58.67	42.45	72.42	54.1
90	-0.0170	26.5	46.97	20.96	71.35	50.39	42.04	65.62	50.2

Table 11.3: Detailed flow measurement data, $+6^\circ$ 2/rev, $\Phi = 0.353$

% Imm.	β_1 ($^\circ$)	V_1 (ft/s)	V_{θ_1} (ft/s)	U_1 (ft/s)	w_{θ_1} (ft/s)	V_{x_1} (ft/s)	w_1 (ft/s)	β'_1 ($^\circ$)	$\Delta\beta'_1$ ($^\circ$)
10	23.0	37.79	14.77	94.81	80.04	34.79	87.27	66.5	-0.9
30	26.2	38.21	16.87	88.94	72.07	34.28	79.81	64.6	-0.9
50	28.9	39.21	18.95	83.08	64.13	34.33	72.74	61.8	-1.6
70	30.1	39.44	19.78	77.21	57.43	34.12	66.80	59.3	-1.5
90	33.5	41.23	22.76	71.35	48.59	34.38	59.52	54.7	-3.0

Table 11.4: Detailed flow measurement data, $+6^\circ$ 2/rev, $\Phi = 0.420$

% Imm.	β_1 ($^\circ$)	V_1 (ft/s)	V_{θ_1} (ft/s)	U_1 (ft/s)	w_{θ_1} (ft/s)	V_{x_1} (ft/s)	w_1 (ft/s)	β'_1 ($^\circ$)	$\Delta\beta'_1$ ($^\circ$)
10	23.0	46.27	18.08	94.81	76.73	42.59	87.76	61.0	-1.0
30	26.7	47.45	21.32	88.94	67.62	42.39	79.81	57.9	-1.9
50	28.6	48.12	23.03	83.08	60.05	42.25	73.42	54.9	-2.3
70	30.4	49.22	24.91	77.21	52.30	42.45	67.36	50.9	-3.2
90	32.0	49.57	26.27	71.35	45.08	42.04	61.64	47.0	-3.2

Table 11.5: Detailed flow measurement data, -6° 2/rev, $\Phi = 0.353$

% Imm.	β_1 ($^\circ$)	V_1 (ft/s)	V_{θ_1} (ft/s)	U_1 (ft/s)	w_{θ_1} (ft/s)	V_{x_1} (ft/s)	w_1 (ft/s)	β'_1 ($^\circ$)	$\Delta\beta'_1$ ($^\circ$)
10	12.8	35.68	7.90	94.81	86.91	34.79	93.61	68.2	+0.8
30	14.9	35.47	9.12	88.94	79.82	34.28	86.87	66.8	+1.3
50	17.4	35.98	10.76	83.08	72.32	34.33	80.05	64.6	+1.2
70	18.6	36.00	11.48	77.21	65.73	34.12	74.06	62.6	+1.8
90	21.4	36.92	13.47	71.35	57.88	34.38	67.32	59.3	+1.6

Table 11.6: Detailed flow measurement data, -6° 2/rev, $\Phi = 0.420$

% Imm.	β_1 ($^\circ$)	V_1 (ft/s)	V_{θ_1} (ft/s)	U_1 (ft/s)	w_{θ_1} (ft/s)	V_{x_1} (ft/s)	w_1 (ft/s)	β'_1 ($^\circ$)	$\Delta\beta'_1$ ($^\circ$)
10	12.8	43.67	9.68	94.81	85.13	42.59	95.19	63.4	+1.4
30	15.0	43.88	11.36	88.94	77.58	42.39	88.40	61.3	+1.5
50	17.0	44.18	12.92	83.08	70.16	42.25	81.90	58.9	+1.7
70	18.1	44.66	13.87	77.21	63.34	42.45	76.25	56.2	+2.1
90	20.3	44.82	15.55	71.35	55.80	42.04	69.86	53.0	+2.8

Table 11.7: Detailed flow measurement data, -16° 2/rev, $\Phi = 0.353$

% Imm.	β_1 ($^\circ$)	V_1 (ft/s)	V_{θ_1} (ft/s)	U_1 (ft/s)	w_{θ_1} (ft/s)	V_{x_1} (ft/s)	w_1 (ft/s)	β'_1 ($^\circ$)	$\Delta\beta'_1$ ($^\circ$)
10	3.9	34.87	2.37	94.81	92.44	34.79	98.77	69.4	+2.0
30	3.9	34.36	2.34	88.94	86.60	34.28	93.14	68.4	+2.9
50	6.2	34.53	3.73	83.08	79.35	34.33	86.46	66.6	+3.2
70	6.2	34.32	3.71	77.21	73.50	34.12	81.03	65.1	+4.3
90	8.9	34.80	5.38	71.35	65.97	34.38	74.39	62.5	+4.8

Table 11.8: Detailed flow measurement data, -16° 2/rev, $\Phi = 0.420$

% Imm.	β_1 ($^\circ$)	V_1 (ft/s)	V_{θ_1} (ft/s)	U_1 (ft/s)	w_{θ_1} (ft/s)	V_{x_1} (ft/s)	w_1 (ft/s)	β'_1 ($^\circ$)	$\Delta\beta'_1$ ($^\circ$)
10	3.0	42.65	2.23	94.81	92.58	42.59	101.91	65.3	+3.3
30	5.0	42.55	3.71	88.94	85.23	42.39	95.19	63.6	+3.8
50	5.5	42.44	4.07	83.08	79.01	42.25	89.60	61.9	+4.7
70	7.4	42.81	5.51	77.21	71.70	42.45	83.32	59.4	+5.3
90	9.3	42.60	6.88	71.35	64.47	42.04	76.97	56.9	+6.7